BIOMECHANCIAL CHARACTERIZATION OF POSTNATAL GROWTH BEHAVIOR IN THE OVINE MAIN PULMONARY ARTERY

by

Bahar Fata

B.S. in Bioengineering, University of California at Berkeley, 2003

M.S. in Biomedical Engineering, University of Southern California, 2007

Submitted to the Graduate Faculty of

The Swanson School of Engineering in partial fulfillment

of the requirements for the degree of

Doctor of Philosophy

University of Pittsburgh

2012

UNIVERSITY OF PITTSBURGH

SWANSON SCHOOL OF ENGINEERING

This dissertation was presented

by

Bahar Fata

It was defended on

June 12, 2012

and approved by

Larry A. Taber, PhD, Professor, Department of Biomedical Engineering, Washington University in St. Louis

Sanjeev G. Shroff, PhD, Professor, Department of Bioengineering

David A. Vorp, PhD, Professor, Department of Bioengineering

John C. Brigham, PhD, Assistant Professor, Department of Civil and Environmental Engineering

Dissertation Director: Michael S. Sacks, PhD, W. A. "Tex" Moncrief, Jr. Simulation-Based Engineering Science Chair, Department of Biomedical Engineering, University of Texas at Austin

BIOMECHANCIAL CHARACTERIZATION OF POSTNATAL GROWTH BEHAVIOR IN THE OVINE MAIN PULMONARY ARTERY

Bahar Fata, PhD

University of Pittsburgh, 2012

It has been estimated that worldwide 600,000 babies are born annually with significant congenital heart disease. In children with congenital heart disease, normal growth and hemodynamic function of the pulmonary arteries and aorta become disrupted due to structural heart defects and/or genetic disorders. Congenital heart and related vascular defects cause increased flow and pulmonary pressure leading to unfavorable vascular remodeling that result in pulmonary arterial hypertension. Congenital abnormalities of these arteries often necessitate surgical repair or the use of autologous tissue and synthetic biomaterials as vascular grafts. The optimal vascular replacement should be able to accommodate somatic growth and closely mimic the structure, function and physiologic environment of native vessels. In recent years, there has been a growing interest in the development of a living autologous tissue graft that could address the critical need for growing substitutes in the repair of congenital cardiovascular defects.

In the current study, the biomechanical characteristics of the native ovine main pulmonary artery during postnatal growth period were delineated to establish the benchmarks for tissue engineering approaches. The local postnatal alterations in the surface geometry of the pulmonary artery based on magnetic resonance images of the endoluminal arterial surface were estimated. The regional growth adaptations of the mechanical behavior and elastin structure were subsequently quantified. The collagen organization and recruitment behavior using a biaxial stretching device combined with multiphoton microscopy were measured. The experimental

measurements were finally fit to a structurally-based constitutive model of the arterial wall. The results of this study can also help elucidate the governing mechanisms of normal remodeling and growth process by enhancing our knowledge of alterations in the geometry and structure-mechanics relationship of the pulmonary arterial wall during postnatal maturation.

TABLE OF CONTENTS

LIST OF TABLES

LIST OF FIGURES

NOMENCLATURE

Acronyms

Acronym	Description
PT	Pulmonary trunk
PA	Main pulmonary artery
AA	Ascending aorta
STJ	Sinotubular junction
BFN	Main pulmonary artery bifurcation to left and right pulmonary arteries
End-ROI	End of region of interest on AA
MRI	Magnetic resonance imaging
ECM	Extracellular matrix
RMS	Root mean square
PBS	Phosphate buffered solution
SALS	Small angle light scattering
MPM	Multiphoton microscopy
SHG	Second harmonic generation
TPEF	Two-photon excitation autofluorescence
NOI	Normalized orientation index
RVE	Representative volume element

Symbols

Symbol	Description
Ψ	Strain energy density function
S, $\mathbf{S}$	Second Piola Kirchhoff Stress (tensor)
P, $\mathbf{P}$	First Piola Kirchhoff Stress or Lagrangian stress (tensor)
σ, $\boldsymbol{\sigma}$	Cauchy stress (tensor)
E, $\mathbf{E}$	Green strain (tensor)
F, $\mathbf{F}$	Deformation gradient (tensor)
λ	stretch
R	2D Fiber orientation distribution function
D	Collagen cumulative recruitment distribution function
d	Collagen recruitment probability density function
Ψ^{ens}	Fiber ensemble strain energy density function
S^{ens}	Fiber ensemble 2nd Piola Kirchhoff stress
ψ^{f}	Single fiber strain energy density function
λ^{ens}	Fiber ensemble stretch
$\mathbf{N}$	Vector aligned with fiber direction in reference configuration Ω_0
$\mathbf{n}$	Vector aligned with fiber direction in deformed configuration Ω_t
θ	Fiber orientation angle with respect to tissue reference coordinate X_1
λ^{ub}	Upper bound ensemble stretch
ϕ_i	Mean volume fraction of tissue component i (i = elastin, collagen or ground matrix)
η_{el}	Elastin ensemble effective modulus
b	Elastin ensemble dimensionless parameter
η_{col}	Collagen fibers effective modulus
η_{gm}	Ground matrix effective shear modulus (neoHookean constant)

PREFACE

My PhD journey started at the University of Southern California (USC) in the Heart Valve Biomechanics Laboratory of Dr. Ivan Vesely. There I was offered many opportunities that helped me build the foundation to do independent research and to develop a profound appreciation of the team-oriented approach to problem solving. I was fortunate to enjoy the wonderful mentorship of Dr. Daniel Einstein whose extensive knowledge of computational mechanics gave me a head-start in my research project. I hope to become as great of a researcher and mentor as him someday. Upon the departure of Dr. Vesley from USC to manage his own firm, I had to find another position to pursue my PhD aspirations. I was graciously offered a position by Dr. Michael Sacks in the Cardiovascular Biomechanics Laboratory at the University of Pittsburgh (Pitt).

At Pitt I worked alongside wonderful graduate students and postdocs, was challenged in many ways and formed great memories that will stay with me forever. There are many people whose help and companionship during these past years has eased the challenges and difficulties of the PhD experience/journey. I cannot mention all their names here, but I am deeply grateful to all of them. I would like to thank Dr. Sacks for providing me with the opportunity to continue working in the field of soft tissue biomechanics and to conduct research in a supportive laboratory environment. His attitude towards research and mentorship has helped my personal

and professional growth along with strengthening my convictions on the importance of humility, and respecting others and their unique abilities.

I am thankful to all of the administrative staff especially Dan Gealey, Jason Vey, Nick Mance, Glenn Peterson, Lynette Spataro and Karen Connor. I am grateful to Karen for doing the utmost possible during these past few years to help ease the lives of everyone in the lab. I wish to thank all of the graduate students and postdocs in the lab especially Erinn Joyce, Chad Eckert, Chris Caruthers, John Stella, Antonio D'Amore and Daniela Valdez-Jasso for their support and team-oriented outlook. I would like to acknowledge Erinn, Chad, and Chris for kindly reading and providing feedback on different chapters of my dissertation. I am thankful to Diana Gaitan and Silvia Wognum for their companionship and friendship especially during the start of my time at Pitt. Although I was very sad to see Diana depart back to Colombia, I am so happy that she is pursuing her passion of teaching and serving her country. She will be my dear friend forever.

I was so fortunate be part of a great bioengineering department at Pitt with many outstanding faculty members. I am much obliged to Dr. Harvey Borovetz for agreeing to and generously assisting my continued PhD work at Pitt after Dr. Sacks' departure to the University of Texas last year. I am deeply grateful to Dr. Sanjeev Shroff for his kind support and sage guidance particularly during this past year.

Although working on a PhD is to a great extent an individual effort, the exchange of ideas and receiving input from different perspectives is crucial to any successful research endeavor. I was blessed to have had Dr. Rouzbeh Amini by my side during these past two years. His open willingness to honestly discuss and challenge ideas, his conviction in providing mentorship, and his solid knowledge of mechanics has greatly aided my dissertation work.

I am grateful to the Pittsburgh Baha'i community for being my second family during this past five years, especially Astrid Kersten, Sharon Eakes, Ayorkor Korsah, Jeri Corbin, Monir and Mahmood Safaean, Linsey McDaniel, Laura Stokes, Ginny Grych, Lahia and Jason Rafalak, who have all helped me to become a better person. I would like to thank my sister Azadeh for being a great friend and support. I would not be where I am today without the unconditional love and sacrifice of my parents, Reza and Soodabeh. Throughout my upbringing they encouraged free and independent thinking and instilled in me the passion for science and engineering. I am immensely blessed to have been raised by such nurturing and open-minded parents. Finally, I am deeply appreciative of my dear husband and best friend, Saba Notghi. He patiently stood by me and forsook his comfort and desires since we met four years ago, so that I could pursue my goal of completing a PhD. I would not have been able to finish my dissertation work without his love and support. I love him with all my heart.

1.0 INTRODUCTION

Growth and remodeling is a cellular activity that is controlled by growth hormones and growth factors at the molecular level. From a physiological perspective, growth is a change in the homeostatic state due to alterations in the environment and internal stresses [1]. Through the application of mechanics, the field of biomechanics enables a better understanding of the effects of mechanical loads on the structure, properties, and function of living tissues [2]. There is great interest in the pulmonary circulation among pediatricians due to the relatively high incidence and extent of pulmonary vascular change in congenital heart disease [3-5], and also among cardiologists due to the occurrence of pulmonary hypertension in chronic rheumatic and thromboembolic disease [6-10].

In the current work, biomechanical principles, based on the application of continuum mechanics to physiology, are employed to delineate the change in the structure-function relationship of the pulmonary arterial tissue as it undergoes normal growth process. The general approach outlined by Y.C. Fung [11] will be followed to conduct a biomechanical study of selected 'quasistatic' snapshots of postnatal growth in the pulmonary artery according to the following steps:

1. Study the gross anatomy of the organ.
2. Delineate the histology and microstructure of the tissue
3. Determine the mechanical properties of the tissue.

4. Derive a constitutive equation based on the fundamental laws of physics (e.g. conservation of mass, conservation of momentum, conservation of energy).
5. Compare the experimental results with theoretical ones to determine whether the given hypotheses are justified.

1.1 MAIN PULMONARY ARTERY ANATOMY AND FUNCTION

The pulmonary trunk (PT) lies between the pulmonary valve and the bifurcation (BFN) into the right and left pulmonary arteries. It carries oxygen-deficient blood from the right ventricle toward the lungs. In this study the main pulmonary artery (PA) is defined as the region of the PT bounded proximally by the pulmonary valve sinotubular junction (STJ) and distally by the BFN (Figure 1.1). The PA is elliptical in cross-section rather than circular, and tapers towards its BFN point [10]. It is curved towards its posterior and medial aspects with a more prominent curvature towards the former aspect. On its medial wall, the PA is adjacent to the ascending aorta (AA), and the auricle of the left atrium lies on its lateral aspect proximal to the BFN. The anterior wall of the pulmonary trunk is physically connected to the AA through connective tissue on its medial aspect and on its anterior wall through the ligamentum arteriosum, the origin of which will be explained in the following section (section 1.2).

Under normal conditions, the output of the right ventricle is equal to that of the left ventricle. The hemodynamics of the pulmonary and systemic circulations are, however, quite different. Their major differences are as follows: 1) The mean pulmonary arterial pressure is about one-sixth of the systemic; 2) The pulmonary vascular resistance is also about one-sixth of

the systemic; 3) Pulmonary arteries are more distensible; 4) Pulmonary arteries do not become stiffer from central towards peripheral sites, as do the systemic arteries [10].

The pumping action of the right ventricle causes pressure in the PT to exceed that of the pulmonary veins to the extent that it forces blood through the pulmonary vascular resistance at a rate of 5 L/min [10]. The large compliance of the pulmonary trunk enables it to convert the pulsatile pumping action of the right ventricle to a relatively continuous blood flow through the pulmonary system. As the right ventricle pumps blood during systole the pulmonary trunk expands, and as the right ventricle starts relaxing during diastole, the PA pressure exceeds the RV pressure causing the pulmonary valve to close; then the pulmonary trunk passively unloads and forces blood flow through the pulmonary arteries and vasculature.

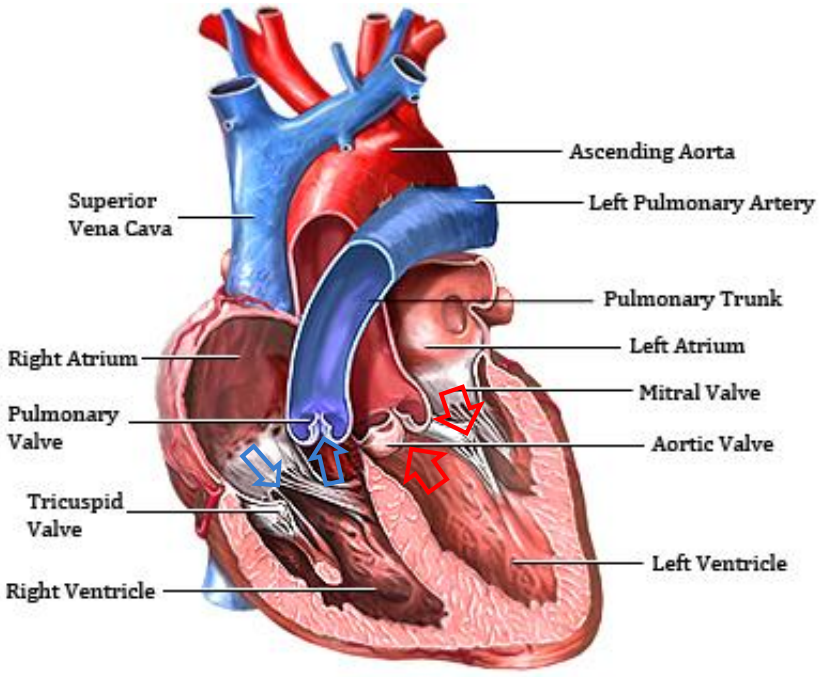

Figure 1.1. Artistic depiction of human heart showing pulmonary trunk and surrounding structures (anterior view). Pulmonary trunk is bounded proximally by pulmonary valve and distally by left and right pulmonary arteries and located adjacent to ascending aorta and left atrium on its medial and lateral walls, respectively (direction of blood flow shown with arrows) (U.S. National Library of Medicine: http://www.ncbi.nlm.nih.gov).

1.2 PHYSIOLOGICAL DEVELOPMENT OF THE PULMONARY ARTERY AND AORTA

During normal embryogenesis, the truncus arteriosus begins to split and form into the anterior pulmonary artery and the posterior aorta [12]. During the prenatal period, a state of physiologic pulmonary hypertension exists due to the patent ductus arteriosus and the equalization of aortic and pulmonary artery pressures; the AA and PA are similar in wall thickness. At the time of birth, the lungs begin to function, the ductus arteriosus closes (gradually becoming a ligament structure), and the PA experiences a significant drop in blood pressure and hemodynamic change. Therefore, changes in the pulmonary vascular resistance, pulmonary blood flow, and oxygen tension distinguish the pulmonary from the systemic circulation, and trigger a transition from the fetal to the postnatal circulatory pattern [13, 14]. The attenuation of medial smooth muscle of the PA wall results in decrease of the ratio of medial thickness to external diameter from 20% to 25% in fetuses to less than 10% in infants 3 to 6 months of age. Beyond the first year of life, thickness of the PA wall is normally less than half that of the adjacent ascending aorta, although diameters of the two great arteries remain similar [15].

1.3 MOTIVATION BEHIND THE STUDY

1.3.1 Diseases Affecting Pulmonary Artery and Treatment Options

It has been estimated that worldwide 600,000 babies are born annually with significant congenital heart disease [16]. In children with congenital heart disease, normal growth and hemodynamic

function of the pulmonary arteries and aorta become disrupted either due to structural heart defects and/or genetic disorders [16-20]. This includes Alagille and Williams syndromes and acquired defects after surgical interventions, most commonly subsequent to the repair of tetralogy of Fallot. Congenital heart and related vascular defects cause increased flow and pulmonary pressure leading to unfavorable vascular remodeling that results in pulmonary arterial hypertension [16, 17, 21]. In children, pulmonary arterial hypertension is a severe condition that leads to substantial remodeling of the extracellular matrix (ECM) in the proximal pulmonary arteries. In systemic arteries, hypertension and aging can lead to structural remodeling in the form of increase in the media thickness, rise in the collagen/elastin ratio, and changes in the structure of the elastic lamina [22, 23].

There are a number of disease conditions that originate in the AA and eventually affect the PA. For example, PA dilation can occur in association with genetic diseases of connective tissue such as Marfan syndrome and with pulmonary valve hemodynamic abnormalities; however, in the absence of any abnormal pulmonary conditions, PA dilation can also occur due to bicuspid aortic valve disease, which is the most common aortic valve malformation [19].

Congenital abnormalities of these arteries often necessitate surgical repair or the use of autologous tissue and synthetic biomaterials as vascular grafts [24-26]. The patency of the synthetic conduit replacements is limited, often requiring further surgical re-interventions due to lack of adaptation to the normal growth of the child and/or functional failure of the graft [27]. The autologous conduit replacements are limited in supply and may not adjust to the different flow environment of the graft site. The optimal vascular replacement should be able to accommodate somatic growth and closely mimic the structure, function and physiologic environment of native vessels. In recent years, there has been a growing interest in the

development of a living autologous tissue graft that could address the critical need for growing substitutes in the repair of congenital cardiovascular defects [28-31].

Detailed growth characteristics of the native artery are required to establish the baseline for tissue-engineered construct in post-implantation. Moreover, delineating the normal arterial growth characteristics has implications for the timing and nature of surgical repair [12, 24]. Finally, understanding the normal arterial morphogenesis is a prerequisite to understanding any disease process by yielding unique insight into the mechanisms of vascular adaptations and their important physiological factors.

1.3.2 Study of Three-Dimensional Geometry and Surface Growth 'Deformation'

There have been promising results in the engineering of arterial conduit replacements [28-30]. However, there is an absence of the required benchmarks of three-dimensional (3D) geometry of these engineered conduit replacements, particularly shape changes associated with somatic growth. Since arterial geometry greatly influences hemodynamics [32], replacement conduits should closely resemble the native 3D arterial shape and, critically, accommodate somatic growth. Therefore, a detailed knowledge of the native arterial shape during normal postnatal growth is a prerequisite in the development of conduit tissue engineering endeavors.

Children with congenital heart disease undergo diagnostic imaging for the evaluation of right ventricular outflow tract dimensions, and the normal sizes of portions of the PT have been carefully elucidated in various stages of development [33-40]. However, the normal progression of three-dimensional PT geometry during postnatal growth, including whether growth is a proportionate scale-up of size in which basic geometric proportions are maintained (i.e. an

isotropic growth pattern), or whether the shape of the PT changes over the period of postnatal growth (anisotropic growth), remains unknown.

Furthermore, an understanding of the dynamic processes of developmental growth in arteries requires a detailed description of the temporal and spatial patterns of geometrical changes. Previous studies have been limited in that they do not provide a detailed, spatially continuous description of the local temporal and spatial patterns associated with growth. Moreover, use of a geometric descriptor that allows for the computation of continuous growth trends with increasing mass can elucidate general growth patterns and reduce errors associated with the use of individual specimen reconstructions.

Recent advances in cardiac magnetic resonance imaging (MRI) and image segmentation offer the potential for detailed three-dimensional characterization of cardiac structures *in vivo*. Many prior investigations have utilized ovine animal models in the evaluation of cardiovascular physiology and heart valve testing [41, 42]. In the present study we will provide a thorough description of the 3D surface geometry of native ovine PA by estimating the mapping of older PA surface shape to the youngest one, and delineating regional modifications in surface geometry using nonlinear deformation analysis. Therefore, growth deformation patterns using MRI data are obtained in order to define the critical three-dimensional benchmarks for PT conduit replacements over time.

Despite their close mechanical association throughout lifetime, the effects of the AA and PA physical coupling on their respective geometries during the normal postnatal remodeling period remains unknown. The present work is thus undertaken to determine the regional postnatal surface growth deformation of the PA and AA to shed light on the underlying causes leading to

the specific three-dimensional surface shape alterations in these arteries during postnatal development and gain further insight into the uniqueness of specific geometric changes of the PA.

1.3.3 Study of Arterial Wall Mechanics and Structure

The relationship of pressure to flow and the propagation of both in the artery is a function of arterial mechanics. Changes in the distensibility of large blood vessels are critical determinants of ventricular afterload and eventual dysfunction in the pulmonary hypertension as well as many congenital defects [43]. The mechanical behavior of the proximal pulmonary arteries is modified in pulmonary hypertension and in many congenital defects due to substantial ECM remodeling and wall thickening [44, 45]. Diminishing compliance of the large pulmonary arteries has been linked to the deposition of excess matrix proteins in the arterial wall [46]. Biochemical studies in animals have shown a significant upsurge in the collagen and elastin synthesis and content in hypertensive pulmonary arteries [46-48].

It is well known that newborn animals develop more severe pulmonary hypertension than adults with dramatic vascular changes [49]. The perinatal period is associated with significant elastin and collagen accumulation in the pulmonary trunk and aorta in preparation for a marked postnatal increase in arterial pressure [50, 51]. Therefore, the elastin and collagen synthesis may be particularly sensitive to modulation by hypoxia during this time of rapid growth. Lammers et al. [52] have delineated the prominent role of elastin in the alteration of pulmonary artery mechanics in hypertensive calves. However, they point out that in order to fully realize the nature of this disease phenomenon, the elastin structure of both the normal PA and that of the hypertensive arterial wall has to be studied and quantified.

In a few previous studies, it has been shown that the regional mechanical behavior of the aorta is modified as a result of normal growth and aging [53-58]. It has been claimed, for example, that the elastic modulus changes as a result of alteration in vessel geometry and ECM mass [56]. It has been suggested that the structure of the artery adapts to changes in arterial shape during postnatal growth in order to maintain an equilibrium mechanical tension per elastin lamellar unit [50, 59]. Wells et al. [60, 61] revealed an important relationship between the mechanics and ECM composition of the ovine thoracic aorta wall during the postnatal maturation. The incremental elastic modulus at low tensile stress was linked to the relative elastin content during the perinatal period; however, they demonstrated that neither variable changed during postnatal life. They measured a substantial increase in the incremental elastic modulus at high tensile stress during postnatal life that corresponded to a dramatic increase in the collagen cross-linking index in the absence of a significant change in relative collagen content.

There have not been any studies on the regional alteration in the mechanical behavior of normal growing vessels and under pulmonary hypertension, particularly the trunk and right main artery. In the current study, the micromorphological and mechanical adaptations of the native ovine PA based on the quantified geometrical surface growth profile are characterized to initially resolve the relationship between geometrical and biomechanical heterogeneity during postnatal growth. Secondly, the study was undertaken to delineate the relationship between mechanical behavior and microstructure, and to understand the role of elastin and collagen in normal pulmonary artery remodeling during postnatal growth. Finally, the structural and mechanical data was used in developing an appropriate constitutive model to explain the structure-function relationship and for future applications in predicting the alterations in the mechanical behavior of the artery in a pathological states based on the measured stress or strain.

1.4 MECHANICAL BEHAVIOR OF THE ARTERIAL WALL

1.4.1 Biaxial Mechanical Behavior

Soft tissues exhibit large nonlinear deformations and pronounced mechanical anisotropy because of their oriented fibrous structure. In many biomechanical studies only uniaxial testing has been performed due to challenges of controlling two-dimensional (2D) boundary conditions [62]. However, since arteries undergo biaxial loading *in vivo* and exhibit mechanical anisotropy, uniaxial data cannot be utilized to formulate a constitutive model with physiologically relevant model parameters. In the vascular biomechanics literature, there have been many reports of the pressure-diameter relationship of the different vessels through pressurization of the cylindrical arterial wall [11, 63]; in this type of experimental setup the physiological boundary conditions is relatively maintained. However, the regional behavior of the arterial wall cannot be characterized due to the heterogeneity of the arterial wall and the challenges associated with accurately defining the boundary conditions for a complex 3D geometry, such as that of the PA. Thus, this form of experimental setup cannot provide the mechanical data relevant to the purposes of the current study. Henceforth, in the present study a previously developed planar biaxial testing device [64, 65] is utilized to characterize the regional biaxial behavior of the PA during postnatal growth.

1.4.2 Residual Strain

Arteries are thick-walled tubes with very large radius to thickness ratios. During the cardiac cycle, when blood pressure increases, the wall thickness decreases, and the radius-to-thickness

ratio increases. Under this condition, the strain at the inner wall is larger than that at the outer wall. Since the stress-strain relationship is exponential, the stress at the inner wall becomes larger and falls exponentially to a lower value at the outer wall [1]. In 1983, Vaishnav and Vossoughi [66] and Fung [67] noted the presence of circumferential residual strain in arterial walls, revealed through the opening of a transversely cut vessel. In 1986, Chuong and Fung [68] proposed that residual stresses develop in growing arteries to reduce stress gradients in the loaded arterial wall by generating compression at the inner wall and tension at the outer wall (Figure 1.2). In a subsequent study, Takamizawa and Hayashi [69] suggested that strain rather than stress was uniform in the arterial wall under physiological loading condition.

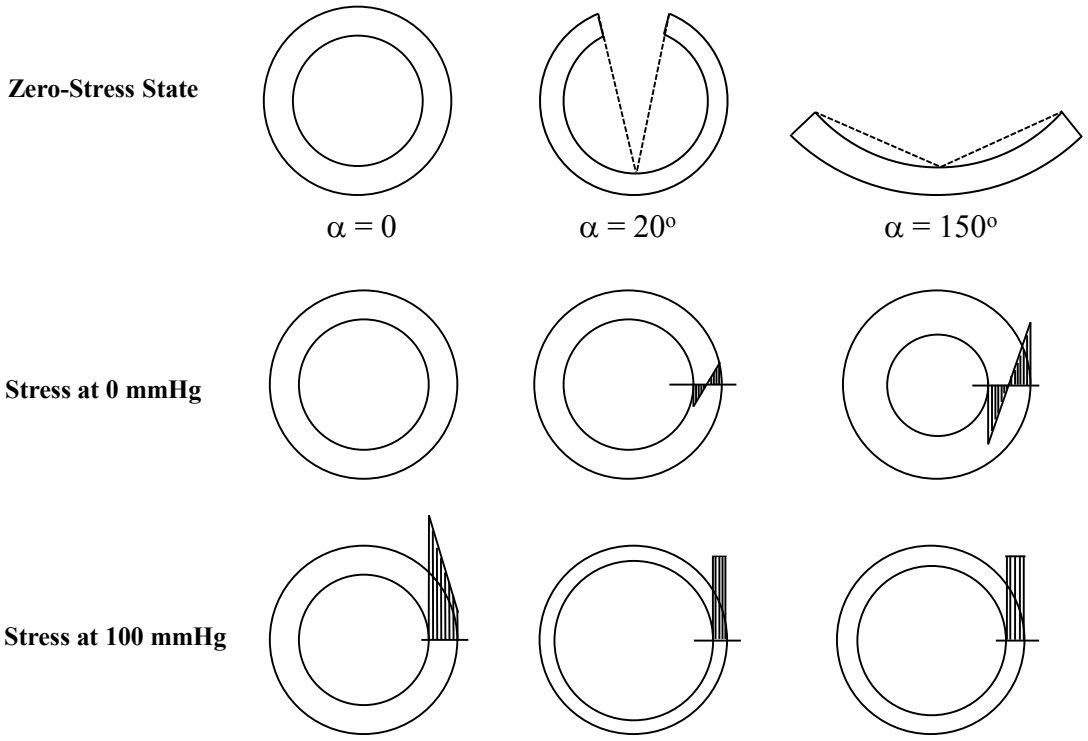

Figure 1.2. Effect of residual strain on the homeostatic stress distribution in blood vessel wall. Circumferential stress distribution in the wall is shown at 0 mmHg and 100 mmHg transmural blood pressure (center and bottom rows) in absence of residual strain (left column) and in presence of increasing residual strain, as shown by opening angle, according to wall thickness in center and right columns, respectively.

Strain and stress distributions in the arterial wall affect the mechanical function of the artery, and can play an important role in the remodeling associated with wall growth and the onset and progression of vascular diseases such as hypertension. In the current study, in order to delineate possible alterations in stress distribution patterns during postnatal maturation, the regional residual strains of the endoluminal and abluminal surfaces of the PA wall are quantified in juvenile and adult age groups.

1.5 STRUCTURE OF THE ARTERIAL WALL

The arterial wall is composed of three lamina: the tunica intima (innermost layer), tunica media (middle layer), and tunica adventitia (outermost layer) (Figure 1.3). The intima is the thinnest layer, consisting of a single layer of endothelial cells (mainly myofibroblasts) and a subendothelial layer composed of elastin, collagen fibers, and smooth muscles cells [11]. The endothelial cells act as a barrier between the thrombogenic media and blood. The elastic sheet demarcating the outermost layer of the aortic tunica intima from the aortic tunica media is termed the internal elastic lamina. The boundary between the tunica intima and media is often not readily defined, and the internal elastic lamina may be the innermost of the many elastic lamellae within the wall. The tunica media is considered to be the most mechanically dominant layer and is comprised of elastic sheets, collagen fibers, and smooth muscle cells [70]. The elastin and collagen fibers are closely associated with each other in the media and are organized into concentric rings of lamella units around the arterial lumen with smooth muscle cells lying between these lamellae [71]. The tunica adventitia is composed of fibroblasts and fibrocytes, ground-matrix, thick bundles of collagen fibers, some elastic fibers, blood vessels (vasa

vasorum), and nerves; it is surrounded by loose connective tissue [70]. The elastic sheets between the tunica intima and tunica media, and the tunica media and tunica adventitia are called the internal and external elastic lamina, respectively (Figure 1.3).

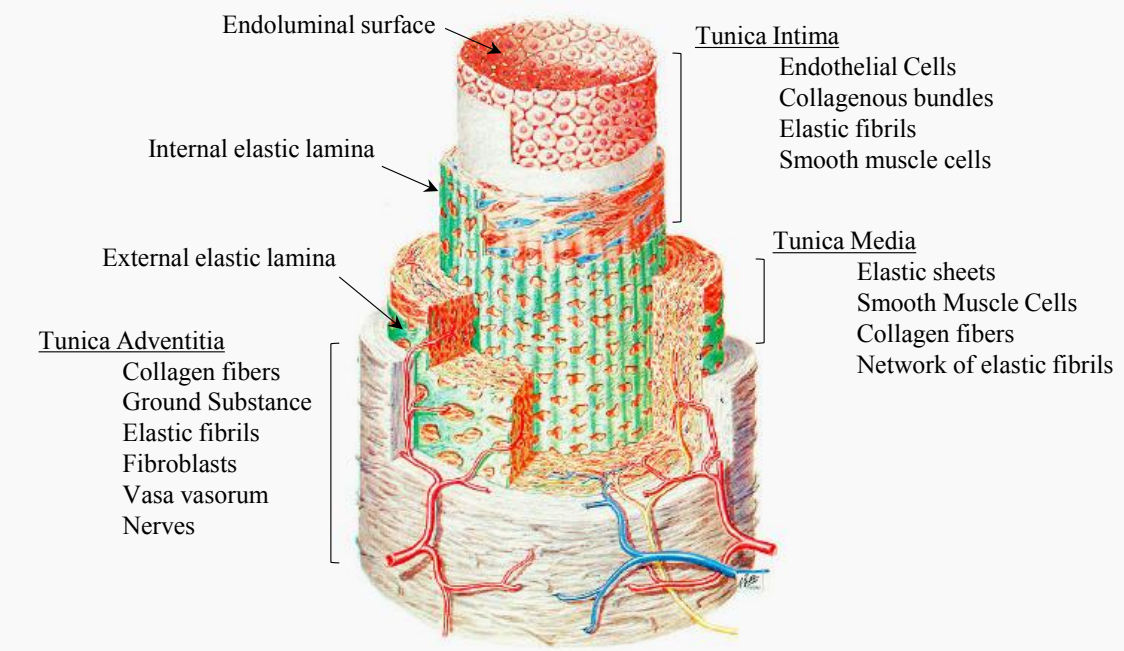

Figure 1.3. Artistic depiction of aortic wall structure.
(http://herkules.oulu.fi/)

Elastin and collagen are the primary structural proteins in the elastic arterial wall and impart the essential mechanical integrity for the artery to modulate the pulsatile cardiac output [72]. The coil and recoil behavior of elastic fibers render the artery its elasticity properties and large-range reversible extensibility. Experiments on single elastic fibers have demonstrated that these fibers do not creep and can endure millions of extension-relaxation cycles without experiencing significant fatigue [73]. Elastic fibers are composed of two morphologically and chemically distinct components: elastin and microfibrils. Elastic fiber is comprised of about 90% elastin, which forms its internal core, and is surrounded by a sheath of unbranched microfibrils

[71]. The highly organized process of elastogenesis, through assembly of fibrillin into microfibrils and the association of microfibrils with tropoelastin, is limited to fetal and early neonatal development [72]. The structure of elastic matrices differs among tissues. Their function is a direct outcome of their composition and organization.

Collagen fibers are composed of three polypeptide chains, each consisting of regions of the repeating amino acid motif Gly-X-Y, where X and Y could be any amino acid. With X and Y amino acids on the surface and Glycine residues inside the core of the protein, the right-handed triple helical structure of the collagen is created. Of the various types of collagen, the fibrillar collagens are the most mechanically significant forms of collagen and widely occur in the vasculature. The three polypeptide chains in a fibrillar collagen molecule are called α chains. Collagen molecules can consist of three identical α chains, termed homotrimeric, or have genetically distinct α chains, termed heterotrimeric. Type III collagen is homotrimeric and Type I collagen is heterotrimeric with two identical α1 chains and a third distinct α2 chain [74]. The medial layer is about 30% Type I and 70% Type III while the adventitia is primarily composed of Type I collagen [75]. The dominant passive mechanical response of the artery is imparted by the medial collagen fibers under physiological conditions [76]. While adventitial collagen may play a role in arterial mechanics, it has been considered to serve primarily as a protective sheath to prevent rupture during hyperinflation, thus the focus of this work is on the media.

In normal fetus, the tunica media of the PA and AA have similar thickness and elastic tissue structure. The relative medial thickness of the PA to AA decreases to between 0.4 and 0.8 from birth until the second year of life [77]. The adult PA elastic tissue is irregular and more sparse than the aorta, and individual lamina are short and not as parallel or uniform [77, 78]. Leung et al [50] studies in the rabbit model during postnatal growth period revealed that the

relative collagen content of the PA surpasses that of the AA while the relative elastin content does not significantly change since birth and is less than the AA.

1.6 MODELING OF THE ARTERIAL WALL MECHANICS

The deformation and stress of materials are linked by constitutive relations, and the functional form of these equations must be experimentally determined. Soft tissue can be characterized by a complex geometry and composite nature as well as a highly non-linear, often anisotropic, finite deformation mechanical behavior. The loading response of anisotropic materials is direction-dependent. For example, in the special case of anisotropy known as orthotropy, there are mutually orthogonal planes of material symmetry. For transversely isotropic materials, there is a single axis of symmetry [79].

For biological materials that only undergo small deformations, such as bone tissue, the principles of linear elasticity can be used [80]. However, for soft tissues, such as arterial tissue, nonlinear approaches must be taken. Many soft tissues are simplified to be nonlinearly elastic or hyperelastic, where the stress state of the material is independent of its loading history. Constitutive modeling based on the hyperelasticity theory under isothermal and adiabatic conditions involves defining a strain energy, or stored energy, function in terms of strain or its invariants.

However, living tissues exhibit complex mechanical behavior and in many ways do not meet the definition of an elastic body. Soft biological tissues show hysteresis or energy dissipation when subjected to cyclic loading and unloading. They display stress relaxation when held at a constant strain, and show creep when held at a constant stress. In order to model the

nonlinear mechanical behavior of soft tissues within the framework of hyperelasticity, certain assumptions need to be made. Since after preconditioning the stress-strain relationship does not vary with the rate of strain, the strain-rate effect is ignored. The stress-strain relationships of loading and unloading curves are treated separately. Each of these curves is considered a pseudoelastic curve with the corresponding strain-energy function called the pseudo strain-energy function [11].

1.6.1 Phenomenological Constitutive Models

Phenomenological constitutive models do not have a structural basis and aim at capturing as well as predicting the bulk response of the tissue. Fung postulated the first model for soft tissue mechanics [81, 82], in which a strain energy function of exponential form was defined to capture the nonlinear behavior. In 1987, Humphrey and Yin [83] presented a model that was a combination of phenomenological and structural approaches, where the strain energy function was expressed in terms of separated matrix and fibrous contributions. In 1998, Holzapfel and Weizsacker [84] proposed an additive phenomenological strain function for passive arterial wall mechanics by introducing a decoupled neo-Hookean strain energy function [85] for the "isotropic" "elastin-dominated" rubber-like response with the Fung model for the anisotropic "collagen-dominated" fabric-like response. In 2000, Holzapfel and Gasser [86], modeled the arterial wall as a two-layer (media and adventitia) thick-walled tube by assigning separate material parameters for each layer with the same form of a Fung-type strain energy function.

1.6.2 Structural Constitutive Models

The mechanical loading-deformation relation of elastin and collagen fibril bundles is fundamental to understanding the underlying microstructural mechanisms of tissue behavior. Structurally motivated models incorporate significant mechanical aspects of the underlying microstructure to better predict the mechanical behavior and understand the mechanisms governing the structure-function relationship of biological tissues. In 1957, Roach and Burton [87] studied the mechanical roles of collagen and elastin in the arterial wall loading response and provided indirect evidence that elastin fibers primarily carry the mechanical load at low pressures, while at higher pressures collagen is the chief load bearing constituent. They demonstrated that the slope of the elastin-depleted arterial wall loading curve was significantly altered at low pressures while it was relatively preserved in the higher pressure region. Additionally, the unloaded radius of the artery increased after removal of elastin. Thus, they inferred that elastic fibers are primarily responsible for resisting deformation at low pressures and do not play a major role at higher pressures. On the other hand, after chemical degradation of collagen, the arterial wall compliance significantly increased at high pressure while the initial radius of the artery decreased. They claimed that "at low pressures, only the elastic fibers have reached their unstretched length, but as the pressure is increased, more and more of the collagenous fibers of the 'fibrous jacket' reach their unstretched length." Therefore, the passive mechanical response of the artery wall has been assumed to be governed by isotropic elastin fibers in the initial loading region while the crimped circumferentially-oriented medial collagen fibers gradually unfurl and begin carrying load under increasing pressure [87, 88].

In 1979, Lanir [89] originally formulated a structurally motivated model for flat collagenous tissues where the passive tissue response was considered to be the result of additive

responses of its two primary constituents: linearly elastic individual elastin and collagen fibers. Nonlinearity was introduced by variation in fibers' undulation or recruitment in a given fiber orientation. Lanir's model allowed for the direct incorporation of recruitment and the orientation distribution of collagen fibers [89, 90]. This model has been modified and applied to various biological tissues [91-93].

Liao and coworkers [94] used the small angle light scattering technique coupled with a planar biaxial mechanical device for direct analysis of kinematics of gross fiber angular distribution of heart valve tissue under biaxial loading, with the results directly incorporated into Lanir's model [93]. Wognum et al. [91, 95] modified Lanir's model to include the mechanical contribution of smooth muscle cells and applied this multiphase model to the study of bladder wall remodeling after spinal cord injury. Hill and colleagues [92] combined a uniaxial loading device with multiphoton microscopy (section 5.2.1) to quantify the collagen structure and recruitment behavior of the carotid artery. They directly incorporated both experimental measurements into Lanir's model and compared their findings with previous assumptions on collagen recruitment behavior.

1.7 SPECIFIC AIMS

The overall objective of this work is initially to establish the benchmarks for tissue engineering approaches. Moreover, by enhancing our knowledge of alterations in the structure-mechanics relationship of the main pulmonary artery during postnatal maturation, help begin elucidating the governing mechanisms of the normal remodeling and growth process. For the majority of this study, Dorset Ovine is used as the animal model of choice for having a cardiovascular system

similar to that of humans and a relatively fast growth rate that allows a feasible timeframe for such a study. The study objective is divided into the following three specific aims:

1. Quantify local postnatal alterations in surface geometry of the PA and AA to determine the effects of physical connections between these adjacent arteries on their respective surface shapes and to provide the basis for the rest of the study.
2. Quantify the regional growth adaptations of the mechanical behavior and microstructural properties to determine the relationship between mechanics and microstructure; this is achieved by
    A. Characterizing regional biaxial behavior and residual strain patterns.
    B. Quantifying elastin organization, and collagen structure and recruitment behavior.
3. Develop a modified structural constitutive model of the arterial fibrous tissue to incorporate all the measured structural data.

All the experimental data along with the constitutive model will help delineate the structure-function relationship of arterial wall and help begin elucidating mechanisms behind regional modifications of mechanics in normal postnatal remodeling and growth of the pulmonary arterial wall.

This thesis is further divided as follows. The formulations for nonlinear deformation and stress analysis used in continuum mechanics are described in Chapter 2.0. The goals set in the first specific aim are fulfilled by the work presented in Chapter 3.0. To achieve part A of the second specific aim, the regional mechanical properties are investigated in Chapter 4.0 using a biaxial mechanical testing device and a residual strain measurement setup. To fulfill the goals sets in the specific aim 2B, in Chapter 5.0, the regional elastin fiber orientation distribution is quantified in the multiphoton images of stress-free sections of the pulmonary arterial wall.

Subsequently, in Chapter 6.0, a coupled multiphoton microscope-biaxial stretching system is used to quantify postnatal alterations in the collagen structure and recruitment behavior. The measured elastin and collagen structure as well as the collagen recruitment data are then directly incorporated into a modified structural constitutive model as explained in Chapter 7.0.

2.0 NONLINEAR THEORY OF ELASTICITY AND SOFT TISSUE MECHANICAL MODELS

The two important measures in a material's mechanical behavior are stress, defined in its simplest form as force divided by the area it is acting on, and stretch or strain, measures of a change in length upon loading. In the case of finite deformations, several different definitions of stress and strain are used. In this chapter the definitions of stress and strain in the context of nonlinear elasticity are presented. Also included is a summary of laws of thermodynamics and physical principles that impose a framework on the form of a constitutive model. Finally, an overview of previously developed soft tissue mechanical models is given.

2.1 GENERAL ANALYSIS OF DEFORMATION

Soft tissues often undergo "large" or "finite" deformation, which introduces geometric nonlinearity into the analysis even if the material properties are linear. This section deals only with geometry; discussion on material nonlinearity due to nonlinear stress-strain relation will follow in next sections. The nonlinear deformation principles have been applied to quantify mass accretion or change in geometry in the studies of tissue growth and remodeling (Section 2.4.4). Thus, the derived equations in this section will be used in estimating surface growth deformation

patterns (Chapter 3.0). The content of this section is based on the Chapter 3 of the book by Larry Taber on the "Nonlinear Theory of Elasticity: Applications in Biomechanics" [96].

2.1.1 Coordinate Systems and Base Vectors

The point P in the reference (or undeformed) state on a body Ω_o at time t=0 becomes point p in the deformed body Ω_t at time t (Figure 2.1). The point P is located in the material or Lagrangian curvilinear coordinate system X^I, and p is located in the spatial or Eulerian curvilinear coordinate system x^i. In a general case, the coordinate system X^I and x^i are defined with respect to two difference reference frames O and o, that could be moving relative to each other. The X^I and x^i coordinate systems can be kept separate to take advantage of any symmetry in Ω_o and Ω_t. The X^I system can also be assumed to be embedded in Ω_o so that it deforms with the body resulting in each point keeping the same coordinate label during the motion, and the $x^i = X^I$ are called convected coordinates.

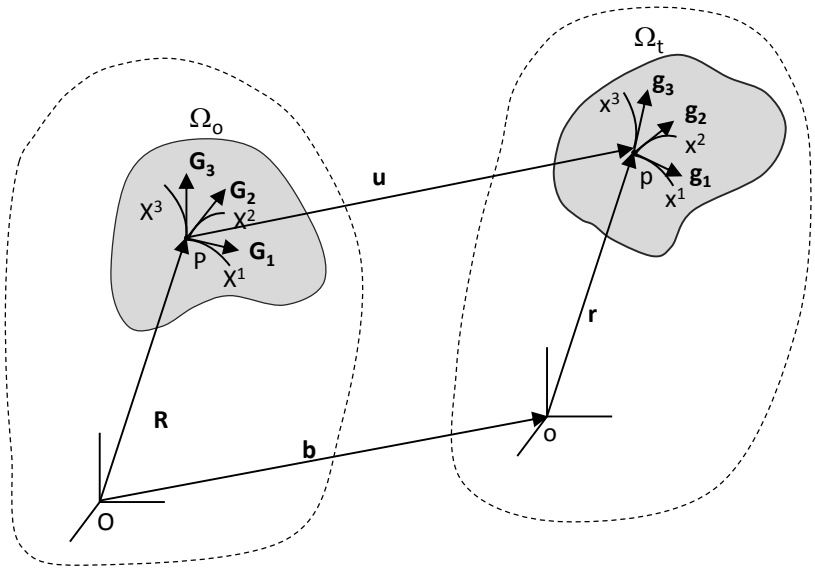

Figure 2.1. Coordinates and base vectors in undeformed body Ω_o and deformed body Ω_t.

The position vectors to P and p are $\mathbf{R}(X^I, t)$ and $\mathbf{r}(x^i, t)$, respectively. Then, the mapping of P into p and the inverse mapping are defined according to

$$\mathbf{r} = \mathbf{r}(\mathbf{R}, t), \quad \mathbf{R} = \mathbf{R}(\mathbf{r}, t), \tag{2.1}$$

respectively, which imply

$$\mathbf{r} = \mathbf{r}(x^i, t) = \mathbf{r}(X^I, t), \quad \mathbf{R} = \mathbf{R}(X^I, t) = \mathbf{R}(x^i, t). \tag{2.2}$$

The covariant base vectors in Ω_o are

$$\mathbf{G}_I = \frac{\partial \mathbf{R}}{\partial X^I} = \mathbf{R}_{,I} \tag{2.3}$$

and the two sets of covariant base vectors in Ω_t are

$$\begin{aligned} \mathbf{g}_I &= \frac{\partial \mathbf{r}}{\partial X^I} = \mathbf{r}_{,I} \\ \mathbf{g}_i &= \frac{\partial \mathbf{r}}{\partial x^i} = \mathbf{r}_{,i} \end{aligned}. \tag{2.4}$$

The $\mathbf{G}_I$ are tangent to the X^I coordinate curves at P, the $\mathbf{g}_i$ are tangent to the x^i coordinates curves at p (Figure 2.1), and the $\mathbf{g}_I$ are tangent to the convected X^I coordinate curves at p. Eqs. (2.3) and (2.4) give the differential line element vectors as

$$\begin{aligned} d\mathbf{R} &= \mathbf{G}_I dX^I \\ d\mathbf{r} &= \mathbf{g}_I dX^I = \mathbf{g}_i dx^i \end{aligned}. \tag{2.5}$$

2.1.2 Deformation Gradient Tensor

The deformation gradient tensor $\mathbf{F}$ is defined to be the tensor that transforms a differential line element $d\mathbf{R}$ in the undeformed body Ω_o into $d\mathbf{r}$ in the deformed body Ω_t (Figure 2.2) as follows

$$d\mathbf{r} = \mathbf{F} \cdot d\mathbf{R} = d\mathbf{R} \cdot \mathbf{F}^T. \tag{2.6}$$

The inverse of the deformation gradient tensor $\mathbf{F}^{-1}$ maps transformation from Ω_o relative to Ω_t according to

$$d\mathbf{R} = \mathbf{F}^{-1} \cdot d\mathbf{r} = d\mathbf{r} \cdot \mathbf{F}^{-T}. \tag{2.7}$$

Based on these equations, the deformation gradient tensor can be obtained through

$$\begin{aligned} \mathbf{F}^{T} &= \frac{\partial \mathbf{r}}{\partial \mathbf{R}} \\ \mathbf{F}^{-T} &= \frac{\partial \mathbf{R}}{\partial \mathbf{r}} \end{aligned}. \tag{2.8}$$

In order to define these tensors in terms of base vectors, we can substitute Eqs. (2.5) into (2.8) as follows

$$\begin{aligned} \mathbf{F}^{T} &= \frac{\partial \mathbf{r}}{\partial \mathbf{R}} = \frac{\mathbf{g}_I dX^I}{\mathbf{G}_J dX^J} = \mathbf{G}^J \mathbf{g}_I \delta^I_J = \mathbf{G}^I \mathbf{g}_I \\ \mathbf{F}^{-T} &= \frac{\partial \mathbf{R}}{\partial \mathbf{r}} = \frac{\mathbf{G}_J dX^J}{\mathbf{g}_I dX^I} = \mathbf{g}^I \mathbf{G}_J \delta^J_I = \mathbf{g}^I \mathbf{G}_I \end{aligned}, \tag{2.9}$$

where

$$\delta^I_J = \begin{cases} 1 \text{ for } I = J \\ 0 \text{ for } I \neq J \end{cases}$$

is the Kronecker delta.

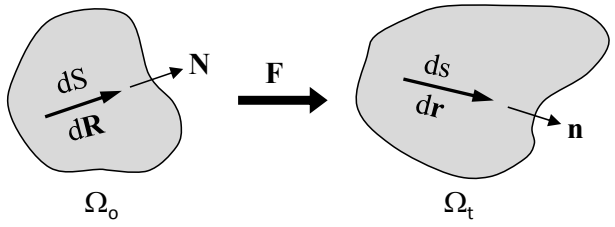

Figure 2.2. Deformation of line element dR into line element dr.

2.1.3 Deformation and Strain Tensors

The deformation gradient tensor includes rigid-body motion, and it also is non-symmetric resulting in nine parameters, that all may not be known in some problems. Hence, **F** is modified to represent only deformation or change in length according to

$$\begin{aligned} \mathbf{C} &= \mathbf{F}^{\mathrm{T}} \cdot \mathbf{F} \\ \mathbf{B} &= \mathbf{F} \cdot \mathbf{F}^{\mathrm{T}} \end{aligned}, \tag{2.10}$$

where **C** and **B** are the right and left Cauchy-Green deformation tensors, respectively; both of these tensors are symmetric ($\mathbf{C}^{\mathrm{T}}=\mathbf{C}$ and $\mathbf{B}^{\mathrm{T}}=\mathbf{B}$). We can now define the Lagrangian and Eulerian strain tensor as follows

$$\begin{aligned} 2\mathbf{E} &= \mathbf{C} - \mathbf{I} = \mathbf{F}^{\mathrm{T}} \cdot \mathbf{F} - \mathbf{I} \\ 2\mathbf{e} &= \mathbf{I} - \mathbf{B}^{-1} = \mathbf{I} - \mathbf{F}^{-\mathrm{T}} \cdot \mathbf{F}^{-1} \end{aligned}. \tag{2.11}$$

2.1.4 Geometric Measures of Deformation

In order to report regional deformation of a tissue, we need to define more physically meaningful measures of deformation than the deformation gradient and strain tensors, which characterize deformation of a body. The stretch or stretch ratio has a direct physical interpretation by describing the deformation of differential element dS into differential element ds. The stretch ratio ds/dS depends on the specific orientation of the deformed or the undeformed element. The Lagrangian stretch ratio $\lambda_{N)}$ measures the deformation of an element in the direction of **N** in the undeformed body Ω_o, and the Eulerian stretch ratio $\lambda_{(n)}$ computes the deformation of element **n** in the deformed body Ω_t, where both **N** and **n** are unit vectors.

The differential vector elements in the undeformed and deformed states are defined according to

$$d\mathbf{R} = \mathbf{N}\, dS, \qquad d\mathbf{r} = \mathbf{n}\, ds \tag{2.12}$$

where d**r** does not necessarily correspond to the deformed d**R**. By substituting into Eqs. (2.6) and (2.7), we can write

$$\mathbf{n}\, ds = \mathbf{F}\cdot\mathbf{N}\, dS \qquad \text{or} \qquad \mathbf{N}\, dS = \mathbf{F}^{-1}\cdot\mathbf{n}\, ds, \tag{2.13}$$

which, when divided by dS, result in the following relations

$$\mathbf{n}\,\lambda_{(N)} = \mathbf{F}\cdot\mathbf{N} = \mathbf{N}\cdot\mathbf{F}^{T} \tag{2.14}$$

$$\mathbf{N}\,\lambda_{(n)}^{-1} = \mathbf{F}^{-1}\cdot\mathbf{n} = \mathbf{n}\cdot\mathbf{F}^{-T}. \tag{2.15}$$

With **N** and **n** being unit vectors, we can write

$$\lambda_{(N)}^{2} = (\mathbf{n}\,\lambda_{(N)})\cdot(\mathbf{n}\,\lambda_{(N)}) = (\mathbf{N}\cdot\mathbf{F}^{T})\cdot(\mathbf{F}\cdot\mathbf{N})$$

$$\lambda_{(n)}^{-2} = (\mathbf{N}\,\lambda_{(n)}^{-1})(\mathbf{N}\,\lambda_{(n)}^{-1}) = (\mathbf{n}\cdot\mathbf{F}^{-T})\cdot(\mathbf{F}^{-1}\cdot\mathbf{n}),$$

and based on Eqs.(2.10), we obtain

$$\begin{aligned} \lambda_{(N)}^{2} &= \mathbf{N}\cdot\mathbf{C}\cdot\mathbf{N} \\ \lambda_{(n)}^{-2} &= \mathbf{n}\cdot\mathbf{B}^{-1}\cdot\mathbf{n} \end{aligned}. \tag{2.16}$$

2.1.5 Principal Strains: The Eigenvalue Problem

At any point in a body, a unique set of orthogonal axes can be defined relative to which shear strains disappear. These axes are called principal axes of strain, and strains along these axes are principal strains. In order to compute the principal strains the eigenvalue problem has to be

solved. The principal stretch ratios $\lambda_{(N_i)}$ and $\lambda_{(n_i)}$ (i=1,2,3) and the corresponding principal axes $\mathbf{N}_i$ and $\mathbf{n}_i$ should satisfy the following eigenvalue problem

$$\begin{aligned} \mathbf{N}\cdot\mathbf{C} &= \lambda_{(N)}^2\ \mathbf{N} \\ \mathbf{n}\cdot\mathbf{B}^{-1} &= \lambda_{(n)}^{-2}\ \mathbf{n} \end{aligned},$$

which can be re-written as

$$\begin{aligned} (\mathbf{C}-\lambda_{(N)}^2\ \mathbf{I})\cdot\mathbf{N} &= 0 \\ (\mathbf{B}-\lambda_{(n)}^2\ \mathbf{I})\cdot\mathbf{n} &= 0 \end{aligned}. \tag{2.17}$$

It can be demonstrated that **C** and **B** have real eigenvalues and mutually orthogonal eignevectors. As **n** is in the direction of the deformed element with undeformed orientation **N**, $\lambda_{(n)} = \lambda_{(N)}$, thus, the eigenvalues of **C** and **B** are equal.

2.2 DEFINITION OF STRESS

In the case of larger deformation, because undeformed and deformed geometries are different, the only meaningful definition for stress is force per unit deformed area, which is called true stress or Cauchy stress. The Cauchy stress tensor $\boldsymbol{\sigma}$ is derived from the traction vectors acting on a body's surfaces in the deformed configuration. The deformed geometry of a solid body, however, often is difficult to measure and may be time-dependent. Therefore, another measure of stress is defined as the force per unit undeformed (reference) area, which is termed the engineering stress or Lagrangian stress. The Lagrangian stress tensor, also called the 1st Piola Kirchhoff stress tensor **P**, is defined in the referential configuration and is related to the Cauchy stress tensor according to

$$\mathbf{P} = J\mathbf{F}^{-1}\boldsymbol{\sigma}\,, \tag{2.18}$$

where $\mathbf{F}^{-1}$ is inverse of deformation gradient tensor, and J (Jacobian) is the change in an infinitesimal volume element from the reference (dV_0) to the deformed configuration (dV) defined as $J = dV/dV_0 = \det(\mathbf{F})$, which based on conservation of mass is equivalent to $J = \rho/\rho_0 = \det(\mathbf{F})$; here, ρ and ρ_0 are the tissue densities in the current configuration and reference configurations, respectively, and $\det(\mathbf{F})$ is the determinant of $\mathbf{F}$.

The governing equations may be easier to solve if written in terms of yet another type of stress called the 2nd Piola Kirchhoff stress tensor **S**, which has no direct physical meaning. **S** is a symmetric tensor, unlike **P**, and is related to $\boldsymbol{\sigma}$ and **P** as follows

$$\mathbf{S} = J\mathbf{F}^{-1}\boldsymbol{\sigma}\mathbf{F}^{-\mathrm{T}} = \mathbf{P}\mathbf{F}^{-\mathrm{T}}; \tag{2.19}$$

thus, **P** can also be written in term of **S** as $\mathbf{P} = \mathbf{F}\mathbf{S} = \mathbf{S}\mathbf{F}^{\mathrm{T}}$.

2.3 THERMODYNAMIC LAWS AND FUNDAMENTAL CONSTITUTIVE PRINCIPLES

The functional form of a constitutive model for a thermomechanical continuum should be bounded by the laws of thermodynamics. In a thermomechanical material, thermal and mechanical effects dominate the material's behavior and electrical, chemical and other effects are ignored [96]. The following text is largely based on ref [96], Chapter 5. The first law of thermodynamics deals with conservation of energy. For a thermomechanical continuum, the principle of conservation of energy can be written in the form

$$\dot{K} + \dot{U} = \dot{P} + \dot{Q}\,, \tag{2.20}$$

where K is the kinetic energy, U the internal energy (consists of thermal energy and strain energy), P the mechanical power input (the rate of work done on a body by applied loads) and Q the rate of heat input. The left side represents changes in internal energy, the right side energy that is added externally.

For an arbitrary volume element that deforms from dV_0 into dV, Eq.(2.20), written in the local form, and in terms of the Cauchy stress tensor $\boldsymbol{\sigma}$, or the first Piola Kirchhoff stress tensor $\mathbf{P}$, respectively, the first law can be formulated as

$$\begin{aligned} \rho\dot{u} - \boldsymbol{\sigma} : \mathbf{D} - \rho r + \tilde{\nabla} \cdot \mathbf{q} = 0 \\ \rho_0\dot{u} - \mathbf{P} : \dot{\mathbf{F}}^{\mathrm{T}} - \rho_0 r + \nabla \cdot \mathbf{q}_0 = 0 \end{aligned} . \tag{2.21}$$

In this, the following definitions hold: ρ and ρ_0 are, respectively, the mass densities in the current and reference configurations; u is the internal energy per unit mass; $\mathbf{D}$ is the rate-of-deformation tensor; $\mathbf{F}$ is the deformation gradient tensor; r is the rate of heat production per unit mass due to internal sources; $\mathbf{q}$ and $\mathbf{q}_0$ the outward-directed heat flux vectors per unit deformed and undeformed surface area, respectively, with ∇ and $\tilde{\nabla}$ being their corresponding gradient operators. According to Eq. (2.21), the first law of thermodynamics states that the rate of increase in internal energy of a volume element ($\rho\dot{u}$ or $\rho_0\dot{u}$) is equal to the sum of the rate of work done by the stresses on the element, i.e. the stress power ($\boldsymbol{\sigma} : \mathbf{D}$ or $\mathbf{P} : \dot{\mathbf{F}}^T$), the rate of internal heat production (ρr or $\rho_0 r$), and the rate of heat flow into the element ($-\tilde{\nabla} \cdot \mathbf{q}$ or $-\nabla \cdot \mathbf{q}_0$).

The first law of thermodynamics basically states that conversion of work to heat, and vice versa, is reversible in a closed system; hence, the total energy remains constant. However, it does not consider the irreversible processes or dissipated energy. The second law of thermodynamics restricts the direction of energy conversion processes and is based on the concept of entropy (Σ). For a solid body, the second law of thermodynamics states that the time-

rate of change of the total entropy in a body is greater than or equal to the sum of the influx of entropy through the surface of the body and the entropy generated by internal heat sources. The Lagrangian local forms of this relation, which is also called the Clausius-Duhem inequality, is given by

$$\dot{\Sigma} - \frac{r}{T} + \frac{1}{\rho_0} \nabla \cdot \left(\frac{\mathbf{q}_0}{T} \right) \geq 0 , \tag{2.22}$$

where T is the absolute temperature.

The possible forms for thermomechanical constitutive equations are restricted by the above thermodynamic considerations and by the following physical principles: *coordinate invariance*, *determinism*, *local action*, *equipresence*, *material objectivity*, *physical admissibility*, and *material symmetry*.

The principle of *material symmetry* is used to develop specific forms of constitutive equations based on a given material directionality or symmetry, such as orthotropy or transverse isotropy, which are often used to characterize soft tissues.

The principle of *coordinate invariance* states that constitutive equations must be independent of the coordinate system that is used to describe the motion of a body, thus, should be developed in tensor form.

The principle of *determinism* states that the stress distribution in a body at a given time depends on the entire history of deformation and temperature. In the case of an ideal elastic material however, there is no energy dissipation and usually temperature effects are ignored; thus, the stress at time t depends only on the instantaneous deformation.

The principle of *local action* indicates that the motion and temperature of an arbitrary point in a thermoelastic body can be determined from the values and the spatial derivatives of

these variables at a nearby point. For simple materials, this principle together with the principle of determinism, suggest that the constitutive equations for a thermoelastic material can be written in the form

$$\begin{aligned} \boldsymbol{\sigma} &= \boldsymbol{\sigma}\left(\mathbf{R},\mathbf{F},T,\nabla T\right) \\ \mathbf{q} &= \mathbf{q}\left(\mathbf{R},\mathbf{F},T,\nabla T\right) \\ u &= u\left(\mathbf{R},\mathbf{F},T,\nabla T\right) \\ \Sigma &= \Sigma\left(\mathbf{R},\mathbf{F},T,\nabla T\right) \end{aligned}, \tag{2.23}$$

where **R** is position vector to two nearby points in the undeformed body.

The principle of *equipresence* states that an independent variable that appears in one constitutive equation for a material, must be present in all constitutive equations for that material. This principle needs to be applied if other effects, such as electrical or chemical, are to be included.

The principle of *material objectivity* or *material frame indifference* states that the *form* of constitutive equations must remain unchanged under rigid motions of the spatial reference frame. In other words, the events occurring at a point in a body must be independent of the motion of the observer. The deformation gradient tensor **F** is per definition an objective quantity, since it describes changes in length and angle relative to a given reference configuration. Under a change of reference frame, the frame invariance of **F** implies that it transforms to $\mathbf{F}^*$ through the rotation tensor **Q**, as $\mathbf{F}^* = \mathbf{Q}\cdot\mathbf{F}$. The contact forces within a body are frame indifferent, so are the differential areas on which they act, it follows that Cauchy stress tensor is an objective quantity. The second order tensors are objective because a general second order tensor **T** transforms as $\mathbf{T}^* = \mathbf{Q}\cdot\mathbf{T}\cdot\mathbf{Q}^T$. Since deformation and temperature are objective, the constitutive relations for a thermoelastic material (Eq. (2.23)) are frame indifferent. Based on the principle of material frame indifference, the constitutive equations can take the forms

$$\begin{aligned} \boldsymbol{\sigma} &= \boldsymbol{\Theta} \cdot g_{(\sigma)}(\mathbf{U}) \cdot \boldsymbol{\Theta}^{\mathrm{T}} \\ \text{or } \boldsymbol{\sigma} &= \boldsymbol{\Theta} \cdot f_{(\sigma)}(\mathbf{C}) \cdot \boldsymbol{\Theta}^{\mathrm{T}} \,, \\ \text{or } \boldsymbol{\sigma} &= \boldsymbol{\Theta} \cdot h_{(\sigma)}(\mathbf{E}) \cdot \boldsymbol{\Theta}^{\mathrm{T}} \end{aligned} \tag{2.24}$$

where $\mathbf{Q} = \boldsymbol{\Theta}^{\mathrm{T}}$, g, f and h are called response functions, and $\mathbf{U}$ is the right stretch tensor which is obtained through polar decomposition of $\mathbf{F}$ ($\mathbf{F} = \mathbf{Q} \cdot \mathbf{U}$). Using the conversion definition of stress measures (Eq. (2.19)), this eventually states

$$\begin{aligned} \mathbf{S} &= g_{(s)}(\mathbf{U}) \\ \text{or } \mathbf{S} &= f_{(s)}(\mathbf{C}) \,. \\ \text{or } \mathbf{S} &= h_{(s)}(\mathbf{E}) \end{aligned} \tag{2.25}$$

These relations, in terms of second Piola-Kirchhoff stress tensor, are convenient to work with since rotation does not appear explicitly.

The principle of *physical admissibility* states that constitutive equations must be consistent with any of the basic laws of continuum mechanics, including the first and second laws of thermodynamics, Eqs. (2.21) and (2.22). Stating these equations in terms of the 2nd Piola Kirchhoff stress $\mathbf{S}$ and eliminating r between these two equations yields

$$\rho_0 \left(T\dot{\Sigma} - \dot{u} \right) + \mathbf{S} : \dot{\mathbf{E}} = 0 \,. \tag{2.26}$$

Eq. (2.26) can now be combined with the general constitutive equations in Eq. (2.23) and the case for which temperature is considered to be the independent variable. It is convenient to introduce the Helmholtz free energy function

$$\psi = u - T\Sigma \,, \tag{2.27}$$

as a replacement for the internal energy u. Then, Eq. (2.23) is substituted by

$$\psi = \psi\left(\mathbf{R}, \mathbf{E}, T, \nabla T \right) , \tag{2.28}$$

and using Eq. (2.27) to eliminate u in Eq. (2.26) yields

$$-\rho_0\left(\dot{\psi}+\Sigma\dot{T}\right)+\mathbf{S}:\dot{\mathbf{E}}=0. \tag{2.29}$$

Combining Eqs. (2.28) and (2.29), and using the chain rule gives

$$\left(\mathbf{S}-\rho_0\frac{\partial\psi}{\partial\mathbf{E}}\right):\dot{\mathbf{E}}-\rho_0\left(\Sigma+\frac{\partial\psi}{\partial T}\right)\dot{T}-\rho_0\frac{\partial\psi}{\partial\nabla T}\cdot\nabla\dot{T}=0. \tag{2.30}$$

For independent strain and temperature distributions, this equation implies the relations

$$\begin{aligned}\mathbf{S}&=\rho_0\frac{\partial\psi}{\partial\mathbf{E}}\\ \Sigma&=-\frac{\partial\psi}{\partial T}\\ \frac{\partial\psi}{\partial\nabla T}&=0\end{aligned}. \tag{2.31}$$

If the deformation is isothermal ($\dot{T}=0$), then $\psi=\psi(\mathbf{R},\mathbf{E})$, meaning the material behaves purely elastically. This relation suggests that during an isothermal deformation, the strain energy is zero in the reference state or in absence of any deformation. In this case, a strain energy density function Ψ is defined as

$$\Psi(\mathbf{R},\mathbf{E})=\rho_0\psi, \tag{2.32}$$

per unit undeformed volume. Since the density ρ_0 of the undeformed body is independent of deformation, Eq. (2.31) gives the constitutive equation

$$\mathbf{S}=\frac{\partial\Psi}{\partial\mathbf{E}}, \tag{2.33}$$

where the 2nd Piola Kirchhoff stress tensor is derived from the scalar strain energy density function Ψ (Note that in the rest of this dissertation, Ψ will be referred to only as strain energy function). A material possessing a constitutive relation of the form (2.33) is called a hyperelastic material, implying that the mechanical properties of the hyperelastic material are characterized

completely by a scalar strain-energy function. The relation (2.33) can be defined in terms of the Cauchy and first Piola-Kirchhoff stress tensors, by using Eqs. (2.19), according to

$$\begin{aligned} \boldsymbol{\sigma} &= J^{-1}\mathbf{F}\cdot\frac{\partial\Psi}{\partial\mathbf{E}}\cdot\mathbf{F}^{\mathrm{T}} \\ \mathbf{P} &= \frac{\partial\Psi}{\partial\mathbf{E}}\cdot\mathbf{F}^{\mathrm{T}} \end{aligned} \quad . \tag{2.34}$$

Under the assumption of pseudoelasticity, the strain energy function Ψ should be technically referred to as a pseudo-strain energy function (Section 1.6). In the rest of this dissertation, however, the general term "strain energy" is used.

Most biological tissues are considered nearly incompressible (isovolumetric) because of their high water content. The work done by a pressure load is due to pressure acting through a change in volume. Since a perfectly incompressible material undergoes no volume change (J = det($\mathbf{F}$) = 1), the hydrostatic pressure does not impart any energy. As a result, for a given strain field in an incompressible material, the constitutive relations resolve the state of stress only up to an arbitrary function $-p\mathbf{I}$, where p is called the Lagrange multiplier and is analogous to hydrostatic pressure. For $J=1$, Eq. (2.34) is modified according to

$$\boldsymbol{\sigma} = \mathbf{F}\cdot\frac{\partial\Psi}{\partial\mathbf{E}}\cdot\mathbf{F}^{\mathrm{T}} - p\mathbf{I}\,, \tag{2.35}$$

which is the general constitutive relation for an incompressible hyperelastic material. Substituting this equation and J=1 into Eqs. (2.18) and (2.19) yields the corresponding relations for Piola-Kirchhoff stress tensor

$$\begin{aligned} \mathbf{P} &= \mathbf{F}^{-1}\cdot\boldsymbol{\sigma} = \frac{\partial\Psi}{\partial\mathbf{E}}\cdot\mathbf{F}^{\mathrm{T}} - p\mathbf{F}^{-1} \\ \mathbf{S} &= \mathbf{F}^{-1}\cdot\boldsymbol{\sigma}\cdot\mathbf{F}^{-\mathrm{T}} = \frac{\partial\Psi}{\partial\mathbf{E}} - p\mathbf{F}^{-1}\cdot\mathbf{F}^{-\mathrm{T}} \end{aligned} \quad . \tag{2.36}$$

Based on the definition of the right Cauchy-Green deformation tensor (Eq. (2.10)) the relation for the 2nd Piola-Kirchhoff stress tensor of an incompressible hyperelastic material can be stated as

$$\mathbf{S} = \frac{\partial \Psi}{\partial \mathbf{E}} - p\mathbf{C}^{-1} \tag{2.37}$$

2.4 MECHANICAL MODELS OF SOFT TISSUES

2.4.1 Governing Equations in Biaxial Stretching of a Membrane

The form of Ψ is not known *a priori* for nonlinear elastic materials, and characterizing mechanical properties requires data from various loading protocols. Unless the structure is one-dimensional, e.g. tendon, uniaxial testing alone is not adequate. At the very least biaxial testing is required to determine material properties of most soft tissues, such as artery, myocardium and pericardium, which experience multiaxial loading *in vivo*.

Arterial tissue is often modeled as transversely isotropic based on the assumption that structural components mainly lie in the plane of the arterial wall. In the biaxial stretching of a rectangular block of membranous tissue undergoing uniform extension in the x_1x_2-plane (Figure 2.3), the boundary conditions are: $P_{11}=P_1$, $P_{22}=P_2$ (with $P_{13} = P_{23} = P_{33} = 0$). If the tissue is transversely isotropic with fibers aligned in the X_1 direction, shear strain are negligible, and the deformation gradient and Lagrangian strain components are, respectively, given by

$$\begin{aligned} [F_I^i] &= diag[\lambda_1, \lambda_2, \lambda_3] \\ [E_{IJ}] &= diag\left[\frac{1}{2}(\lambda_1^2 - 1), \frac{1}{2}(\lambda_2^2 - 1), \frac{1}{2}(\lambda_3^2 - 1)\right], \end{aligned} \tag{2.38}$$

where λ_i are stretch ratios. For an incompressible material, $\lambda_3 = \dfrac{1}{\lambda_1\lambda_2}$ since $\det(\mathbf{F}) = \lambda_1\lambda_2\lambda_3 = 1$.

Since the x_i are aligned with material principal axes, shear stresses can be considered negligible, consequently, there is no disadvantage in working with Piola-Kirchhoff stress tensor since it is symmetric. The constitutive relation $(2.36)_1$ yields

$$P_{II} = \frac{\partial \Psi}{\partial E_{II}} F_{II} - p(F_{II})^{-1} \quad \text{(I not summed)}, \tag{2.39}$$

with $P_{IJ} = 0$ for $I \neq J$ .The first term involving can be simplified by (2.38) using

$$\frac{\partial \Psi}{\partial \lambda_I} = \frac{\partial \Psi}{\partial E_{II}} \frac{\partial E_{II}}{\partial \lambda_I} = \frac{\partial \Psi}{\partial E_{II}} \lambda_I = \frac{\partial \Psi}{\partial E_{II}} F_{II}. \tag{2.40}$$

Thus, we can write

$$P_{II} = \frac{\partial \Psi}{\partial \lambda_I} - \frac{p}{\lambda_I} \quad \text{(I not summed)}. \tag{2.41}$$

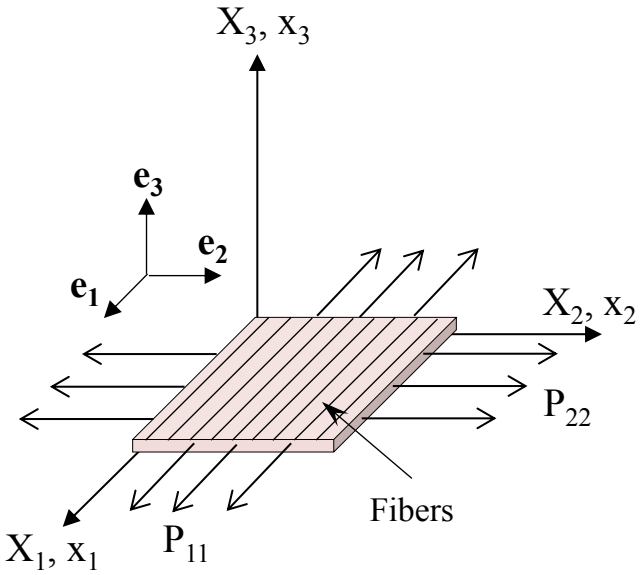

Figure 2.3. Biaxial stretching of transversely isotropic rectangular membrane.

If the material is incompressible, the Lagrange multiplier p can be determined directly from the boundary condition (P_{33}=0) according to

$$p = \lambda_3 \frac{\partial \Psi}{\partial \lambda_3}. \tag{2.42}$$

Inserting this relation into Eq. (2.41) yields

$$\begin{aligned} P_{11} &= \frac{\partial \Psi}{\partial \lambda_1} - \frac{\lambda_3}{\lambda_1}\frac{\partial \Psi}{\partial \lambda_3} \\ P_{22} &= \frac{\partial \Psi}{\partial \lambda_2} - \frac{\lambda_3}{\lambda_2}\frac{\partial \Psi}{\partial \lambda_3} \end{aligned}. \tag{2.43}$$

It should be noted that the shear terms, P_{12} and P_{21}, are negligible if the fiber orientation distribution is symmetric about the co-ordinate axis along $\mathbf{e}_1$.

2.4.2 Phenomenological Hyperelastic Constitutive Models

The most common type of constitutive models used for soft tissues are phenomenological models, which are usually of a polynomial or exponential form. A very well-known example of a phenomenological constitutive model, originally introduced by Fung [11] but used and extended by many researchers afterwards, is of the form

$$\Psi = c \cdot \exp\left[f\left(a_i, \mathbf{E}\right)\right], \tag{2.44}$$

where the function f generally consists of polynomial terms of the components of $\mathbf{E}$ of varying order (with constants a_i), depending on the specific set of mechanical data. The most general form of Eq. (2.44) is given by (in indicial notation with the summation convention) [97]

$$\Psi = \frac{1}{2}\alpha_{ijkl}E_{ij}E_{kl} + \left(\beta_0 + \beta_{mnpq}E_{mn}E_{pq}\right)\exp\left(\gamma_{ij}E_{ij} + \kappa_{ijkl}E_{ij}E_{kl} + \ldots\right). \tag{2.45}$$

Another form of phenomenological constitutive equation is expressed in terms of a set of independent strain invariants of **C** or **B** [98]. The first three (principal) invariants are defined as

$$\begin{aligned} \mathrm{I}_1 &= tr\,\mathbf{C} = tr\,\mathbf{B} = \lambda_1^2 + \lambda_2^2 + \lambda_1^2 \\ \mathrm{I}_2 &= \frac{1}{2}\left[\left(tr\mathbf{B}\right)^2 - tr\mathbf{B}^2\right] = \lambda_1^2\lambda_2^2 + \lambda_1^2\lambda_3^2 + \lambda_2^2\lambda_3^2 \\ \mathrm{I}_3 &= \det\mathbf{C} = \det\mathbf{B} = J^2 = \lambda_1^2\lambda_2^2\lambda_1^2 \end{aligned} . \tag{2.46}$$

These invariants are used to define the strain energy for isotropic materials, i.e.

$$\Psi = \Psi\left(\mathbf{C}\right) = \Psi\left(\lambda_1, \lambda_2, \lambda_3\right), \tag{2.47}$$

which results in the three principal stresses (Cauchy, 1st Piola Kirchhoff, and 2nd Piola Kirchhoff) in an incompressible material (a=1,2,3) to be defined as (see also [99])

$$\begin{aligned} \sigma_a &= J^{-1}\lambda_a \frac{\partial\Psi}{\partial\lambda_a} \\ P_a &= \frac{\partial\Psi}{\partial\lambda_a} \\ S_a &= \frac{1}{\lambda_a}\frac{\partial\Psi}{\partial\lambda_a} \end{aligned} . \tag{2.48}$$

Many different forms of strain energy functions for isotropic soft deformable materials in terms of the principal stretches have been proposed in the literature. On the other hand, many materials, and in fact, most biological tissues, are characterized as anisotropic and cannot be described by isotropic constitutive equations. These materials can be viewed as being composed of an isotropic matrix material (ground substance) and one or more families of fibers responsible for the anisotropy, with the derivation of the constitutive relation based on the principle of *material symmetry*. This approach, initially proposed by Holzapfel [86], can be viewed as a "hybrid" approach, between pure phenomenological and fully structural. The simplest representation of this is transverse isotropy, with one family of fibers. The fiber direction in the

reference configuration is defined by a unit vector **a**(**X**), and its structural tensor is defined as $\mathbf{a}\otimes\mathbf{a}$. The so-called pseudo-invariants of **C** and **a**, related to the fibers, are now introduced as

$$\begin{aligned} \mathrm{I}_4 &= \mathbf{a}^T\mathbf{C}\mathbf{a} = \lambda_A^2 \\ \mathrm{I}_5 &= \mathbf{a}^T\mathbf{C}^2\mathbf{a} \end{aligned}, \tag{2.49}$$

where λ_A is the stretch in fiber family *A*. For a transversely isotropic material, the strain energy is written in terms of the five invariants as $\Psi = \Psi\left(\mathrm{I}_1,\mathrm{I}_2,\mathrm{I}_3,\mathrm{I}_4,\mathrm{I}_5\right)$. When a material consists of two families of fibers, where the second fiber family is defined by the unit vector **b**, additional strain invariants are defined associated with this additional fiber family and the interaction between the two families. The invariants I_6-I_8 are defined as

$$\begin{aligned} \mathrm{I}_6 &= \mathbf{b}^T\mathbf{C}\mathbf{b} = \lambda_B^2 \\ \mathrm{I}_7 &= \mathbf{b}^T\mathbf{C}^2\mathbf{b} \\ \mathrm{I}_8 &= \mathbf{a}^T\mathbf{C}\mathbf{b} \end{aligned}. \tag{2.50}$$

In soft tissues, the strain energy function is often divided into an isotropic and an anisotropic part representing the isotropic matrix and the fibers, respectively, resulting in

$$\Psi = \Psi_{iso}\left(\mathrm{I}_1,\mathrm{I}_2\right) + \Psi_{aniso}\left(\mathrm{I}_4,\mathrm{I}_5,\ldots\right), \tag{2.51}$$

when assuming incompressibility ($I_3 = 1$). This is often simplified to [86]

$$\Psi = \Psi_{iso}\left(\mathrm{I}_1\right) + \Psi_{aniso}\left(\mathrm{I}_4,\mathrm{I}_6\right). \tag{2.52}$$

Different specific functional forms of Ψ_{iso} and Ψ_{aniso} have been proposed in the literature, where for Ψ_{iso} often a neo-Hookean formulation is used

$$\Psi_{iso} = \frac{\mu}{2}\left(\mathrm{I}_1 - 3\right), \tag{2.53}$$

where μ is the shear modulus. For Ψ_{aniso} many different phenomenological expressions similar to Eq. (2.45) have been proposed (*e.g. [86, 100-103]*). An interesting generalization of the

invariant based method has been presented by Ehret and Itskov [104]. They have introduced a constitutive model for fiber-reinforced materials consisting of an arbitrary number of fibers, where each fiber is represented by its individual structural tensor and a weight factor.

2.4.3 Structural Constitutive Models

The structural approach, where each model parameter has physiological significance, allows for separate investigation of the contribution of each individual tissue component to the tissue's mechanical behavior. Structural constitutive models can help determine the underlying physiological parameters of normal remodeling and growth as well as pathological processes.

The structural constitutive model developed in this dissertation builds upon the theoretical work formally introduced by Lanir [89, 90], in which the tissue-level response is related to the collective contribution of individual fiber ensembles. The term fiber ensemble refers to a collection of fibers sharing a common orientation. This modeling technique treats the fibrillar ECM component by homogenizing the fiber ensemble response. This modeling approach for planar collagenous tissues is integrated into a multi-component structural constitutive model by combining it with a description for a second component, outlined in Chapter 7.0.

2.4.3.1 Assumptions

The representative volume element (RVE) identified, that contains a fiber ensemble (Figure 2.4), is sufficiently large to include enough information on the underlying microstructure yet is amply smaller than the macroscopic tissue dimensions. The RVE is treated as a three-dimensional continuum, and within the RVE, the following assumptions are made:

1. The tissue can be idealized as a network of fibers of varying types and structures, all embedded within a compliant ground matrix.
2. Tissue dimensions and internal structure change under the affine assumption.
3. The individual constituent fibers bear load only along their fiber axes and have negligible compressive or bending rigidity.

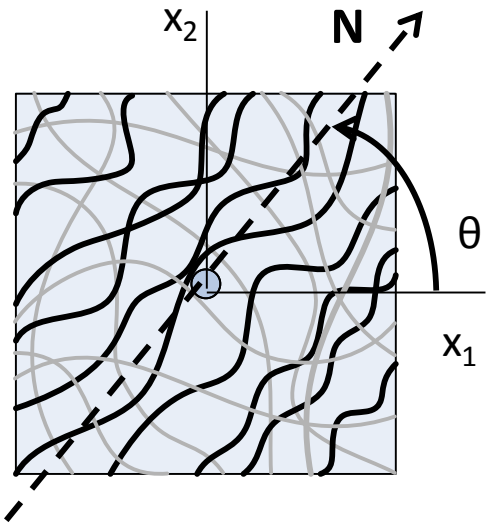

Figure 2.4. Schematic of representative structural volume element.
Fiber ensemble is an idealized group of fibers of different crimp or undulation, aligned in the same direction **N** at an angle θ.

2.4.3.2 Tissue Level Framework

The tissue level strain energy density Ψ of the RVE is assumed to result from the summation of contributions of individual fibrous components, weighted by their respective mean volume fractions ϕ is defined as

$$\Psi(\mathbf{E}) = \sum_i \phi_i \Psi(\mathbf{E}) \tag{2.54}$$

Assuming a hyperelastic material response, the tissue-level 2nd Piola Kirchhoff stress **S** is derived from the strain energy as (Eq. (2.37))

$$S(\mathbf{E}) = \frac{\partial \Psi(\mathbf{E})}{\partial \mathbf{E}} - p\mathbf{C}^{-1},$$

where the Lagrange multiplier p accounts for the incompressible nature usually associated with non-fibrillar tissue components.

A structurally based modeling approach for the collagen fibers in planar tissues have been employed, where the contribution of individual collagen fiber ensembles acting at independent orientations is summed over all orientations, using a statistical fiber orientation distribution function. Thus, it assumes the form

$$\Psi_{col}(\mathbf{E}) = \int_{\theta} R_{col}(\theta)\ \Psi_{col}^{ens}(\theta, \mathbf{E})\, d\theta = \int_{\theta} R_{col}(\theta)\ \Psi_{col}^{ens}\left(E^{ens}(\theta)\right) d\theta, \tag{2.55}$$

where $R_{col}(\theta)$ is the collagen fibers' angular density function, Ψ_{col}^{ens} is the strain energy associated with an individual collagen fiber ensemble (*ens*), and $E^{ens} = \mathbf{N}^T\mathbf{E}\mathbf{N}$ is the uniaxial Green-Lagrange strain acting in the ensemble direction, defined by a unit vector parallel to the fiber axis in the reference configuration $\mathbf{N}(\theta)$. The effective ensemble response has been modeled with a phenomenological expression [93, 105] as well as with a formulation accounting for the recruitment process [93]. The former approach is described here, and the latter approach will be presented in Chapter 7.0.

2.4.3.3 Phenomenological Fiber Ensemble Model

Exponential models have been successfully used to describe the nonlinear effective fiber ensemble stress-strain relation. A two-parameter exponential model has been defined as

$$S^{ens}\left(E^{ens}\right) = d_1\left[\exp\left(d_2 E^{ens}\right) - 1\right], \tag{2.56}$$

which has been applied to the aortic valve and arterial tissue [93, 105-108]. Using this exponential fiber model form for the fiber ensemble response, this model can be considered

hybrid: The fiber orientation distribution is defined in a structural manner and can be determined experimentally; however, the fiber ensemble model itself is phenomenological.

A modified version of this model considers that collagen fibers are being recruited up to an upper bound ensemble strain E_{ub} where all fibers are straight. The effective fiber ensemble response follows the exponential response of Eq. (2.56) up to this upper bound strain, and when the upper bound strain is reached, the fiber ensemble is assumed to behave in a linear elastic manner with a modulus equal to the tangent modulus at E_{ub}, under the assumption that straight collagen fibers behave linear elastic. This results in the following fiber ensemble model:

$$S^{ens}\left(E^{ens}\right)=\begin{cases} d_1\left[\exp\left(d_2E^{ens}\right)-1\right] & for \quad 0<E^{ens}<E_{ub} \\ \left.\dfrac{\partial S^{ens}}{\partial E^{ens}}\right|_{E^{ens}=E_{ub}}\left[E^{ens}-E_{ub}\right]+d_1\left[\exp\left(d_2E_{ub}\right)-1\right] & for \quad E^{ens}>E_{ub} \end{cases}. \tag{2.57}$$

2.4.4 Mechanical Models of Growth and Remodeling

The widely accepted biomechanical driver behind the growth and remodeling (G&R) processes, as a part of normal development or as a response to pathology, is the restoration of a homoeostatic internal stress level. The radius, wall thickness, and opening angle associated with residual stress in arteries adapt to perturbations in pressure and flow. During the last decade several mathematical models have been developed to capture and predict the G&R behavior of arteries [109-111]. The volumetric growth was explained by early models through the study of the relationship between mechanical load and uniform growth by Hsu [112], and the study of mass resorption and deposition in living bone by Cowin and Hegedus [113, 114], who introduced a theory explaining the structural adaptations of an elastic material to applied loading. The later work by Skalak [115] provided an analytical description of the non-uniform mass growth, and

Rodriguez et al. [116] combined these theories of the finite volumetric growth in soft tissue within the continuum framework by introducing the multiplicative decomposition of the total deformation gradient into its elastic and growth parts (Figure 2.5). In this approach, the growth kinetics resulting in total shape change is divided into two parts: (i) a generally non-compatible part resulting from the material addition or removal that alters the local stress-free configuration, and (ii) an elastic part associated with the deformation of constituent elements to form the final shape [117].

Mixture theories [118, 119], which combine continuum theories for the motion and deformation of solids and fluids, with general principles of chemistry, have been utilized to model the individual growth and mechanical response of primary individual wall constituents, mainly proteoglycan gel matrix, smooth muscle cells, elastin and collagen; homogenization is done through a rule-of-mixtures model for the stress response. Humphrey and coworkers [120-122] have developed an extensive modeling framework for tissue growth and remodeling of vascular wall based on the so-called constrained mixture approach, where the tissue is assumed to be a mixture of multiple (solid) constituents, that are constrained to deform together.

The rule-of-mixtures relations allow the changing rates of protein synthesis and cell proliferation and associated half-lives to be accounted for and enable basic mechanisms of G&R to be modeled mathematically rather than merely modeling the consequences of such turnover. Changes in geometry are computed naturally in the constrained mixture model of G&R simply by satisfying linear momentum balance at each G&R time point. Nevertheless, the current functional forms are in a state of infancy, and appropriate constitutive relations need to be derived based on experimental data.

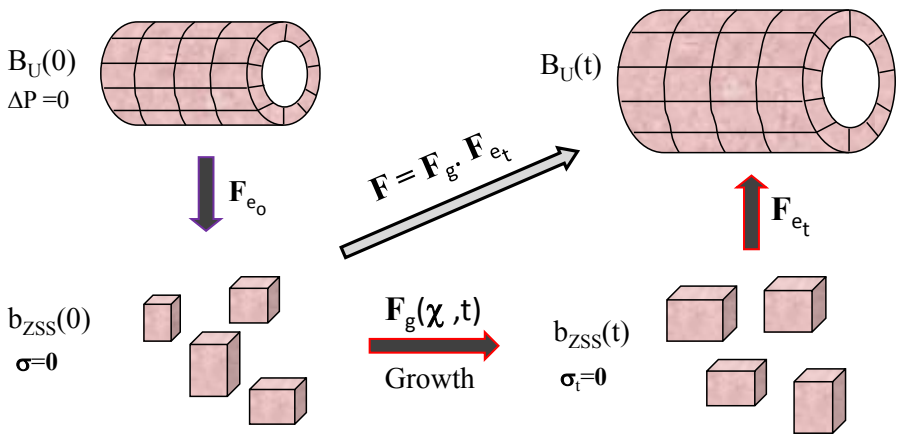

Figure 2.5. Schematics of multiplicative decomposition of deformation gradient in remodeling and growth. The deformation gradient is decomposed into its elastic, $\mathbf{F}_e$, and growth, $\mathbf{F}_g$, parts. B_U represent unloaded intact configurations, and b_{ZSS} are stress-free configurations.

3.0 ESTIMATION OF IN VIVO SURFACE GROWTH DEFORMATIONS OF MAIN PULMONARY ARTERY AND ASCENDING AORTA

The following studies were conducted to characterize the PT and AA geometry and delineate deformation patterns in the growing ovine model as outlined in the first specific aim (section 1.7). MR images were obtained from endoluminal surfaces of 13 ovine hearts at end-diastole with ages ranging from 1.5 to 12-months (considered adult), with corresponding masses of 15.3 to 56.6 kg. The basic geometric parameters of the PT and AA (including sinus regions) were first measured, based on segmentation point cloud data. This initial study was carried out to define the tissue engineered pulmonary artery conduit *in vivo* dimensional requirements, and also to determine the degree of nonaffine alteration in the surface geometry of both arteries during postnatal growth. Based on the results obtained, it was decided to quantify the regional surface growth deformation patterns of the PA and AA to understand the underlying causes of revealed nonaffine changes in surface geometry of each artery. A finite element based surface representation of each artery was developed, and the interpolated geometries as a function of mass were obtained to determine local arterial surface growth relative to each artery's early age state of 15 kg. The principles of nonlinear deformation analysis were used to quantify the local alterations in the *in vivo* surface geometry.

Although in the biomechanical analysis of growth, the reference configuration is usually the stress-free state, in this study, the reference state is the in-vivo end-diastolic stage of the

artery, where artery is both loaded and contains residual stress. Therefore, the computed postnatal surface growth deformations include the alterations in the residual stress and the end-diastolic deformation. However, the assumption was made that the changes in surface geometry of the artery significantly dominate the postnatal growth deformation patterns as compared to the modifications in residual stress and end-diastolic deformation profile or mechanical behavior.

Results indicated that the spatial and temporal growth deformation patterns of both arteries were highly heterogeneous. The longitudinal PA growth stretch of the middle region on the posterior wall reached 2.57±0.078 (mean±SD) at the adult stage. In contrast, the longitudinal growth of the AA was smaller and fairly uniform (1.80±0.047). Interestingly, a region of the medial wall of both arteries where they are in contact showed smaller circumferential growth stretches, specifically 1.12±0.012 in the PA and 1.43±0.071 in the AA at the adult stage. Overall, our results suggested that the surrounding tissue impingements and contact between the arteries resulted in increasing spatial heterogeneity in postnatal growth, leading to increasing taper and in particular an increase in cross-sectional ellipticity of the PA. Results of this study can be used to guide the development of therapeutic approaches for congenital defects.

3.1 METHODS

3.1.1 Animal Source

Thirteen sheep (Ovis aries, subspecies Dorset) weighing between 12 to 60 kg, of ages 1.5 (the earliest time point used for ovine heart valve implants [30]) to 12 months (full adulthood), were obtained. Use of experimental sheep was approved by the Institutional Animal Care and Use

Committee of Children's Hospital Boston. Animals were cared for by a veterinarian in accordance with the "Guide for the Care and Use of Laboratory Animals." Since it was shown that the mass of the animals highly correlated with their age and was known more exactly, mass was used to identify the growth stage throughout the study.

3.1.2 MRI

Imaging was performed with a 1.5 Tesla MRI scanner (Philips Achieva, Best, the Netherlands) and a 5-channel cardiac radiofrequency surface coil. After localizing images were obtained, breath-hold ECG-gated steady-state free precession sequences were obtained in long and short-axis ventricular planes, and in the long and short-axis planes to the pulmonary valve. In-plane and through-plane velocities were measured using an ECG-gated velocity-encoded cine MRI pulse sequence. Imaging of the thorax was performed using a ECG and respiratory navigator 3D SSFP pulse sequence to generate a three-dimensional isotropic data set (acquired resolution of 1.5 x 1.5 x 1.5 mm sections, reconstructed to 0.78 x 0.78 x 0.78 mm) at end-expiration and end-diastole (Figure 3.1A).

3.1.3 Image Segmentation

A semi-automated segmentation method, termed Shells and Spheres, was used for extracting anatomical shapes from 3D images. This method is specifically designed to segment shapes that curve back upon themselves, such as the heart and great vessels [123]. Spherical operators were centered at each image pixel and sized to reach, but not cross, the nearest object boundary. Spheres were then "grown" at each pixel location by incorporating "shells" of pixel intensity

values into an ongoing analysis of mean, variance, and first-order moment, in order to identify the radius at which each sphere would grow past its nearest object boundary. The coronary arteries and first AA side branch were removed and the remaining gaps were filled during the segmentation. For each image, a subset of spheres was identified as medial, meaning that each touched at least two boundaries. Therefore the algorithm produced a set of paired boundary and medial locations in addition to the segmented shape of the PT and AA. The local medial locations or center points helped define the centerline paths used in registering the arteries as well as develop an appropriate curvilinear coordinate system to carry out the deformation analysis.

A set of Shells and Spheres segmentations of the PT were also manually segmented. The Shells and Spheres segmentation results correlated well with the given set of manually segmented images and produced visually accurate representations of the heart and great vessels (Figure 3.1). The Dice Similarity Coefficient was calculated to be 0.97, indicating a strong similarity between manual and Shells and Spheres segmentations [124].

3.1.4 Definition of Anatomic Terms

The proximal extent of the PT was defined at the pulmonary root and its distal extent at the PA bifurcation (Figure 3.1B,C). The sinuses of Valsalva were defined as the bulbous portion of the proximal PT. The STJ was defined as the distal boundary of the sinuses of Valsalva. The proximal boundary of the PA was defined at the STJ and its distal aspect, at the PA bifurcation. The region of interest (ROI) on the AA was defined as beginning at the aortic STJ and ending at a plane that intersected the bifurcation point of the pulmonary trunk, termed end-ROI.

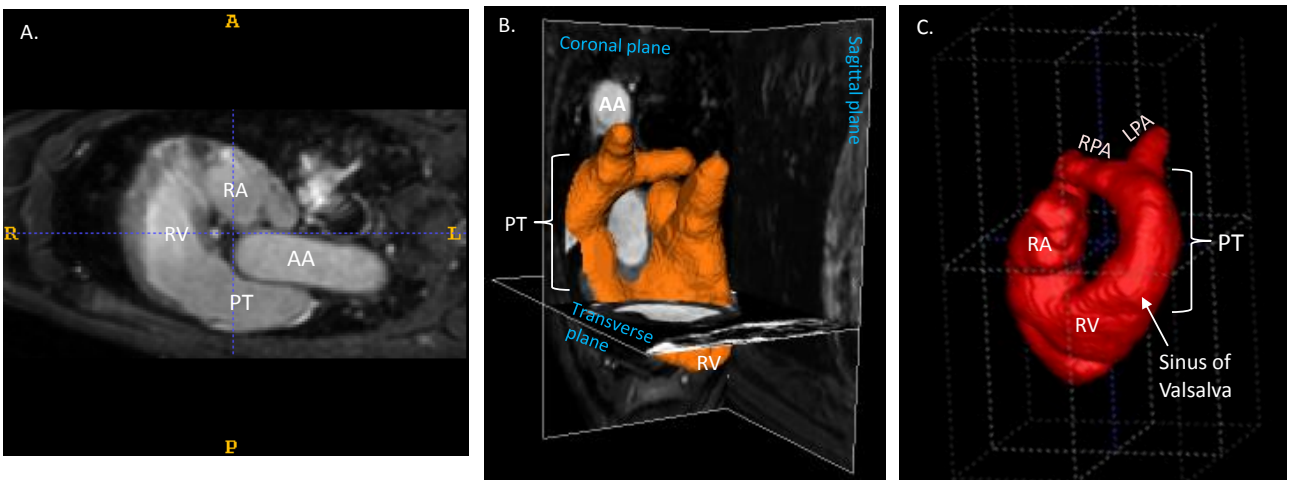

Figure 3.1. 2D slice and 3D raw MR cardiac images and segmentation masks. 2D slice (A), 3D MRI of the Ovine heart and two major arteries overlaid with a Shells and Spheres segmentation of the pulmonary trunk and right ventricle in the posterior view (orange) (B), and anterior view of 3D surface model of the automated Shells and Spheres segmentation of the right heart shown (red) with following structures labeled (C): Right atrium (RA), Right ventricle (RV), Pulmonary trunk (PT), Right pulmonary artery (RPA) and Left pulmonary artery (LPA). Copyright © 2007, IEEE [124].

3.1.5 Basic Dimensional Measurements

Centroids of medial point clouds were calculated at a mean of 6-mm intervals along the height of the artery. To define a center axis, every three adjacent centroids were fitted with a second order polynomial. Sections of surface point clouds, with an average thickness of 2.5mm, were obtained normal to the center axis at midpoint between neighboring centroids (Figure 3.2). The proximal and distal anatomic boundaries of the PA were defined manually, by the identification of the sinuses of Valsalva (pulmonary root, proximal boundary) and the pulmonary bifurcation (distal boundary). The length of the artery along the center axis path was calculated based on the cumulative lengths of the polynomial segments within these defined boundaries. Vessel tortuosity was calculated as the ratio of distance along the center axis path to end-to-end length, with a value of 1.0 corresponding to no tortuosity (i.e. straight tube).

The boundary data were fitted with ellipses (Figure 3.2), and volume and surface area of each artery were calculated. For the pulmonary root and sinuses of Valsalva, the segmented section having the largest sinus radius was selected manually for analysis from each data set (Figure 3.3A). Nodes were manually selected from that cross-section. The center of the section was determined based upon the center of the best-fit circle to the three sinus nodes. From these definitions of nodes and center, the sizes, angles and areas of the sinuses of Valsalva were measured (Figure 3.3B).

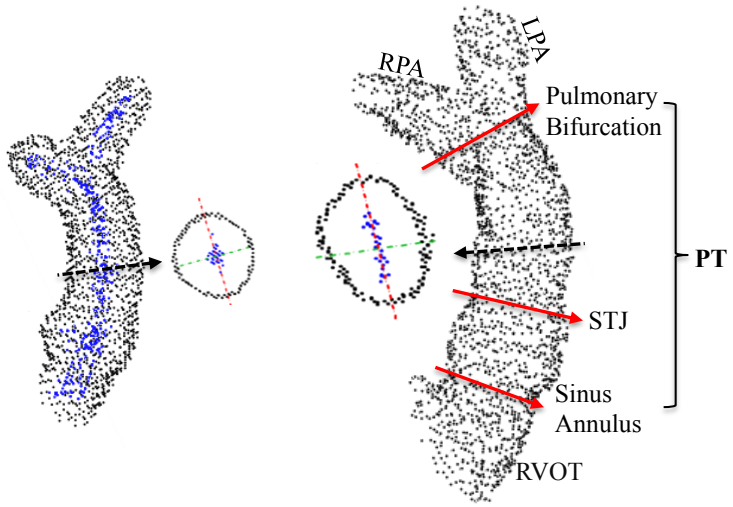

Figure 3.2. Point cloud depictions of PT as generated by shells and spheres segmentation technique. Representative juvenile and adult PT surface points (black) with medial point clouds (in blue) shown in the former, and corresponding single anatomical cross-sectional shapes of surface and medial points clouds along with principal axes in both PTs demonstrated.

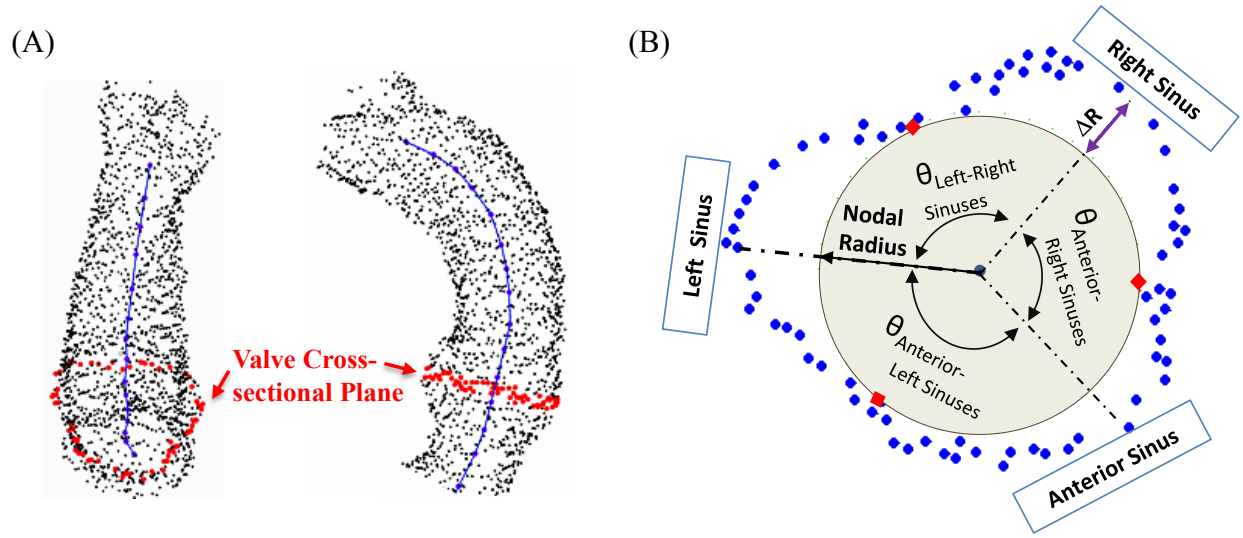

Figure 3.3. Basic dimensional measurements of sinuses of Valsalva shown in PA. Plane of maximum sinus radii (red) shown along with center axis (blue), and calculated centroids (purple) in posterior (left) and sagittal views (right) (A). Illustration of measurements of sinuses of Valsalva in a cross-section of surface point clouds across region of maximum sinus size (blue) and best-fit circle to sinus nodes (valve commissures; red rectangles) along with angles between sinuses (B).

3.1.6 Overall Approach for Estimation of Surface Growth Deformation

Since it was not possible to place physical markers on the tissue surface, we assumed that the relative circumferential and longitudinal locations of material points were locally preserved throughout the postnatal maturation period. The 3D coordinates of arterial surfaces points were interpolated in the in-surface coordinate space using the piece-wise polynomial finite-element shape functions. Subsequently the surface geometries were interpolated as a function of mass. Finally, the full growth deformation maps were obtained by applying the 2D nonlinear membrane shell-based convective surface analysis to the interpolated surface coordinates to estimate the effective growth strain field. Specific steps are given in the following.

3.1.7 Registration

While semi-automated non-rigid 3D registration methods that can deform one image to match the template image by defining a spatial transformation exist [125], the more inherent variations in anatomical shapes and image quality, the less applicable these approaches become. The AA and PA datasets were, therefore, registered semi-manually through the following global affine transformation sequence. The affine registration of the PA was defined from three significant features: 1) the left, 2) right pulmonary arteries at the BFN (Figure 3.4B), and 3) the centerline path. The AA registration was based on the main side branch and the two coronary arteries at the sinuses of Valsalva, which formed three prominent anatomical landmarks.

The AA and PA of the youngest sheep (1.5 month-old, 15.3 kg) were chosen as the templates to define registration. Each segmentation image was aligned to the corresponding template using a two-step registration procedure. Automated intensity-based registration was first used to align the images, and then the images were manually transformed to improve alignment of the aforementioned features. The automated registration was performed within a standard registration framework consisting of a cost function, optimizer, transform, and interpolator. In this framework, a cost function was computed between the two images to measure similarity, an optimizer iteratively adjusted the parameters of a transform to improve the cost function, and the interpolator applied image transforms to calculate sub-voxel values. In this study, a gradient descent optimizer with a correlation ratio cost function was used to determine the affine transformation variables of 3D rotation and scaling with the nearest neighbor interpolation, appropriate for binary data, used to apply the transform.

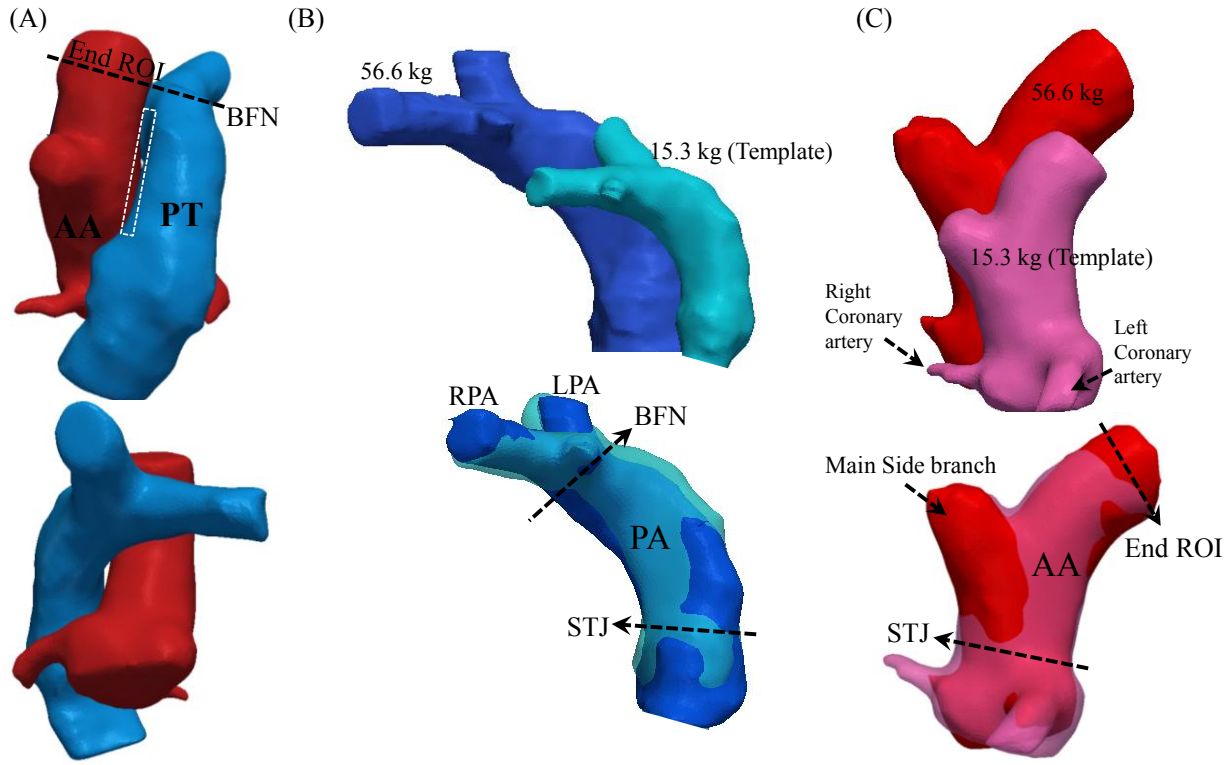

Figure 3.4. Anatomical positions and registration of AA and PT.
Anatomical positions shown in anterior view, with medial aspect outlined (Dashed square; Top), and in posterior view (Bottom) (A). Registration by affine transformation: (B) and (C) show, respectively, non-registered images of PA and AA (Top), and images of PA and AA of 56.6-kg ovine registered to their corresponding templates of 15.3-kg lamb (Bottom) (registration RMS errors for images of same juvenile ovine obtained one week apart were 0.78 mm in PA and 0.62 mm in AA). *Note:* Main side branch coming off of AA in ovine branches off to Brachiocephalic, Left Common Carotid and Left Subclavian arteries at a more distal point.

The AA registration was manually refined by aligning the segments of coronary arteries proximal to the sinuses of Valsalva and the main side branch with those of the template (Figure 3.4C). To develop the PA centerline paths, the surface and local center points were aligned with the X^3 axis (Figure 3.5A), and the cylindrical polar coordinates of local center points were computed. The centerline path of each PA was defined using 4^{th} and 2^{nd} order polynomials to interpolate the radial and angle coordinates of local center points as a function of the X_3 coordinate, respectively. The 3D curvilinear feature of the centerline paths allowed refining PAs' registration and defining optimal scaling factors μ. The AA and PA registered surface renderings

were displayed together and each surface data set was re-cropped according to the aforementioned boundary definitions.

3.1.8 Surface Fitting

3.1.8.1 Surface parameterization

A toroidal coordinate system was defined to allow use of the linear least-squares fitting method for developing surface models of the PA and AA, where only a single coordinate was fitted [126], and resulted in a relatively uniform distribution of data points in the in-surface coordinate plane [127]. The local coordinate of each surface point was determined by finding its orthogonal projection on the centerline path using the gradient-based unconstrained optimization routine of backtracking line search, implemented in Mathcad (Parametric Technology Corporation. MA, USA).

3.1.8.2 Common centerline path generation

In order to define all the corresponding surfaces with respect to one coordinate system, a common centerline path was developed. The common centerline path of all PA surfaces was simply developed by interpolating the radial and angle coordinates of individual centerline paths as a function of X^3 coordinate using 2nd and 4th order polynomial functions, respectively, which accurately approximated both coordinates (Figure 3.5A).

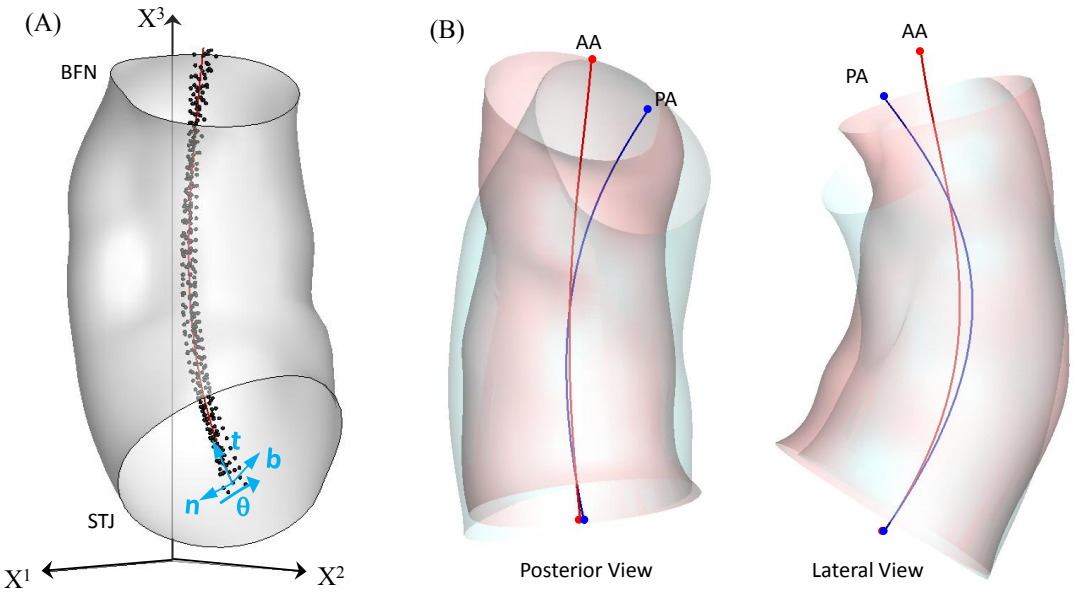

Figure 3.5. Common center axis of PAs and comparison of AA and PA center axes curvatures. Common center axis of PAs (red) and individual center axes points (black) with Frenet frame (blue) shown in medial-posterior view along with global Cartesian coordinate system (A). AA and PA center axis paths shown together from two perspectives to demonstrate larger tortuosity of PA compared to AA (B).

3.1.8.3 Coordinate transformation and surface fit

Once the parameterization of surface points was complete, the following local Cartesian coordinate was defined at each of the projection points on the centerline path based on the Frenet frame [128]. This coordinate transformation is represented by

$$\mathbf{r}(\theta, X^3) = \mathbf{x}(\theta, X^3) = \mathbf{Q}(s) \cdot \mathbf{x}'(\theta, s) + \mathbf{y}(X^3), \tag{2.1}$$

where s is the length along center axis path, $\mathbf{x}'$ is the local coordinate of the surface point in the current configuration, with its projected centerline path point $\mathbf{y}$, and $\mathbf{Q}$ is the local 3D rotation matrix (Appendix A1)**.** Next, local growth as a deformation was evaluated using a convective coordinate system, under the assumption that deformations occur such that the (θ,s) surface coordinate locations for any material point undergo minimal changes during maturation. A finite

element based surface fit was developed to model the arterial surface geometry using 2D finite element interpolation functions derived from the tensor product of 1D cubic hermite element formulation to enforce C^1 continuity [126]. The bicubic Hermite finite element has four functions defined at each node: the radial coordinate and its partial first and cross derivatives with respect to local isoparametric coordinates ξ and η (which correspond to the **θ** and **t** directions, Figure 3.5A). Thus, the radial coordinate of an internal surface point *P* is computed by summing the product of 16 terms

$$\rho_P = \psi_i^{jk}(\xi,\eta)\rho_i^{jk}, \tag{2.2}$$

where ρ_i^{jk} is the vector of nodal variables, subscript i=1,4 denotes the node number, and subscripts j,k=0,1 denote the order of derivatives with respect to ξ and η respectively.

3.1.8.4 Finite Element Mesh Size

The very high density of data points from MR images greatly exceeded the minimum requirement of 16 data points per element (with 16 nodal variables). However, the accurate reconstruction of the 3D surface in the toroidal coordinate system through the finite element interpolation scheme required determination of the appropriate mesh resolution for capturing the prominent features while smoothing the noise due to MRI and segmentation processes. To this end we developed the following approach to determine the optimal number of elements required to accurately represent the endoluminal surface geometries. The mesh resolution was determined based on the oldest PA geometry due to its more complex 3D shape compared to the AA. The in-plane dimensions of the smallest feature of interest amongst all PA surfaces was resolved to be 6 x 7 mm, in **t** and **θ** directions, respectively. A finite element surface fit with relatively dense grid size of 8 by 8 elements, that captured the features having twice as high of the spatial frequency

as that of the smallest feature of interest, was initially generated. The surface fit was sampled at a quarter size of the smallest targeted feature in **θ** and **t** directions. A 2D FFT analysis was performed on the surface fit data using MATLAB (The MathWorks Inc. MA, USA). The numbers of elements in θ and t directions were reduced iteratively until the 2D FFT spectrum of the surface fit indicated significant smoothing of the determined spatial noise.

3.1.9 Two-Dimensional Surface Deformation

The local growth deformation of the 2D endoluminal surfaces (with no transmural deformation consideration) was estimated in the polar toroidal coordinate. The in-surface base vectors were computed using Eqs. (2.3) and (2.4) according to

$$\mathbf{G}_I = \frac{\partial \mathbf{R}}{\partial \Theta^I}, \qquad \mathbf{g}_I = \frac{\partial \mathbf{r}}{\partial \Theta^I}$$

where I=1,2 and $(\Theta^1,\Theta^2) = (\theta,s)$. The corresponding normal unit vectors are then simply derived from the in- surface vectors as follows

$$\mathbf{G}_3 = \frac{\mathbf{G}_1 \times \mathbf{G}_2}{|\mathbf{G}_1 \times \mathbf{G}_2|}, \qquad \mathbf{g}_3 = \frac{\mathbf{g}_1 \times \mathbf{g}_2}{|\mathbf{g}_1 \times \mathbf{g}_2|}. \tag{3.1}$$

The measure of shear during growth was defined as

$$\gamma = \cos^{-1}\left(\hat{\mathbf{u}}_\theta \cdot \hat{\mathbf{u}}_s\right) - \cos^{-1}\left(\hat{\mathbf{U}}_\theta \cdot \hat{\mathbf{U}}_s\right), \tag{3.2}$$

where $\hat{\mathbf{u}}_\theta = \frac{\mathbf{g}_\theta}{|\mathbf{g}_\theta|}$, $\hat{\mathbf{u}}_s = \frac{\mathbf{g}_s}{|\mathbf{g}_s|}$; $\hat{\mathbf{U}}_\theta$ and $\hat{\mathbf{U}}_s$ are the corresponding unit base vectors in the reference configuration The stretch ratios λ_θ and λ_s corresponding to $\hat{\mathbf{u}}_\theta$ and $\hat{\mathbf{u}}_s$ directions, respectively, were computed based on Eq.$(2.16)_2$. The subsequent growth rates (in units of Kg^{-1}) in the circumferential and longitudinal directions were obtained by computing the instantaneous slope

of the growth stretch ratio curves as a function of mass, $\dot{\lambda}_\theta$ and $\dot{\lambda}_s$, at each unit mass interval from 12 kg to 60 kg.

3.1.10 Time Interpolated Growth

To gain better insight into major trends in the temporal development and spatiotemporal relationships, a continuous growth deformation map was generated as follows. The 3D surface shapes were approximated as a function of mass by interpolating the four surface fit variables, ρ_i^o and $\rho_i^{jk>0}$, at each node. The radial coordinates were linearly interpolated, and the remaining nodal variables were approximated based on second order polynomial functions, which represented the general trend in data as accurately as possible without capturing the outlier points. The scaling factors, obtained from registration, were interpolated linearly as a function of mass. The interpolated shape of each artery at 15 kg was used as the referential geometry to obtain the spatiotemporal developmental deformation map up to 60 kg using the equations provided in the previous section. This approach also had the advantage of developing an interpolated referential configuration that avoided issues with individual specimen variations.

3.1.11 Study of Arterial Cross-Sections based on Interpolated Surface Fits

The true anatomical sections of the interpolated PA and AA surface fits with respect to their corresponding common center axes were obtained. The principal component analysis was performed on all the surface cross-sections and major and minor diameters were obtained (Figure 3.2). The angle of the major axes of sections along each artery with respect to its corresponding STJ cross-section was measured. Ellipticity of each section was calculated as the ratio of major

to minor diameters, and tracked along the length of the vessel. The arterial taper was defined as the ratio of BFN or end-ROI to STJ cross-sectional areas.

3.1.12 Verification

To assess the accuracy of the method implementation for the above deformation analysis, an analytically defined torus shaped phantom was generated [129], based on the measured geometric characteristics of the PA as follows. It was demonstrated that in the postnatal growth period the PA taper towards the BFN increased by about 20% and its cross-sectional ellipticity increased by about 30%. Its tortuosity, however, was maintained at an average value of 1.1, with negligible out-of-plane curvature. Two phantoms with the same tortuosity as the PA were created to represent the above geometric trends from the juvenile to adult stage. The analytical equation of a torus was modified to incorporate the ellipticity and taper changes (Appendix A2). To simulate growth, the phantom representing the juvenile stage was scaled by a factor of 2.33 to obtain the phantom representing the mature artery (Figure 3.15A).

3.1.13 Statistical Analysis

Student t-tests were performed for comparisons of mean values for the results of basic geometric study, where $p<0.05$ was considered significant (SPSS software, IBM Inc., New York, U.S.). Net results are presented as mean ± standard deviation (SD).

3.2 RESULTS

3.2.1 Basic Geometric Parameters

MRI data were utilized for the 11 sheep, whose mean weight was 30.9 kg (12-57 kg range) and mean age was 6 months (1-12 months range). Animal age and weight were highly correlated (r^2=0.86), and were functionally interchangeable. Due to its accessibility, weight was selected as the basis for further analysis. The linear interpolation of all growth data with respect to animal weight, explained in the following sections, resulted in $r^2 > 0.8$.

The postnatal increase in volume of sinuses of Valsalva in both aortic and pulmonary roots proportionately by an average of 184 and 171 mm^3, respectively, for every unit (kg) rise in weight (Figure 3.6A). The lengths of both sinus regions also linearly rose over time at rates of 0.22 and 0.26 mm/kg (Figure 3.6B). The angles of the sinuses with respect to the center of the vessel did not differ between age groups (p=NS) in either pulmonary (anterior-to-left angle = 117±4°; anterior-to-right angle = 112±4°; left-to-right angle = 131±4°, or aortic sinuses (left-to-right coronary angle=115±1°; right-to-noncoronary angle=124±2°; left-to-noncoronary angle=117±4°). A comparison of the size of each sinus of Valsalva was performed based on the maximum cross-sectional area of each sinus. The cross-sectional areas of aortic and pulmonary sinuses were very similar and increased significantly with age proportionate to the weight (Figure 3.7A). There were no statistically significant differences between growth rates of individual pulmonary root sinuses (right, anterior and left); however, there was a difference in sinus cross-sectional area, with the right ("non-facing") semilunar cusp area representing a larger portion of the total cross-sectional area than the left or anterior cusp (right vs. anterior p<0.008; right vs. left p<0.05, data not shown). The aortic sinuses (right coronary, left coronary and

noncoronary) were not significantly different in size and growth rate. The ratio of cumulative cross-sectional areas of sinus lobes with respect to center circle was calculated. The average contribution of aortic sinus lobes was twice as much as that of pulmonary sinus lobes to their corresponding total sinus cross-sectional areas (Figure 3.7B).

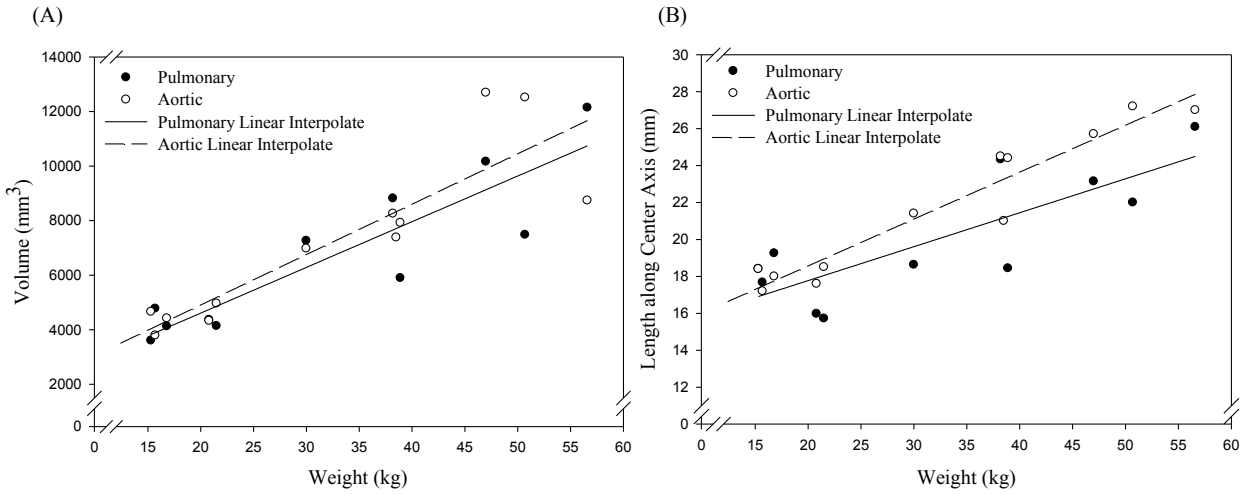

Figure 3.6. Postnatal increase in volume and length of aortic and pulmonary sinuses of Valsalva. Sinus of Valsalva increase in volume at rates of 171 mm^3/kg in pulmonary and 184 mm^3/kg in aortic roots (A) and increase in length at 0.22 mm/kg in pulmonary and 0.26 mm/kg in aortic roots (B) were linearly proportional to animal weight.

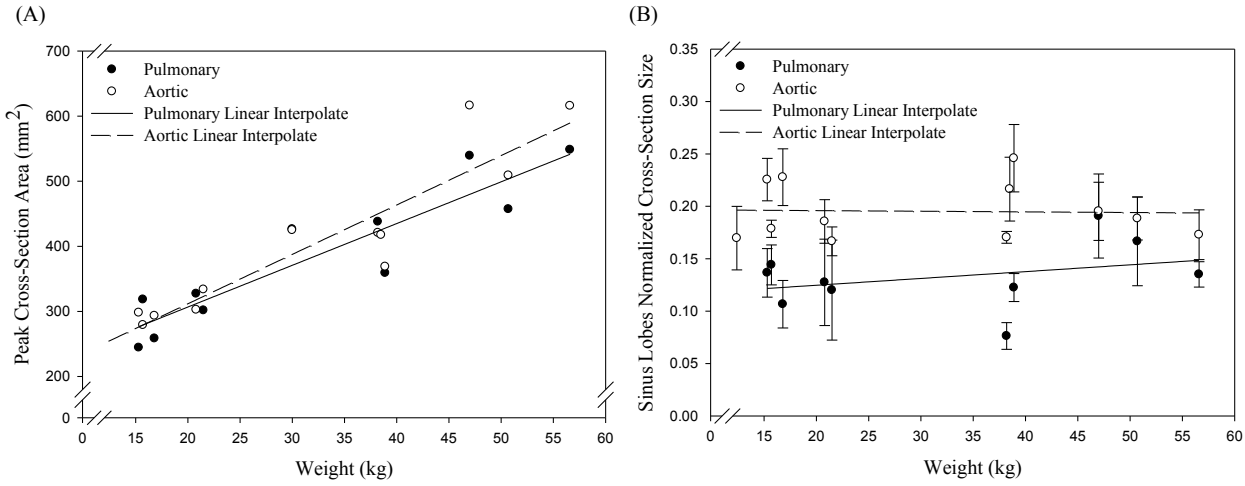

Figure 3.7. Postnatal changes in total sinus cross-sectional area and relative area of sinus lobes. Cumulative peak cross-sectional area of the sinuses of Valsalva linearly increased with weight (A). Ratio of cumulative cross-sectional areas of sinus lobes with respect to center circle was twice as large in pulmonary root as compared to aortic root (B).

Tortuosity of the PT was moderate and did not vary by animal size (1.110±0.005, p<0.7 between groups). Therefore, for the pulmonary trunk taken as a whole, additions to surface area over time did not translate into an increasingly tortuous arterial course, but into scaled arterial size increased over time. The relative contribution of the sinuses of Valsalva to the PT length along center axis path became less over time. In young animals, the sinuses of Valsalva represented approximately 38±2.2% of the entire PT length, while in larger animals, the sinuses accounted for 33±0.01% of PT length; this measurement was proven to be significant based on the considerably faster longitudinal growth rate of the PA compared to its sinus region (p<0.04). The longitudinal growth rate was very close between the PT and AA (p=NS) with every 1 kg increase in animal weight resulting in a corresponding increase in length along center axis path of 0.5 mm and 0.2 mm in the PA and pulmonary root respectively, and 0.4 mm and 0.3 mm increase in lengths of the AA and aortic root, respectively (Figure 3.6B and Figure 3.8A).

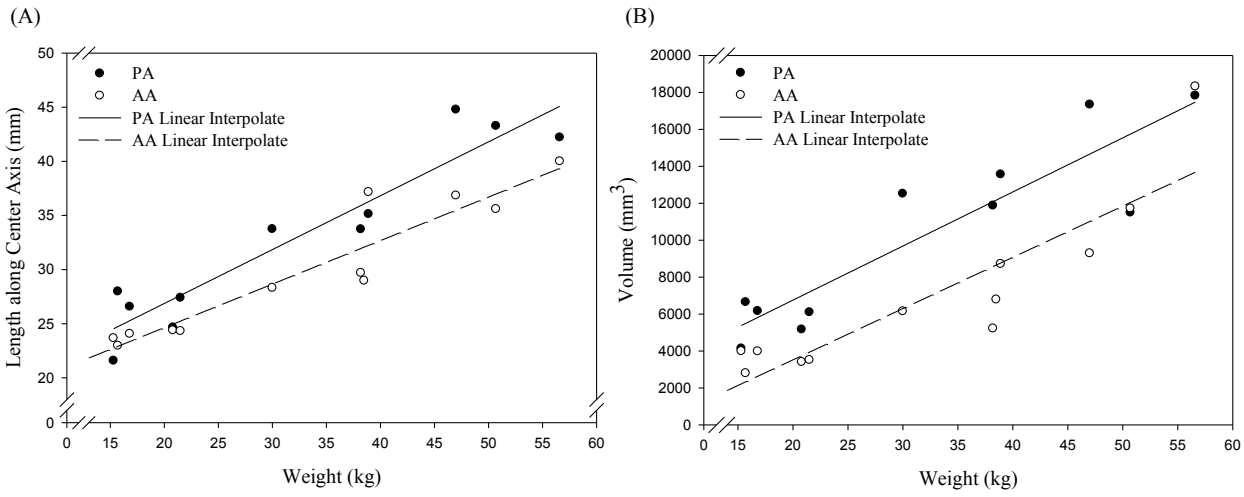

Figure 3.8. Postnatal increase in volume and anatomical length of PA and AA.
Volumes of both arteries increased linearly with weight at 343 and 256 mm3/kg, respectively (A). PA's considerably faster increase in its true length, at 0.5 mm/kg, compared to sinus region (at 0.2 mm/kg) explains its increasing contribution to PT length over time, whereas longitudinal growth of AA, at 0.4 mm/kg, did not significantly dominate that of its sinus region (0.3 mm/kg) (B).

Bulk size of both arteries, measured by surface area and volume, linearly scaled with growth; every unit kg increase in body weight yielded a corresponding increase of 44.5 mm^2 and 293 mm^3 in the PA, and 38.0 mm^2 and 278 mm^3 increases in the AA surface areas and volumes, respectively (Figure 3.8B).

The orientation of major axes of cross-sections along each artery relative to that of the STJ section was fairly constant in the PA and did not considerably change in the AA (Figure 3.9A). The cross-sectional shape of the PA, expressed as vessel ellipticity, differed between groups. In the smaller, younger animals, the PA cross-sectional shape was nearly circular throughout its length. In the larger, older animal group, the PA was relatively circular in cross-section at the level of the sinuses, but became more elliptical, with maximum ellipticity detected around approximately 70% of the total PA center axis length from the STJ. In the distal PA (70-100% of total center axis length), the arterial shape became less elliptical. Unlike the PA, the AA cross-sections showed relatively irregular and non-elliptical geometry with ellipticity staying relatively constant with age (Figure 3.9C, D; major-to-minor diameter ratios were 1.13±0.049 in the PA and 1.35±0.058 in the AA at the 60-kg growth stage).

Both the PA and AA showed significant distal tapering with age, demonstrated by a decrease in the ratio of the STJ to PA bifurcation cross-sectional areas. The PA taper increased from 0.86 (i.e. nearly straight) to 0.67 (for the adult) while the AA tapered at a slower rate from 0.74 to 0.62 (Figure 3.9B).

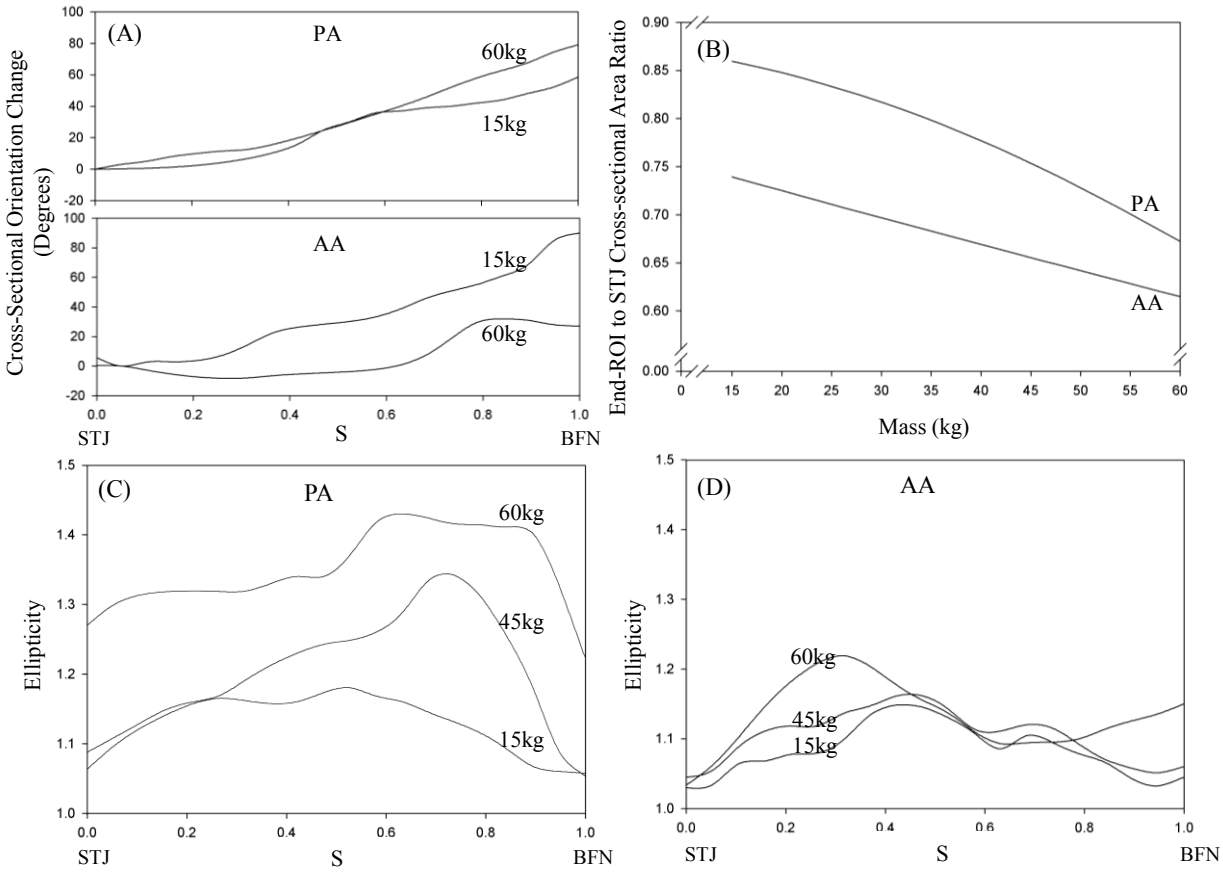

Figure 3.9. Resulting overall changes in geometry of PA and AA.
Orientation of major axes of cross-sections along PA remained unaltered and only slightly changed in AA (A). Tapering, as measured by the ratio of cross-sectional areas of BFN or end-ROI to STJs, increased with growth slightly faster in PA than AA (B). Cross-sectional ellipticity of PA increased with age (C) while it was relatively maintained in AA (D) as demonstrated by measurements at three growth stages.

3.2.2 Regional Growth Deformation Patterns

3.2.2.1 Method verification

The stretches in both circumferential and longitudinal directions computed based on the modified torus analytical equations were close in magnitude to those obtained from the finite element based implementation with root mean square (RMS) errors of 0.011 and 0.0032, respectively (Figure 3.15). The error in the shear calculation was somewhat larger since it combined errors in

both base vector calculations, but was still well within acceptable limits (RMS error=0.063 degs). Overall, the surface fit methodology was able to capture the virtual arterial surface accurately.

3.2.2.2 Affine registration

The scaled gross shapes of the PAs and AAs of the older animals closely matched with that of the 15.3-kg template, which confirmed the findings from the previous study that the arterial tortuosity remained relatively constant (Figure 3.4B,C). The registration of images from preliminary MR scans of the same juvenile ovine obtained one week apart verified the accuracy of the registration approach with RMS errors of 0.78 mm in the PA and 0.62 mm in the AA. The animals' mass and scaling factor values correlated linearly (r^2=0.85 for PA and r^2=0.91 for AA), with every 10 kg increase in mass resulting in an increase of 0.2 in scale (unitless) in both the PA and AA size. The 4th and 2nd order polynomial regressions of radial and angle coordinates very accurately approximated the coordinates of combined PAs centerline paths, further validating the accuracy of the registration method (RMS error = 0.46 mm and 3.90 degs of radial and angle fits, respectively). The resulting AA common centerline path provided an accurate representation of the combined local center coordinates with angle coordinates of local center points staying relatively constant along the X^3 coordinate (RMS error = 2.43 mm and 2.46 degs for radial and angle fits, respectively). The PA and AA segments of the centerline paths were calculated to be 24.0 mm and 27.1 mm long, respectively.

3.2.2.3 Geometry

The results from the 2D FFT analysis on different mesh densities indicated that the optimal number of equally spaced elements in θ and s was a grid of 4 x 3, respectively. For the sake of

computational efficiency the data density was reduced by 50% to less than 80 points per element. The 12-bicubic hermite element mesh provided an excellent representation of the endoluminal surface geometries (PA RMS error = 0.60±0.10 mm, AA RMS error = 0.50±0.04 mm).

The interpolated arterial shapes with respect to animal mass provided a faithful representation of spatiotemporal geometric changes in both the PA (RMS error = 0.80±0.033 mm for radial coordinates, RMS error = 0.28±0.11 and 1.61±0.22 $mm.mm^{-1}$ for first derivatives in **θ** and **t** directions, respectively, and RMS error = 1.70±0.88 mm^{-1} for cross partial derivatives) and the AA (RMS error = 0.64±0.034 mm for radial coordinates, RMS error = 0.33±0.11 and 2.23±0.26 for first derivatives in of **θ** and **t** directions, respectively; and RMS error = 2.20±1.25 mm^{-1} for cross partial derivatives).

3.2.2.4 Growth deformation patterns

The change in growth directions as measured by shear was very small in the both PA (γ = 1.17±3.50 degs) and AA (γ = –0.37±1.40 degs). Shear deformations during growth were, therefore, ignored due to overall negligible values, consequently the principal directions of growth deformation coincided closely with the circumferential and longitudinal directions.

The temporal growth patterns were relatively consistent during the developmental period with the spatial heterogeneity becoming progressively more substantial with age. The circumferential growth particularly showed larger degree of spatial variation than longitudinal growth, where it was dependent on both the circumferential and longitudinal locations (Figure 3.10 and Figure 3.13). The λ_θ values of adult stage of 60 kg are reported in the following explanation of growth deformation patterns.

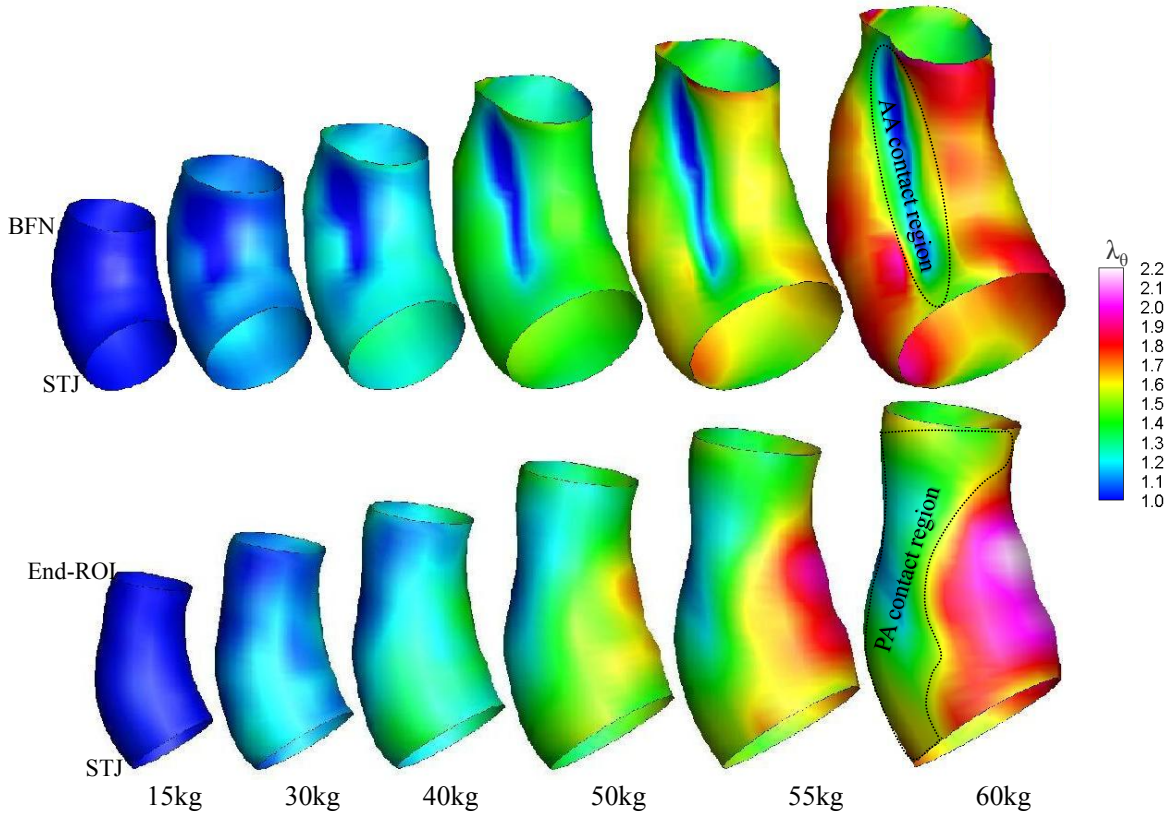

Figure 4

Figure 3.10. Time-interpolated circumferential growth stretch of PA and AA medial and posterior walls. Circumferential growth was highly heterogeneous in both PA (top) and AA (bottom) due to mutual radial constraints they impose on outlined regions of their respective medial walls and absence of constraint on their posterior aspects.

Most of the medial wall of the PA grew very little circumferentially compared to other aspects of the artery (1.12±0.012) while λ_θ of a large segment of the AA medial wall was not as substantially inhibited (1.43±0.071) (Figure 3.10 and Figure 3.14A). The circumferential growth of the PA lateral wall significantly decreased towards the BFN (from 1.69±0.11 to 1.28±0.067) (Figure 3.11 and Figure 3.14B). A similar, but less pronounced, trend was observed on the anterior wall, where towards the BFN, the λ_θ values dropped from a mean of 1.70± 0.066 to 1.48±0.035 (Figure 3.11 and Figure 3.14B). The average circumferential growth was

significantly larger on the posterior wall compared to the other three walls, and the pattern was relatively less heterogeneous (1.73±0.056) (Figure 3.10 and Figure 3.14B).

The circumferential growth patterns did not significantly change in the axial direction on most of the lateral wall of the AA (1.66±0.056) (Figure 3.11 and Figure 3.14C); however, λ_θ increased in the circumferential direction for less than 30% from anterior towards posterior walls. On the anterior wall of the AA, where the main side branch was located (Figure 3.11), circumferential growth appreciably changed, with the region located right after the side branch having significantly smaller growth (1.28±0.029) compared to the rest of that aspect (1.47±0.067). The largest circumferential growth in the AA occurred on a large segment of its posterior wall with λ_θ of 2.019±0.047 (Figure 3.10 and Figure 3.14C).

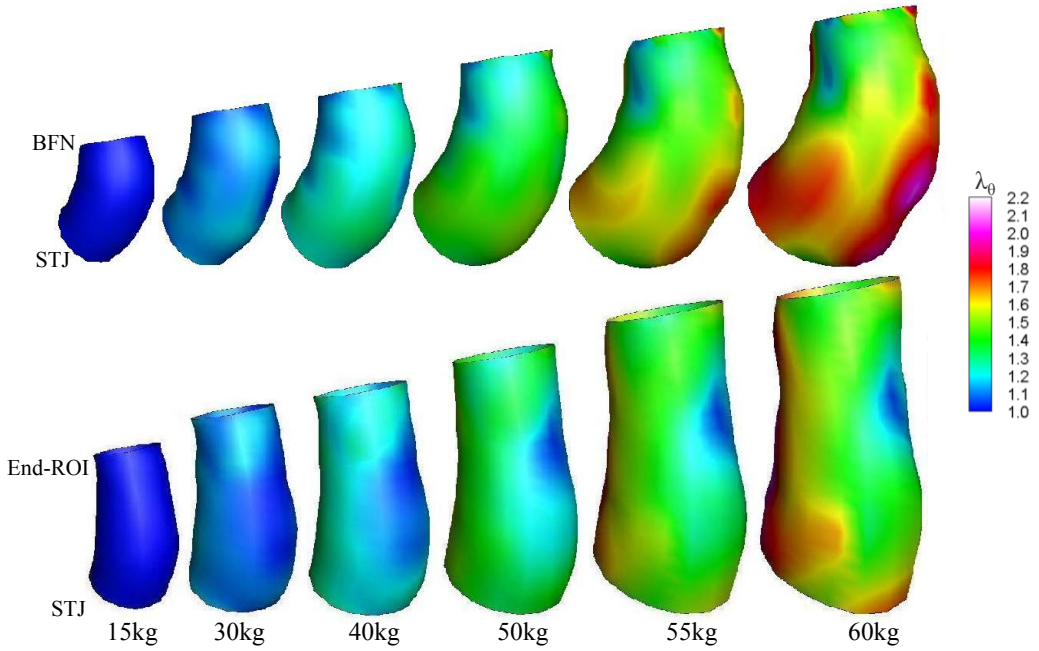

Figure 3.11. Time-interpolated circumferential growth stretch of PA and AA anterior and lateral walls. Proximal region to BFN of PA lateral wall (top), that appears to coincide with anatomical position of the auricle of the left atrium, grew about 60% less. A decrease of at least 20% in circumferential growth stretch values on corresponding region of PA anterior wall postulated to be due to connection with pericardial sac. Main side branch on anterior wall of AA (bottom) was slanted towards end-ROI resulted in 18% less growth on region located right after side branch. Large axial regions of anterior and lateral walls grew slower than posterior wall, most likely due to constraints of superior vena cava and left brachiocephalic vessel.

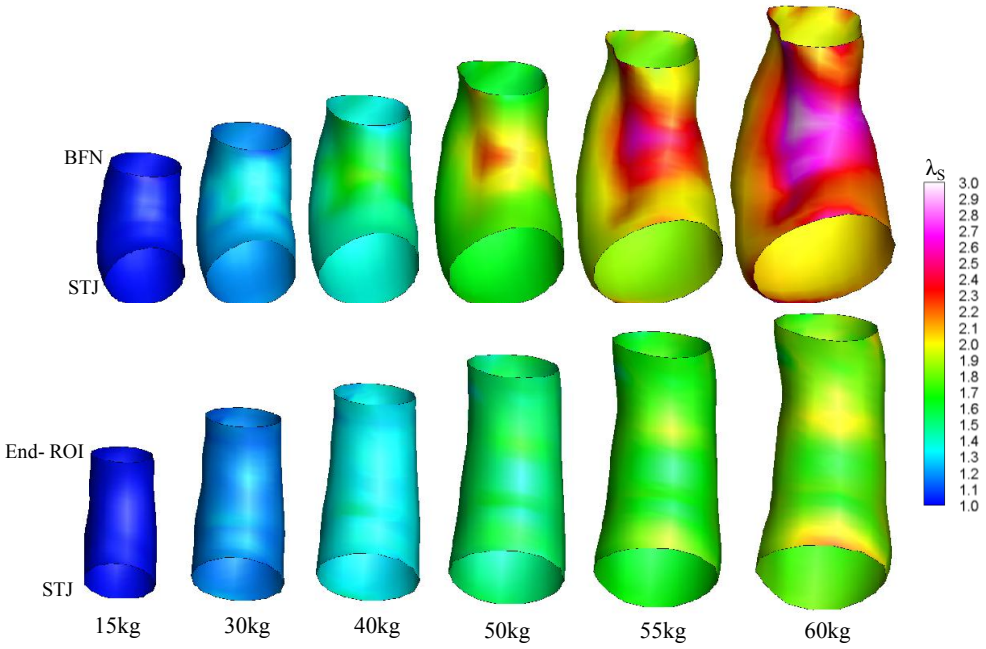

Figure 3.12. Time-interpolated longitudinal growth stretch of PA and AA posterior walls. Posterior and medial walls of PA (Top) were significantly larger, due to a larger curvature, than that of the posterior wall of AA (Bottom).

The longitudinal growth had considerably smaller degree of heterogeneity compared to the circumferential growth (Figure 3.12 and Figure 3.13). The posterior and medial walls and a portion of the lateral wall of the PA showed, respectively, progressively larger longitudinal growth with age (2.50±0.10) compared to most of the anterior wall, which had a slower and relatively uniform longitudinal growth (1.99±0.094) (Figure 3.12,Figure 3.13 and Figure 3.14E). The considerably larger longitudinal growth of the PA posterior wall as compared to the anterior wall was mainly due to its axial curvature and essentially unchanged tortuosity of the centerline path during the whole growth period (Figure 3.4). That is in order to maintain constant tortuosity, the posterior wall had to grow faster than the anterior wall (Appendix A3). Due to the absence of a comparable axial curvature in the AA (Figure 3.5B), for most part, the longitudinal growth of the AA was relatively smaller and less heterogeneous with a mean of 1.80±0.023 (Figure 3.12-

Figure 3.14F). The presence of a relatively large curvature on a small region of the posterior wall resulted in a slight rise in λ_s (Figure 3.12 and Figure 3.14F).

The areal stretch was less heterogeneous than either the longitudinal or circumferential stretch in the PA. The lateral wall consistently had relatively smaller areal stretch starting about 30% away from BFN (2.77±0.18) compared to the rest of that wall (3.72±0.13). The medial wall had on average the smallest growth as measured by an areal stretch of 2.88±0.28. The posterior wall grew the most (4.19± 0.22) with anterior wall having the next largest growth in surface area (3.31±0.26). The areal stretch of the AA was only slightly non-uniform on the medial and anterior walls with means of 2.72±0.21 and 2.51±0.22, respectively. The change in surface area was fairly constant and larger on the lateral wall of the AA in the axial direction (3.03±0.12) with the posterior wall growing the most (3.44±0.29).

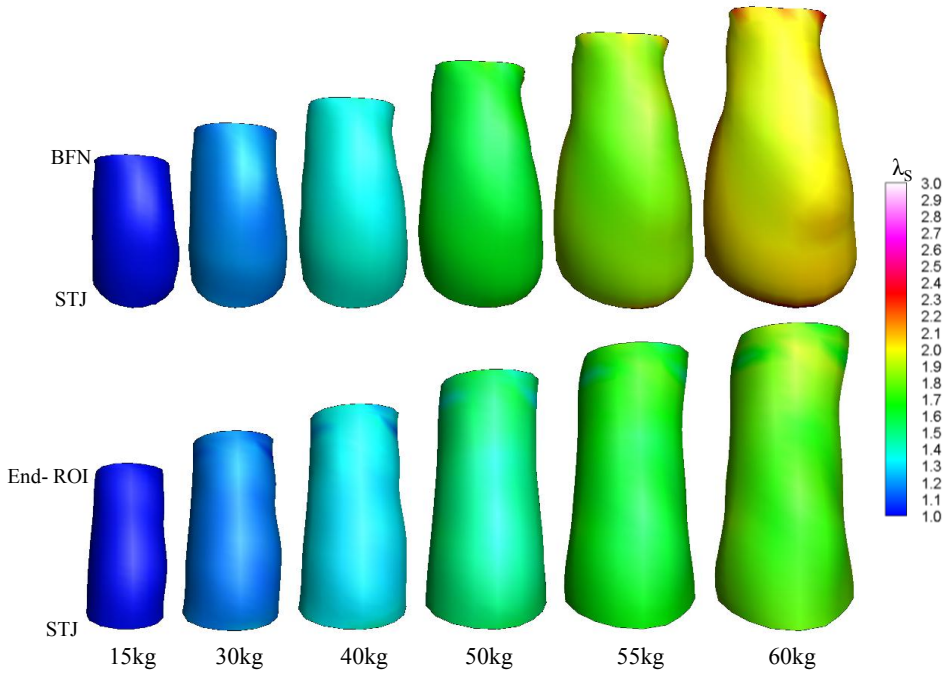

Figure 3.13. Time-interpolated longitudinal growth stretch of PA and AA anterior walls. Longitudinal growth of PA (Top) and AA (Bottom) uniformly changed with age with larger growth of PA anterior wall at the 60-kg growth stage attributed to its larger curvature than that of AA.

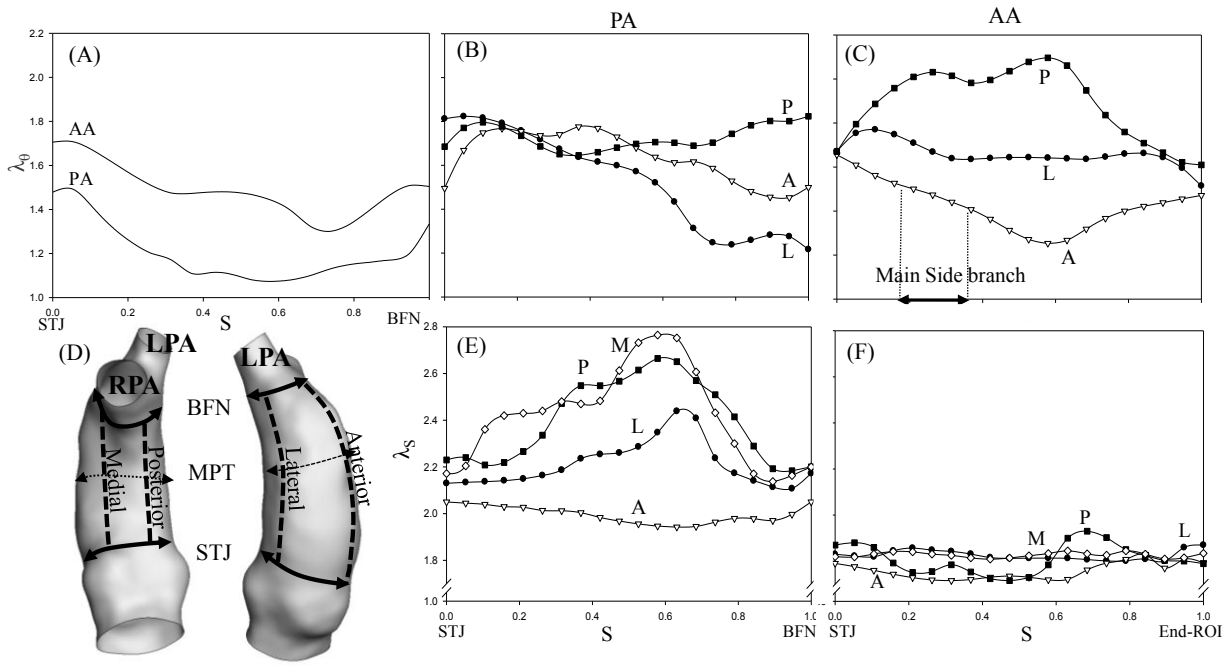

Figure 3.14. Circumferential growth stretch profiles of PA and AA at the adult stage (60 kg). Circumferential growth of PA and AA medial walls (M) shown in (A), and those of lateral (L), anterior (A) and posterior (P), with approximate position of AA main side branch, shown in (B) and (C), respectively. The paths along four walls and locations for the computation of growth rates are illustrated in PA (D). Longitudinal growth stretch profiles along four walls of PA and AA, shown in (E) and (F), respectively.

3.2.3 Growth Rates

The growth rates were computed in the STJ, middle point (MPT) regions and the BFN region in the PA (Figure 3.14D) or end-ROI region in the AA on all four aspects of each artery (Table 3.1). Both circumferential and longitudinal growth rates increased with age as compared at four different growth stages from youngest to oldest time points (except $\dot{\lambda}_s$ of the AA was constant up to 35-kg growth stage). For the most part $\dot{\lambda}_\theta$ of the PA was small up to about the 35-kg growth stage (about 4 months of age) and increased approximately linearly thereafter. The AA circumferential, however, was relatively more linear with smaller change in growth rates. The

circumferential growth rate on the 'contact' segment of the medial wall of the PA was substantially smaller than that of the corresponding segment of the AA medial wall.

Table 3.1. Circumferential and longitudinal surface growth rates in PA and AA.
Rates computed after ~35 kg growth stage in four circumferential and three longitudinal regions (reported as mean±SD in %/kg).

Artery	Axial region	Circumferential Growth Rate				*Mean*
		Medial	Posterior	Lateral	Anterior	
PA	STJ	1.5±0.5	2.3±0.7	2.4±1.3	1.9±0.6	2.0±0.8
	MPT	0.48±0.12	3.0±1.1	1.1±0.5	1.9±0.6	1.6±0.6
	BFN	0.24±0.03	1.9±0.6	0.48±0.13	0.83±0.16	0.9±0.2
AA	STJ	1.6±0.06	2.7±0.7	1.3±0.2	1.5±0.5	1.8±0.4
	MPT	1.1±0.05	2.9±0.8	1.7±0.3	0.50±0.25	1.6±0.4
	End-ROI	1.5±0.2	2.1±0.5	1.1±0.02	1.0±0.1	1.4±0.2

Artery	Axial region	Longitudinal Growth Rate			
		Medial	Posterior	Lateral	Anterior
PA	STJ	2.9±0.7	3.3±1.0	3.3±0.7	3.4±0.9
	MPT	4.6±1.1	4.2±0.9	3.6±0.9	2.3±0.6
	BFN	2.9±0.7	3.5±0.9	2.8±0.7	2.2±0.6
	Mean	3.5±0.8	3.7±0.9	3.2±0.8	2.6±0.7
AA	STJ	1.7±0.4	2.5±0.7	1.5±0.7	1.7±0.4
	MPT	1.9±0.4	2.1±0.4	2.3±0.6	1.6±0.4
	End-ROI	1.9±0.4	1.9±0.4	1.4±0.7	2.1±0.4
	Mean	1.8±0.4	2.2±0.5	1.7±0.7	1.8±0.4

3.3 DISCUSSION

3.3.1 Overview

This study is the first to investigate the spatial and temporal postnatal growth changes in the geometry (expressed as a deformation) of the AA and PA during the postnatal development. Knowledge of normal arterial growth kinematics can shed light on mechanisms guiding development and allow detection of deviations that can change arterial mechanics, which can set the stage for the development of a degenerative disease [130]. As an example, it has been determined that during normal embryogenesis the truncus arteriosus begins to split and form into the anterior pulmonary artery and the posterior aorta [12]. Possibly due to their common embryologic origin from a single outflow tract, there are disease conditions that originate in one artery and eventually affect both arteries [19, 131]. This provided an additional reason to characterize the growth deformation of both the AA and PA to quantify the degree of mechanical association of these two arteries.

3.3.2 General Trends and Implications

The key findings from the initial study were that the postnatal volumetric growth of the pulmonary and aortic root as well as the PA and AA scaled with the weight of the animal, and occurred at the same rate in both arteries. Despite considerable increase in actual length, the PT maintained its tortuosity while the contribution of the sinuses of the Valsalva to its length decreased over time. The alterations in the surface geometry of the PT were found to be

considerably non-uniform as compared to the AA. The cross-sectional shape of PT became more elliptical with age and more non-uniform along its length.

The surface growth deformations revealed that the region of the medial PA wall in contact with AA had the smallest computed growth at the 12-month postnatal stage. A large segment of the AA medial wall and part of its posterior wall, which is proximal to the end-ROI (where the PA wraps around the AA), showed about 40% to 70% smaller circumferential growth. The lack of significant growth on the sections of both arteries, where they are associated with each other, implies that both mutually impose radial constraints. The circumferential growth rate on the AA medial wall in the PA-coupling region was about four times as fast as that of the corresponding region on the PA medial wall. Therefore, the constraint imposed by the AA on the PA had a substantially larger inhibiting effect on the PA circumferential growth than vice versa.

The lateral wall and anterior walls of the PA showed, respectively, the next highest degrees of spatial heterogeneity. The region proximal to the BFN of the PA lateral wall, that coincides with the anatomical position of the auricle of the left atrium, had an average circumferential growth comparable to that of the medial wall of the PA and grew about a quarter as fast as the rest of that wall. On the anterior wall of the PA, we speculate that the decrease of at least 20% in circumferential growth stretch values in the vicinity of the BFN is due to the connections to the ligamentum arteriosum in that region.

The circumferential growth patterns of the rest of the AA seemed to be also guided by the presence of surrounding tissue impingements. On the anterior wall of the AA due to the main side branch being slanted towards the end-ROI, the region located after the main branch showed an average of about 18% less growth than other areas of that wall, resulting in the circumferential growth rate slowing down by a factor of about two and a half. Compared to the

posterior wall, the relatively slower growth on the large axial region on the anterior wall extending to the lateral wall appears to be caused by the constraints imposed by the superior vena cava and the left brachiocephalic vessel.

The orientations of the major axes of cross-sections along each artery relative to that of the STJ section remained fairly unaltered in both arteries. This is an indication that the locations of surrounding tissue structures or constrains are relatively unchanged during postnatal growth. This observation supports the assumption that the relative location of surface material points during the study timeline were somewhat persevered.

It was demonstrated that both arteries became increasingly tapered towards the BFN and end-ROI during postnatal maturation. However, the PA taper increased from 0.86 (i.e. nearly straight) to 0.67 (for the adult) while the AA tapered at a slower rate from 0.74 to 0.62 (Figure 3.9B). The study by Huang et al. [54] also reports increasing taper in the AA of mice during the postnatal growth stage. The aforementioned constraints proximal to the BFN on the lateral and anterior walls of the PA probably have resulted in slower circumferential growth compared to more distal regions, and explain the increase in PA taper towards the BFN with age. The presence of the main side branch between the STJ and the end- ROI regions in the AA is the cause of its greater taper compared to the PA. The radial impingement of the PA on the posterior wall of the AA proximal to the end-ROI limits growth in that region and leads to an increase in axial taper as the rest of the posterior wall of the artery is considerably less constrained to grow.

The existence of taper in the AA has been recognized as a physiological adaptation allowing for the optimization of pulsatile flow and favorable wave reflective properties that are inherent to the design of the conduit arteries [132]. The arterial taper enables connecting segments of the cardiovascular system that have different wave propagation or input impedance

properties in order to decrease blood flow fluctuations [133] and wave reflection. Therefore, the increase in taper with growth can lead to a more efficient wave propagation properties of the AA and PA with the rise in hemodynamic demands in larger ovine.

The cross-sectional geometry of both arteries was elliptical, with the PA ellipticity increasing significantly with age compared to the AA. The significant radial impingement of the AA on a large segment of the PA's medial wall along with considerable growth on most of the posterior and anterior walls of the PA results in the increase in cross-sectional ellipticity with age. In the generated torus phantom the circumferential stretch was also axially variable due to the phantom becoming more tapered and was circumferentially variable due to increase in ellipticity (Figure 3.15B, D).

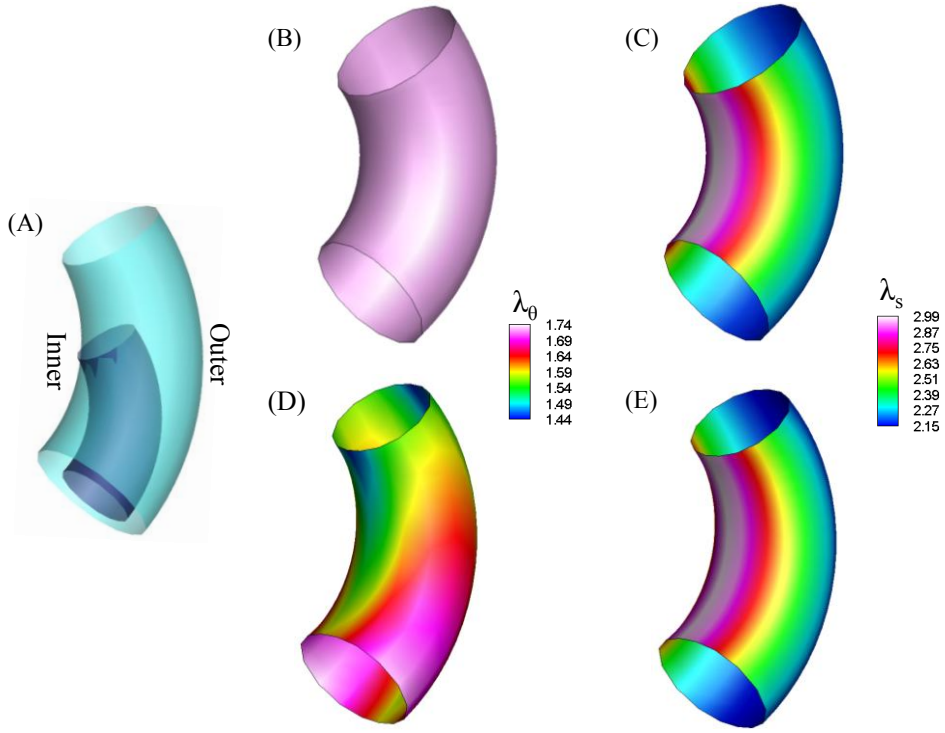

Figure 3.15. Torus phantoms to verify implementation of growth deformation analysis. 'Juvenile' phantom was affinely enlarged by a factor of 2.33 to obtain 'adult' phantom (A), (B) and (C). Additionally, it was increased in taper by 20% and cross-sectional ellipticity by 30%, (D) and (E). Circumferential stretch was axially variable due to the phantom becoming more tapered and was circumferentially variable due to increase in ellipticity (D). The longitudinal stretch was larger on the inner aspect as compared to the outer aspect (C) and (E), which indicates that in order for a torturous artery to maintain constant axial curvature, it has to grow more on the aspect with larger curvature.

The PA longitudinal growth patterns did not significantly change with age; λ_s was on average more than 50% larger and more heterogeneous on the posterior, medial, and a small area on the lateral walls. The longitudinal growth patterns resembled those of the torus phantom with the inner surface growing significantly more than the outer surface, which indicates that in order for the artery to maintain a constant axial curvature, its posterior wall, with larger curvature, had to grow more than the anterior one (Appendix A3). This phenomenon was also demonstrated in the torus phantom results of Figure 3.15C,E. The large λ_s on the medial wall was a result of the concaved shape of the vessel in that region due to mechanical coupling with the AA. The relatively smaller and more uniform longitudinal growth in the AA is due to the absence of comparable axial curvature to the PA.

Understanding normal arterial morphogenesis can yield unique insight into the mechanisms of vascular adaptations and their important physiological factors. As explained, there is probably a dynamic interplay between arterial growth kinematics, pulsatile blood flow, and arterial hemodynamics. As demonstrated, the existence of and changes in geometric features such as curvature and torsion lead to spatial variations in the vessel wall. These geometric features can also result in hemodynamic conditions leading to disease localization [134, 135]. Furthermore, due to the correlation between vessel geometry and its microstructure, the change in morphology of the artery as it grows will result in changes in its mechanical properties [56-58]. Additionally, the data on growth deformation patterns allows computation of changes in stress distribution, which is an important measure of the onset of disease and an indicator of predisposition to a variety of vascular pathologies.

3.3.3 Limitations

Since the animals used here were sacrificed at varying times for other non-related studies, the same individual animals could not be imaged for the entirety of the study. However, the growth trends found in both arteries for all animals were very consistent. Furthermore, since it was not practical to place surface markers on either artery to track growth during the one-year length of study, it was assumed that the relative spatial locations with respect to in-surface coordinates were maintained within the growth period. This assumption was supported by the registration results and especially the similarity in shapes of the scaled centerline paths over the entire growth period, which demonstrated that the overall arterial shape was maintained despite local changes in geometry.

3.3.4 Summary

This study demonstrated, for the first time, highly heterogeneous growth deformation profiles with variable growth rates during the normal postnatal development of the AA and PA. The heterogeneous circumferential growth patterns led to an increase in taper in both arteries and in cross-sectional ellipticity in the PA. This was a result of the surrounding tissues and the physical interaction between the vessels considerably constraining the geometric remodeling of both arteries. Interestingly these external forces had a significantly larger effect on the PA growth patterns compared to the AA. Due to the larger tortuosity of the PA, its posterior wall had to grow more rapidly in the longitudinal direction than its anterior aspect; whereas the longitudinal growth patterns in the AA were comparatively less heterogeneous. The present results will lay

the basis for a full growth and remodeling simulation of implants in developing individuals, including normal and congenitally defective patterns in humans.

4.0 REGIONAL CHARACTERIZATION OF THE MECHANICAL BEHAVIOR

The work in this chapter fulfills the first part of the second specific aim (section 1.7). The knowledge of biaxial mechanical behavior of the arterial wall is of great significance as outlined in sections 1.3.3 and 1.4. Based on the surface growth patterns delineated in Chapter 3.0, the mechanical behavior of the PA wall in four regions around its circumference was characterized at two growth stages. Initially, the biaxial behavior of the AA and PA in the porcine model was characterized in order to gain insight into the nature of differences in the mechanical properties of these two major arteries. Finally, the residual strain of the PA wall was quantified at the STJ and BFN in order to characterize arterial wall remodeling patterns during the normal growth process. The results from the porcine AA and PA study suggested that the PA has more viscous properties than the AA. Additionally, the PA stress-stretch loading path was more nonlinear than the AA. The mechanical behavior of the PA was quite heterogeneous in each growth stage. The circumferential stiffness among the four regions was relatively similar while the longitudinal stiffness was significantly heterogeneous. The medial wall became considerably more anisotropic while the biaxial mechanical properties of the anterior and posterior walls were maintained. The endoluminal and abluminal circumferential residual strain at the BFN was smaller compared to the STJ and significantly decreased with growth while it was fairly preserved at the STJ.

4.1 METHODS

The postnatal growth period was represented by two age groups of 4-5 months and 10-12 months old, considered juvenile and adult, respectively, in Dorset ovine. For each age group ten fresh Dorset ovine PT specimens were obtained from local slaughterhouse for each of the biaxial mechanical and residual strain measurement experiments. Specimens were carried in PBS on ice for about 45 minutes before arriving at the laboratory to be either tested or stored in the -80^{o}C freezer. The age of the animal was verified by the size of its pulmonary trunk.

4.1.1 Biaxial Testing

A detailed description of the biaxial testing device (Figure 4.1) has been previously presented [65, 136, 137]. A summary of specimen preparation and biaxial system is provided below.

Arterial wall samples were cut into squares of appropriate size (sections 4.1.1.2 and 4.1.1.3); thickness measurements were taken at three locations using a micrometer Starrett® Model 1010 thickness gage (The L.S. Starrett Company) and averaged. Stainless steel hooks, 0.016 inch in diameter, were tied to both ends of 10 cm long silk suture lines and were attached to the specimen with four hooks per side forming two loops of suture (Figure 4.1). A total of sixteen hooks were placed creating four pairs of sutures. Four small cut portions of polypropylene suture were affixed to the middle region of the specimen in a square pattern using small amount of cyanoacrylate glue to serve as fiducial markers. Specimens were submerged in room temperature PBS bath and mounted onto the biaxial device with the circumferential and longitudinal directions aligned with the X_1 and X_2 axes, respectively.

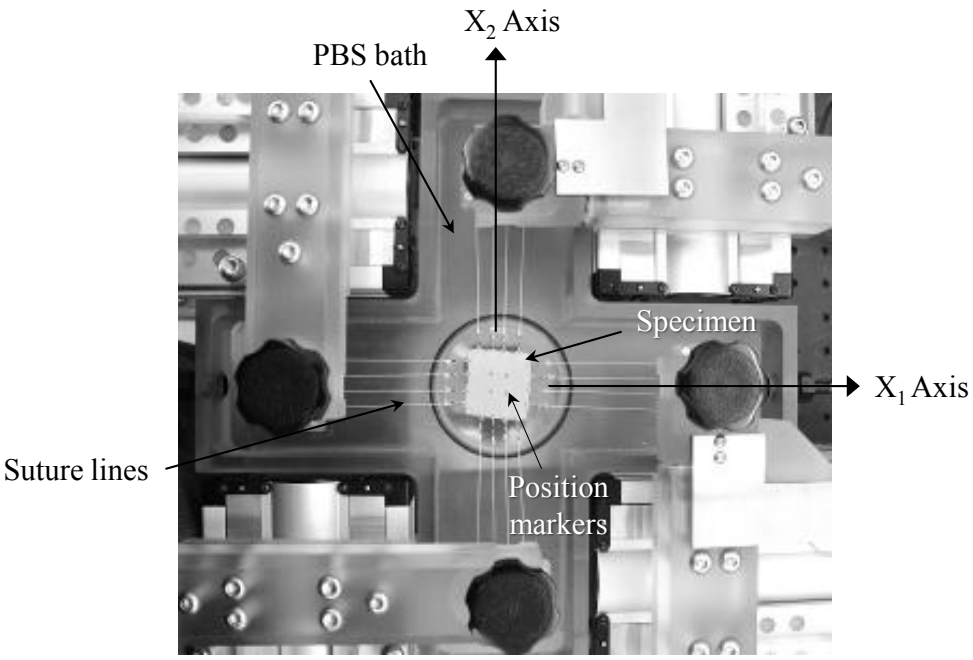

Figure 4.1. Biaxial mechanical experimental setup.

Using custom-written control software, load control biaxial mechanical testing was performed. The samples were taken through ten preconditioning cycles for each biaxial stress protocol. The marker positions in the free-floating (no-load) reference states were saved before start of the test, after the initial ten equibiaxial stress preconditioning cycles (post-preconditioned), and finally after the seven-protocol biaxial testing was finished (post-test). The post-preconditioned state was used as the reference for all the seven protocols. A 0.4-0.6 gram tare load was applied to the specimen to enable proper device operation.

4.1.1.1 Biaxial Tensile Testing Analysis

The gage lengths as determined from marker positions from the unconstrained or free-float post-preconditioned states were used as the reference for all strain calculations. The biaxial deformation of soft biological tissues is generally very heterogeneous. In order to calculate

deformation of a planar biaxially loaded arterial wall sample, using limited number of fiducial markers, it was assumed that the deformation within the marker-delimited area is homogeneous. The stretch calculation method used is well documented for soft tissues [62, 138]. The generalized planar biaxial deformation is considered to be

$$x_1 = \lambda_1 X_1 + \kappa_1 X_2, \qquad x_2 = \lambda_2 X_2 + \kappa_2 X_1, \tag{3.1}$$

where X and x are the locations of material particles in the reference and deformed states, respectively, and λ_i and κ_i, being the in-plane stretch ratios and shear. The locations of markers are tracked the using an optical tracking software. X_n, where n is the marker number, are the pixel coordinates of the marker positions in the reference configuration and x_n, are the deformation-dependent marker coordinates. Shape functions are used to map the real pixel coordinates into an isoparametric coordinate system (Figure 4.2) such that the marker displacements u can be calculated as the linear sum of the isoparametric shape functions according to

$$\mathbf{u}(\xi,\eta) = \sum_{n=1}^{4} f_n(\xi,\eta)\mathbf{u}_n, \tag{3.2}$$

where f is the set of isoparametric shape functions; ξ and η are the isoparametric coordinates.

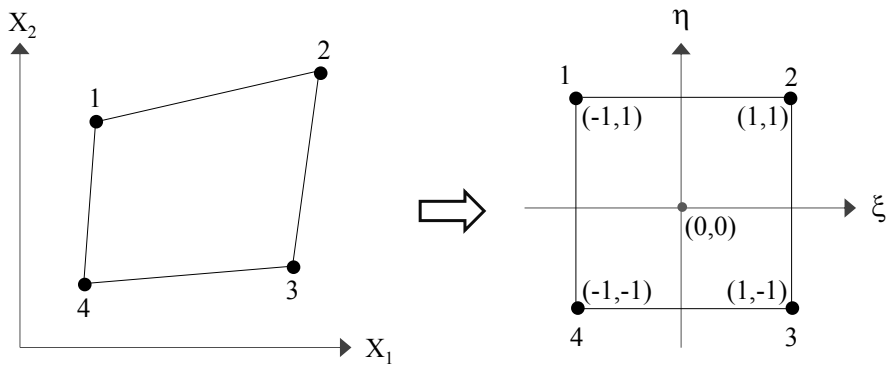

Figure 4.2. Mapping of marker coordinates into an isoparametric coordinate system.

The spatial derivatives of **u** with respect to ξ andη can then be calculated as

$$\frac{\partial \mathbf{u}}{\partial \xi} = \sum_{n=1}^{4} \frac{\partial f_n}{\partial \xi} \mathbf{u}_n, \quad \frac{\partial \mathbf{u}}{\partial \eta} = \sum_{n=1}^{4} \frac{\partial f_n}{\partial \eta} \mathbf{u}_n \tag{3.3}$$

which can be used to derived the spatial derivatives of ***u*** with respect to ***x*** can using the relation

$$\begin{bmatrix} \frac{\partial \mathbf{u}}{\partial \xi} \\ \frac{\partial \mathbf{u}}{\partial \eta} \end{bmatrix} = \begin{bmatrix} \frac{\partial x_1}{\partial \xi} & \frac{\partial x_2}{\partial \xi} \\ \frac{\partial x_1}{\partial \eta} & \frac{\partial x_2}{\partial \eta} \end{bmatrix} \begin{bmatrix} \frac{\partial \mathbf{u}}{\partial x_1} \\ \frac{\partial \mathbf{u}}{\partial x_2} \end{bmatrix} \tag{3.4}$$

These spatial derivatives comprise the components of the of the deformation gradient, F_{iJ}, from which λ and κ can be determined by

$$F = \begin{bmatrix} \frac{\partial u_1}{\partial X_1} & \frac{\partial u_1}{\partial X_2} \\ \frac{\partial u_2}{\partial X_1} & \frac{\partial u_2}{\partial X_1} \end{bmatrix} = \begin{bmatrix} \lambda_1 & \kappa_1 \\ \kappa_2 & \lambda_2 \end{bmatrix} \tag{3.5}$$

Since soft tissues are composed primarily of water, they can be considered incompressible so that J = det(**F**) = 1; thus, λ_3 is calculated from the components of **F** (section 2.4.1). The corresponding Lagrangian-Green strain tensor was calculated according to Eq. (2.11). Using the measured axial loads, the deformation gradient tensor and the initial specimen dimensions, Cauchy stress tensor **σ** at each time t was calculated. The first and second Piola-Kirchhoff stresses (**P** and **S**, respectively) were computed using the deformation gradient tensor and **σ** according to Eqs. (2.18) and (2.19).

The shear components of the deformation gradient and stress tensors can be considered negligible if fibers are mainly aligned or symmetrically distributed along either loading axes; in that case, the two remaining major stress components, $S_{11}(E_{11}, E_{22})$ and $S_{22}(E_{11}, E22)$, can be determined from planar biaxial testing and used in developing the constitutive equation.

4.1.1.2 Comparative study of the PA and AA in porcine model

Fresh adult porcine hearts (n=8) with intact AAs and PTs were obtained from the local abattoir. A porcine model was chosen because of its similar anatomy and biomechanics to human cardiovascular system. Before performing biaxial testing on all samples, the maximum stress level for conducting a one-to-one comparison of the two arteries mechanical properties had to be determined. Therefore, the effect of stress history on the biaxial behavior was evaluated on three samples from each artery by subjecting each sample to ten cycles of preconditioning sequentially to maximum equibiaxial stress levels of 40 kPa, 60 kPa, 80 kPa and again 40 kPa. Based on the results obtained, each pulmonary and aortic sample was biaxially loaded to the estimated average respective pulmonary and systemic physiologic hoop stresses of 30 and 80 kPa. One specimen from each of the central regions of medial and lateral walls were excised from each artery. The specimens were cut into squares of 15 mm per side. The specimens were subjected to equibiaxial stress controlled testing.

4.1.1.3 Study of postnatal mechanical properties of PA

From each artery four square samples were excised from the following four locations around the circumference (Figure 4.3): medial, lateral, posterior and anterior. The specific location of samples on each of four walls was chosen based on the circumferential growth deformation profile reported in Chapter 3.0. Each set of four specimens was tested on the same day. Specimens were cut into squares of 10-15 mm per side.

Each specimen was taken to a maximum biaxial stress of 35 kPa which is approximately equivalent to the peak systolic stress level. The complete seven-protocol planar biaxial routine consisted of the following stress controlled circumferential-to-longitudinal stress ratio: 8.75:35, 17.5:35, 26.25:35, 35:35, 35:26.25, 35:17.5 and 35:8.75 kPa. For each protocol, specimens were

taken through contiguous loading and unloading cycles of preconditioning until cycles became repeatable or a steady state was achieved. The loading and unloading paths of all specimens became repeatable in less than 5 preconditioning cycles. The loading duration was set to 10 seconds resulting in strain rates of 3-4 percent/sec and 5-6.5 percent/sec, in circumferential and longitudinal directions, respectively.

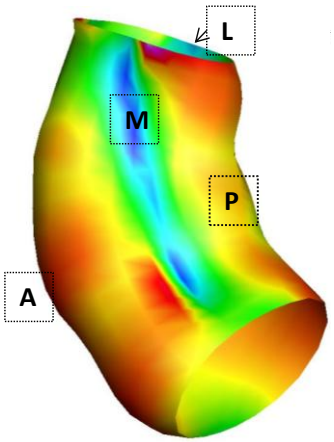

Figure 4.3. Locations of biaxial samples excised from PA anterior (A), medial (M), posterior (P), and lateral (L) walls.

4.1.2 Residual Strain Measurement

The residual strain measurements were performed immediately following the arrival of the tissue from the slaughterhouse. One ring from the STJ and one ring from the BFN regions of the fresh PA were excised. A large number of black water-insoluble ink dots were placed uniformly along the thickness of the ring with a fine brush to better identify endoluminal and abluminal surfaces (Figure 4.4). To allow tissue re-equilibration and inhibit protease activity, the ring was initially placed in a PBS-PMSF solution at 37^{o}C for 20 minutes. Thereafter, the ring was placed in a tank containing PBS and papaverine-HCl to relax the smooth muscle cells; the temperature was

maintained at approximately 37°C by circulating the tank solution through a Julabo heater bath (Julabo Labortechnik GmbH, Seelbach, Germany; Figure 4.4). The rings were attached point-wise with a high viscosity glue to a small insulated wire piece (1 mm in diameter) attached to a stable base to keep the ring in one location and the edges in the right orientation towards the camera. After a few minutes, a lateral cut was made on the ring. A custom-written Labview program (National Instruments Corporation, Austin, TX) was run to acquire an image every 2 minutes for 30 minutes. ImageJ software (National Institute of Health Image, http://rsb.info.nih.gov/ij/) was used to measure the lengths of endoluminal and abluminal surface boundaries in the intact and final state of cut specimens. The circumferential residual strain was calculated in the cut ring with respect to unloaded state according to

$$E_{RS\theta} = \frac{1}{2}\left(\lambda_{RS\theta}{}^{2} - 1\right),$$

where $\lambda_{RS\theta} = \frac{L_{intact}}{L_{cut}}$.

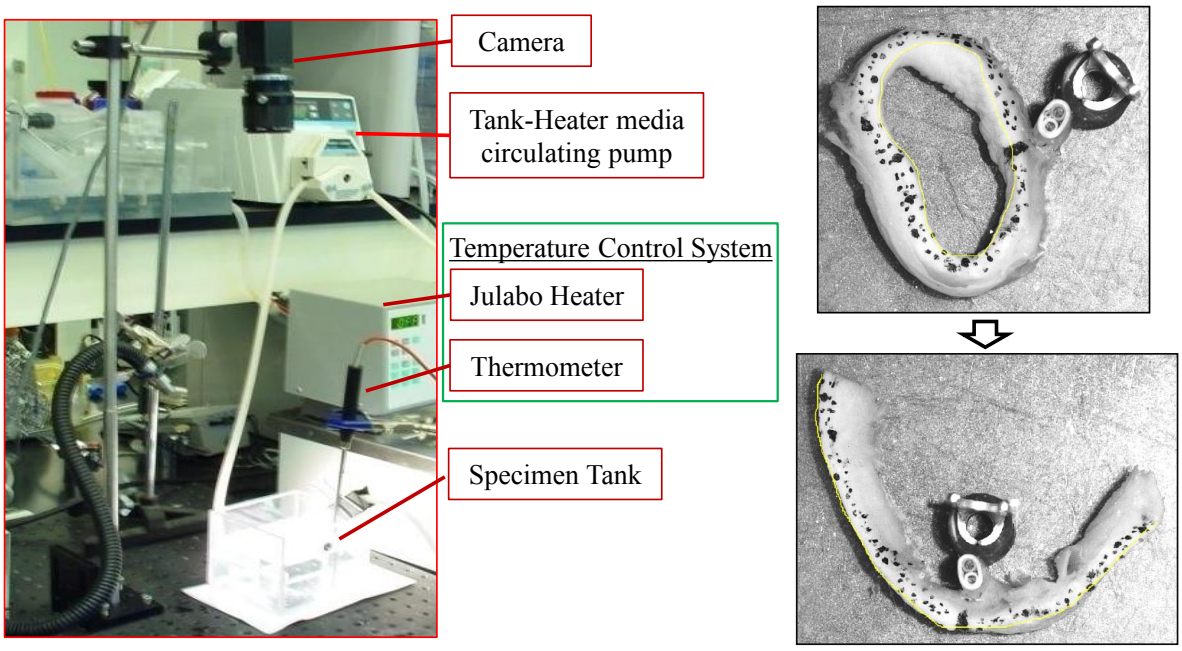

Figure 4.4. Residual strain measurement experimental setup (left). Ring (unloaded) and cut (stress-free) specimens (right).

4.1.3 Statistical Analysis

Statistical analysis was performed using the SPSS software. A mixed factorial analysis of variance (ANOVA) was performed for the between-subjects variables of age and within-subject variables of location and direction (SPSS software). The Mauchly's test of sphericity was performed for examining the equality of error variances. The multiple post hoc comparisons were made using the Bonferroni correction when error variances were similar and the Greenhouse-Geisser post-hoc adjustment was made when homogeneity of variance was violated. A one-tailed value of $p < 0.05$ was considered statistically significant. The effect size r was calculated for each statistical comparison to determine whether the difference between data was substantive (the threshold for a large effect is defined to be above 0.5). All values are reported in terms of mean ± standard error (SEM).

4.2 RESULTS

4.2.1 Biaxial Behavior

4.2.1.1 Comparative study of the PA and AA in porcine model

The initial and final 40kPa loading paths of the same specimens did not coincide in the higher stress regions in both circumferential and longitudinal directions; the stress-stretch curves of each protocol instead followed more closely the immediately preceding curve (Figure 4.5). Therefore, the PA wall retained its loading history, and the preconditioning for each protocol did

not ‘reset’ the mechanical behavior of the PA wall. However, all the loading paths of the AA coincided (Figure 4.5).

The PA biaxial behavior was nearly isotropic in the middle region of the medial wall (p>0.2) while the lateral wall samples exhibited significant anisotropy (p<0.03). The AA biaxial behavior was significantly anisotropic at both locations (p<0.01, Figure 4.6). Therefore, the biaxial behavior of the PA was more heterogeneous than that of the AA. The AA maximum equibiaxial stress value was approximately 2.7 times larger than that of the PA maximum. However, the mean peak circumferential and longitudinal stretches of the AA at both locations, 1.20±0.02 and 1.36±0.04, respectively, were close to that of the PA with respective peak circumferential and longitudinal stretches of 1.28±0.02 and 1.36±0.04.

The tangential moduli of both arteries were calculated based on the slope of the mean first Piola-Kirchoff stress of the equibiaxial stress loading path (Figure 4.6). The deformation-stiffening response of the AA was fairly linear; however, the PA tangential modulus was nonlinear remaining relatively constant up to about 13 to 18% stretch and increased linearly thereafter (Figure 4.7). The AA showed a much larger degree of anisotropy with 1.8±0.1 times larger circumferential tangential modulus than the longitudinal modulus.

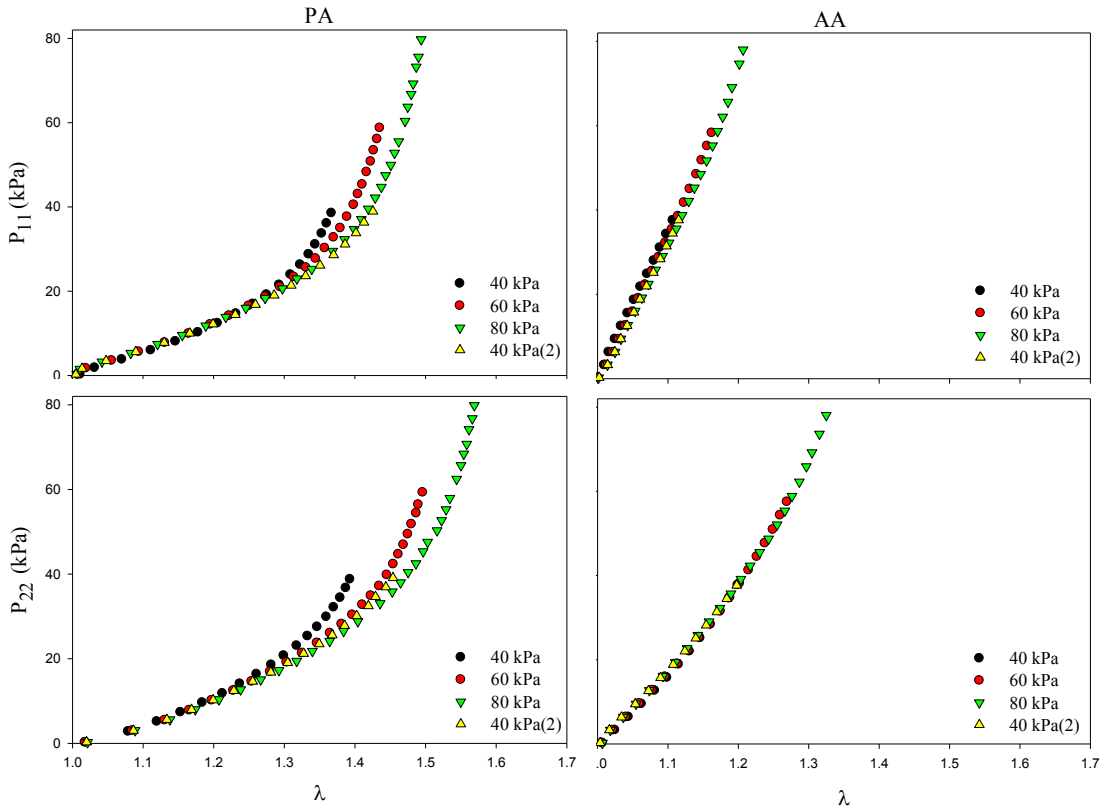

Figure 4.5. Effect of loading history on porcine PA and AA stress-stretch curves despite preconditioning. Representative circumferential (top) and longitudinal (bottom) equibiaxial stress loading paths of PA and AA samples after sequentially preconditioned to each of maximum stress levels of 40 kPa, 60 kPa, 80 kPa and 40 kPa.

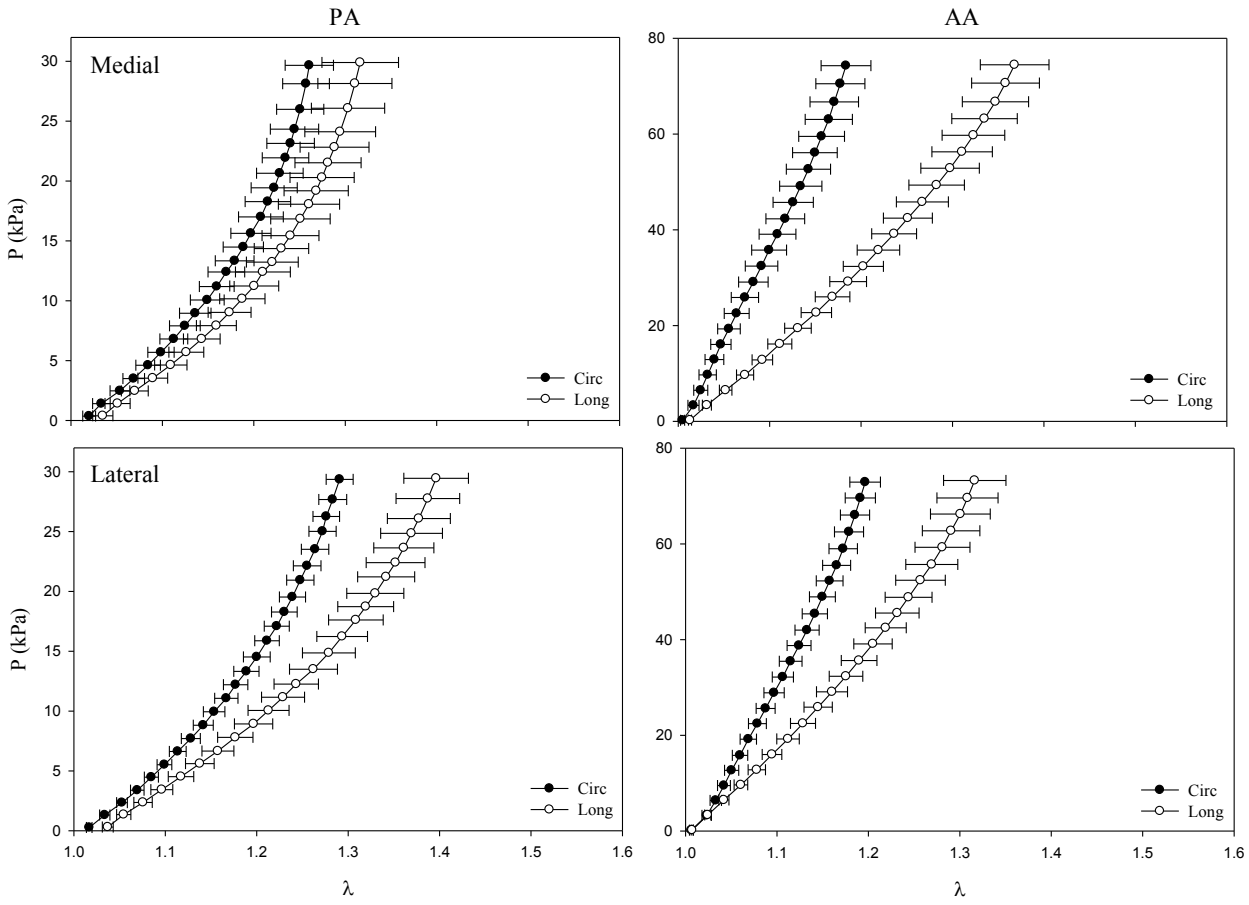

Figure 4.6. Equibiaxial stress-controlled behavior of porcine PA and AA.
PA response is more nonlinear as well as heterogeneous, with its medial wall (top) nearly isotropic and lateral wall (bottom) anisotropic, compared to AA. Although AA maximum applied biaxial stress value was about 2.7 times larger than that of the PA, mean peak circumferential and longitudinal stretches of AA at both locations, 1.20±0.02 and 1.36±0.04, respectively, were very close to that of PA with peak longitudinal stretch of 1.28±0.02 and circumferential stretch of 1.36±0.04.

The mean ratio of the circumferential to longitudinal moduli of the PA were only 1.32±0.01 in the medial and 0.89±0.03 in the lateral walls. The tangential moduli of the AA in circumferential and longitudinal directions were 406±43 and 209±50 kPa, respectively, in the medial location and 389±71 and 249±65, respectively, at the lateral wall. The PA wall was significantly more complaint with respective circumferential and longitudinal tangential moduli of 126±70 and 146±86 kPa at the medial and 121±49 and 91±37 at the lateral walls (p<0.01).

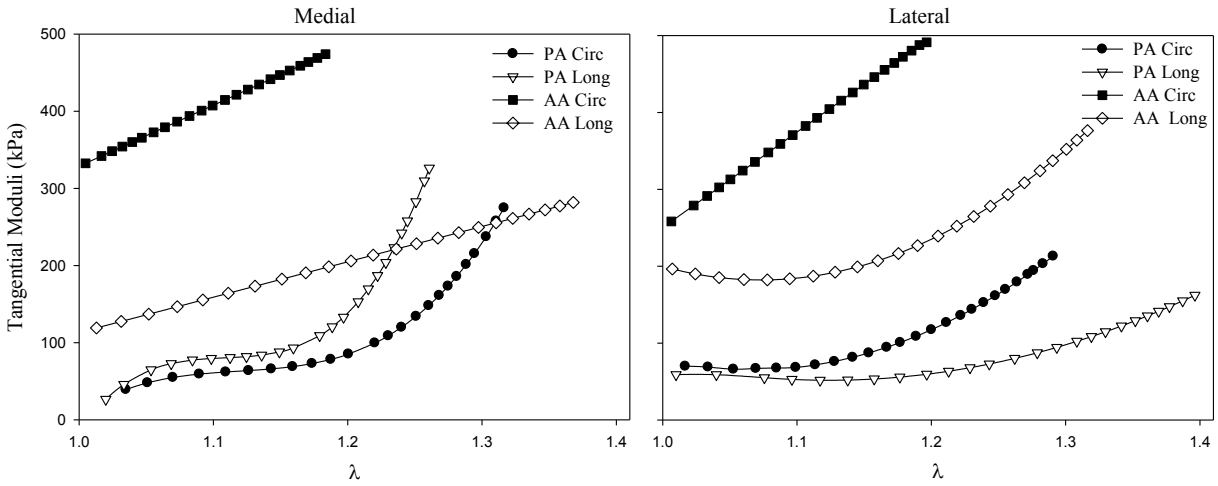

Figure 4.7. Tangential moduli of porcine PA and AA equibiaxial stress-stretch loading paths. Deformation-stiffening response of the AA was fairly linear while PA tangential modulus was constant up to about 13 to 18% stretch and increased linearly thereafter. The AA showed much larger degree of anisotropy with 1.8±0.1 times larger circumferential tangential modulus than the longitudinal modulus. The circumferential modulus was only 1.32±0.01 and 0.89±0.03 times the longitudinal modulus in PA medial and lateral samples.

4.2.1.2 Postnatal growth alterations of PA

The spatial variation of the thickness of the biaxial specimens, measured before testing, was significant. The anterior and posterior locations had similarly larger thicknesses (1.6±0.08 mm) compared to medial and lateral positions (1.14±0.05 mm, $p<0.006$) in the juvenile Ovine group (Figure 4.8). The regional thickness change with growth was not significant ($p>0.06$).

The biaxial loading curve for each protocol was stable and repeatable after the first two to three preconditioning cycles. A representative raw stress and deformation data for all seven biaxial protocols is shown in Figure 4.9. The deformations due to preconditioning in the circumferential and longitudinal directions were maintained with growth ($p>0.2$, Figure 4.10). The effect of preconditioning on the circumferential sample dimension was significantly heterogeneous. The change in the circumferential dimension was much larger in medial samples compared to the posterior ones ($p<0.006$). The preconditioning resulted in a much larger stretch

in the circumferential, 1.07±0.01, than the longitudinal direction, 1.012±0.003, in the anterior and medial locations (p<0.001) while it did not show any significant directional dependency for posterior and lateral samples (1.03±0.03, p>0.07).

The degree of change in sample dimensions due to the seven-protocol biaxial testing in any given direction was not significantly heterogeneous (p>0.2, Figure 4.10). The biaxial testing had a substantially smaller effect on the sample dimensions than the first ten preconditioning cycles, resulting only in a mean stretch of 1.019±0.002 in the circumferential and 1.006±0.002 in the longitudinal directions after the initial preconditioning, indicating that the tissues were not damaged during testing. The directional-dependency of the specimen deformation due to biaxial testing and its significant spatial variability in the juvenile group were consistent with the preconditioning deformation patterns. The small change in the free-float circumferential dimension as a result of biaxial testing became even significantly less in the adult group in all four regions with larger decrease in the medial and anterior walls (p<0.005).

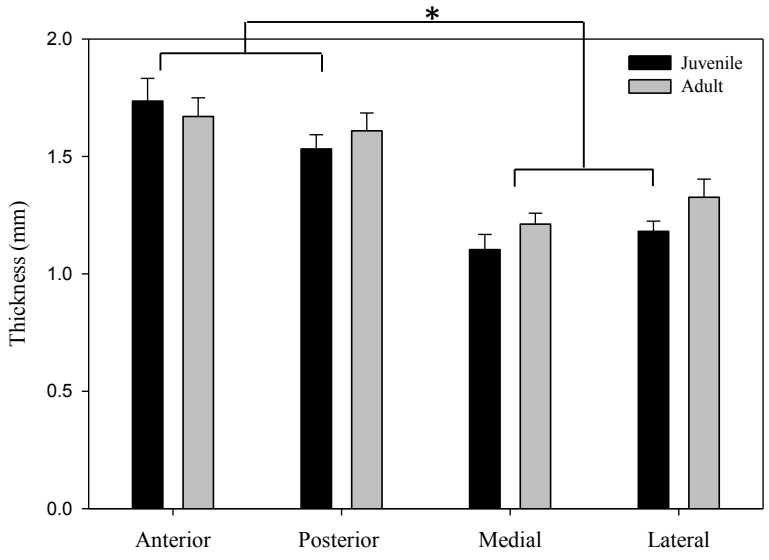

Figure 4.8. Thicknesses (mm) of excised specimens of adult and juvenile PA.
Anterior and Posterior samples were consistently thicker than the medial and lateral samples (p<0.006). The thickness of PA wall was maintained with growth in all regions.

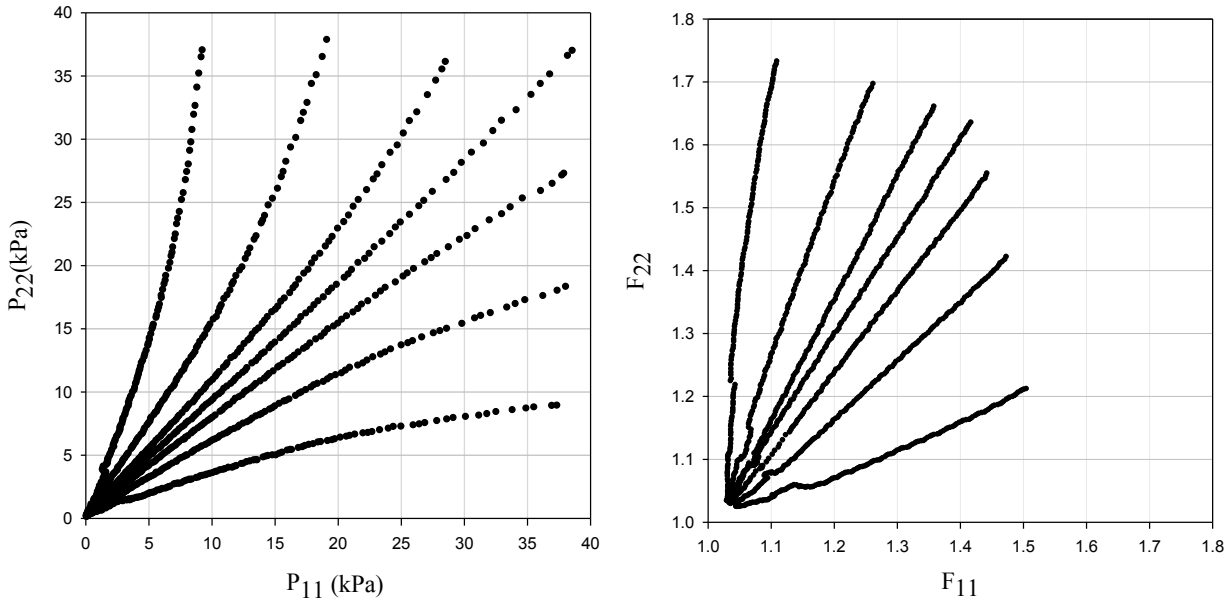

Figure 4.9. Representative seven-protocol biaxial circumferential and longitudinal stress (P_{11} and P_{22}) data (left) and corresponding measured deformations (right).

The biaxial loading paths of the PA wall samples were nonlinear. However, A prominent toe region similar to that of heart valves [64] and other arterial tissues [139] was not present (Figure 4.11). The circumferential direction was consistently stiffer than the longitudinal direction in all regions except the posterior wall, where the biaxial behavior was nearly isotropic in both age groups (p>1.0, Figure 4.11 and Figure 4.12). The compliance in the circumferential direction was not spatially variable in the juvenile stage (p>0.07) while it became slightly more heterogeneous towards the adult stage with the medial wall significantly stiffer circumferentially than the lateral wall (p<0.04, r=0.63). The longitudinal compliance of the lateral wall considerably increased with growth (p<0.01, r=0.57, Figure 4.12). In the juvenile stage, the anterior and medial regions exhibited a similarly larger degree of anisotropy than the posterior wall (p<0.02) while posterior and lateral walls were not significantly different in their biaxial behavior (p>0.8), based on the comparison of their maximum longitudinal-to-circumferential

stretch ratio (Figure 4.13). The anisotropy of medial wall increased substantially during postnatal growth (p<0.006, r=0.64) while it was relatively maintained in the other regions (Figure 4.13).

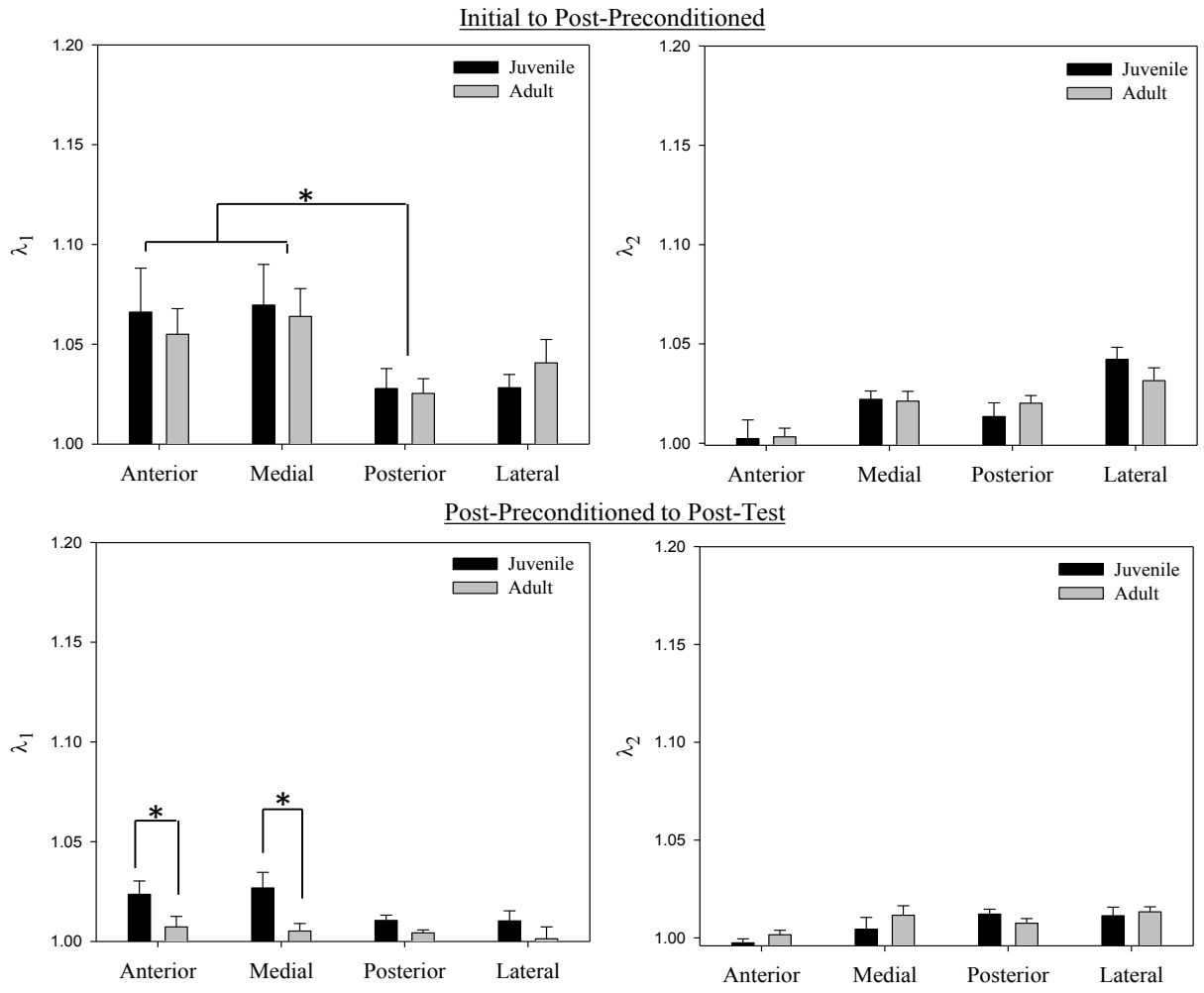

Figure 4.10. Change in load-free dimensions of samples due to preconditioning and seven-protocol biaxial testing. Change in circumferential λ_1 and longitudinal λ_2 dimensions both due to preconditioning (top) and biaxial testing (bottom) was not significantly heterogeneous (p>0.2). Preconditioning changed circumferential dimension significantly more than the longitudinal one in both age groups and biaxial testing had the same effect in the juvenile group in anterior and medial locations (p<0.03).

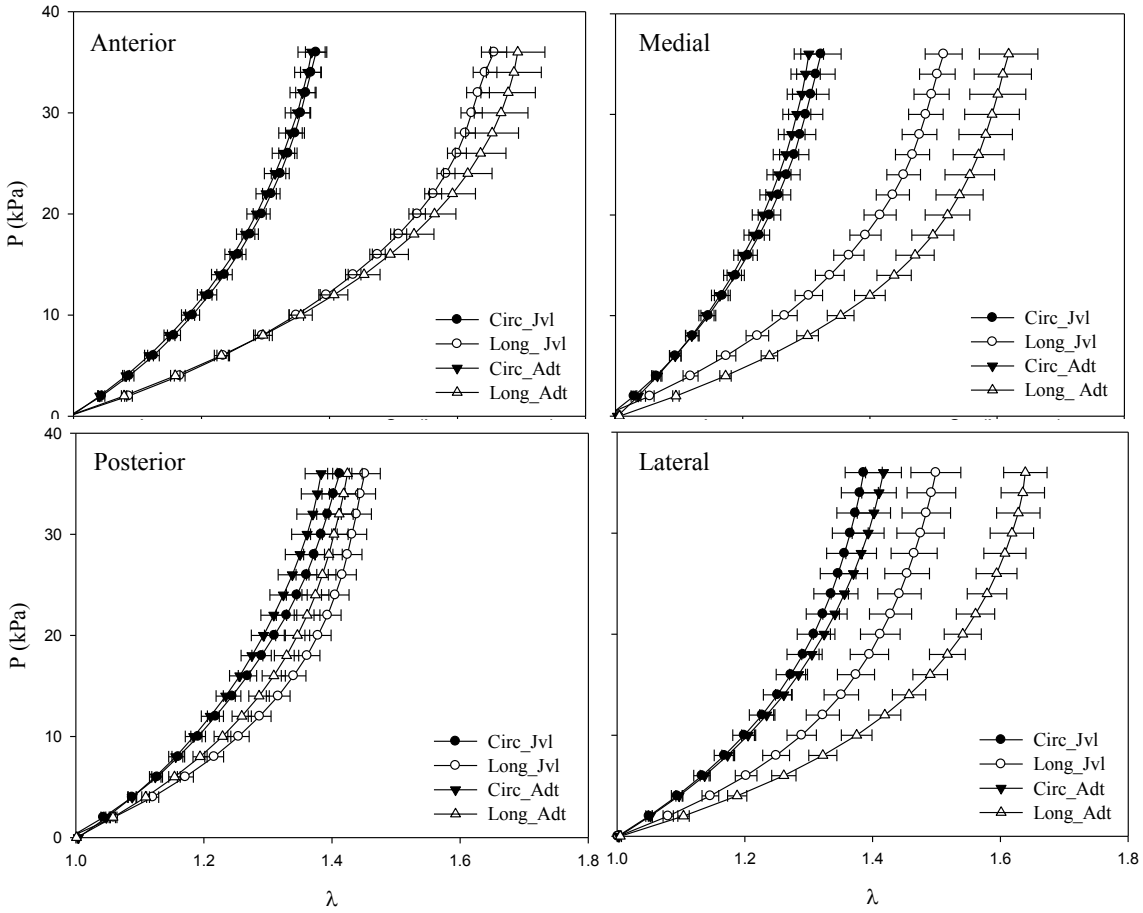

Figure 4.11. Circumferential (filled symbols) and longitudinal (hollow symbols) equibiaxial stress loading paths in the given four regions of juvenile (circles) and adult (triangles) PA wall.
Biaxial loading paths were nonlinear; all regions were circumferentially stiffer than longitudinally except the posterior wall, where the biaxial behavior was nearly isotropic in both age groups.

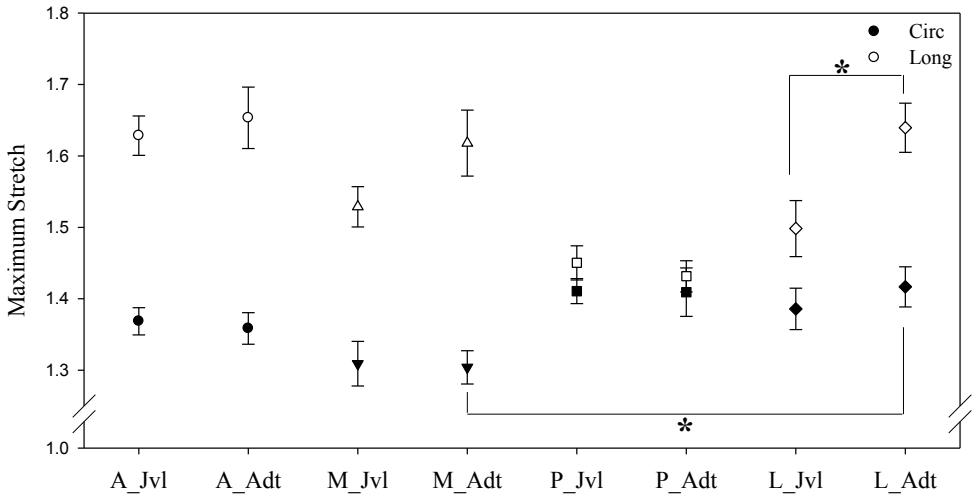

Figure 4.12. Regional growth changes in circumferential and longitudinal compliance of PA wall.
Maximum Circumferential (filled symbols) and longitudinal (hollow symbols) stretch of equibiaxial stress protocol of PA anterior (A), medial (M), posterior (P) and lateral (L) regions shown in juvenile (Jvl) and adult (Adt) groups. Circumferential compliance was relatively homogeneous at juvenile stage ($p>0.07$) while it became heterogeneous towards the adult stage with the medial wall circumferentially stiffer than the lateral wall ($p<0.04$, $r=0.63$); lateral wall became considerably more longitudinally compliant with growth ($p<0.01$, $r=0.57$).

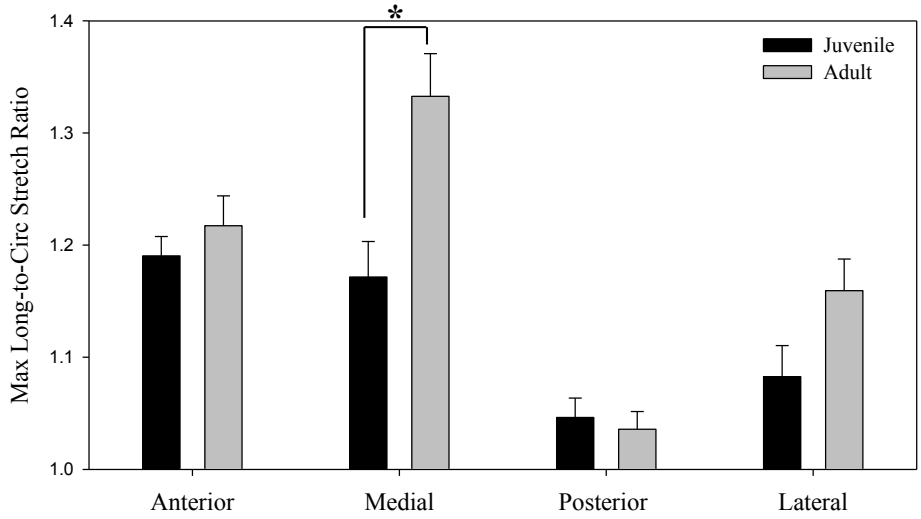

Figure 4.13. Regional growth changes in anisotropy of PA wall.
Ratio of maximum longitudinal to circumferential stretch of equibiaxial stress protocol in four regions of PA with growth: anisotropy of medial wall increased substantially during postnatal growth ($p<0.006$, $r=0.64$) while it was relatively maintained in the other regions.

4.2.2 Residual Strain

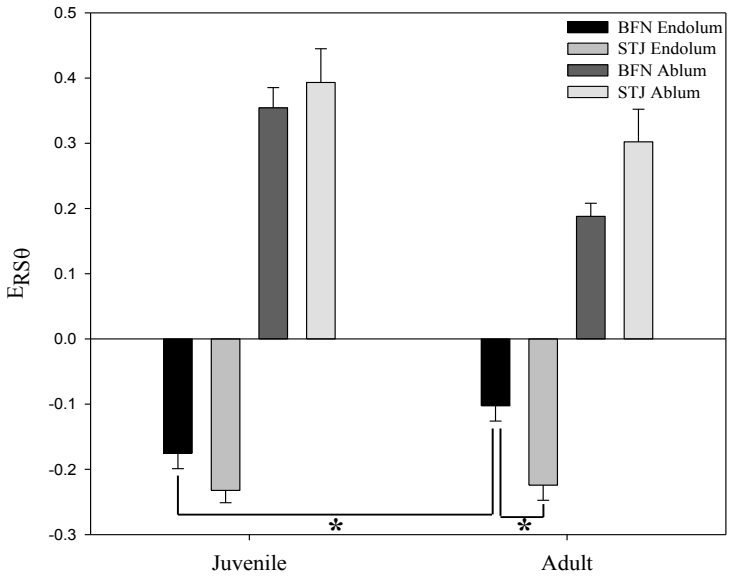

Figure 4.14. Circumferential residual strain of endoluminal and abluminal surfaces in juvenile and adult ovine. Larger residual strain values were measured on abluminal surface than endoluminal surface in both age groups (p<0.001); BFN residual strain decreased considerably over time (p<0.02, r=0.5) while it was maintained at STJ.

The internal diameter of the PA increased by approximately 1.4 times on average based on the measurements of the load-free ring specimens. The abluminal circumferential residual strain was consistently larger compared to the endoluminal surface (p<0.001, Figure 4.14). In the juvenile stage, the respective endoluminal and abluminal residual strains of -0.23±0.02 and 0.39±0.05 at the STJ decreased to -0.18±0.02 and 0.35±0.03, respectively, at the BFN. However, this distal decrease in residual strain was not significant in the juvenile group (p>0.06). While the STJ residual strain was relatively preserved with growth (p>1), it did significantly decrease at the BFN from juvenile to adult stage. This decline in amount of residual strain at the BFN with growth occurred both at the endoluminal surface, falling from -0.18±0.02 to -0.10±0.02, and at the abluminal surface, from 0.35±0.03 to 0.19±0.02 (p<0.02, r=0.5). This finding was further

confirmed by the adult group's considerably smaller residual strain at the BFN compared to the STJ, with residual strains of -0.22±0.02 and 0.30±0.05 at endoluminal and abluminal surfaces, respectively, (p<0.01, r=0.6).

4.3 DISCUSSION

The study of the changes in arterial geometry and mechanical properties at their zero-stress and no-load states and relating these to arterial histology are critical steps toward understanding the underlying mechanism of variations in arterial *in vivo* mechanical behavior due to vascular growth and remodeling. The regional mechanical behavior of the aorta and its postnatal growth adaptations have been investigated in several previous studies [53-55, 61, 140, 141]. While there have been a few studies of pulmonary artery mechanics [63, 142-144], there have not been any other rigorous investigation of the regional pulmonary arterial mechanical behavior as a function of growth. In this chapter, the regional mechanical properties of the porcine PA and AA were initially studied to understand the uniqueness of the PA mechanical behavior. Subsequently, the regional mechanical properties of the ovine PA were characterized guided by the previously quantified alterations in local surface geometry during postnatal growth.

4.3.1 Biaxial Behavior of Porcine PA and AA

The results of this study demonstrated that the PA and AA had significantly different mechanical behavior under their respective physiological stresses. As expected, the circumferential direction was stiffer in both arteries. The PA retained its loading history while the biaxial behavior of the

AA was not dependent on the previous loading regiment. This finding suggests that PA has more viscous properties than the AA. Cox [145] claimed that smooth muscle cells are contributors to viscous properties in the canine pulmonary arteries. Wells et al. [60] reported that changes in arterial viscosity during postnatal maturation closely followed changes in the relative smooth muscle cell content in the ovine thoracic aorta. Therefore, the expected relative smooth muscle cell content of the PA should be considerably more than that of the AA.

Although the AA maximum physiological stress was about 2.7 times larger than that of the PA, their mean peak strains were very similar in circumferential direction and nearly identical in longitudinal direction. This phenomenon could be achieved due to the AA's substantially larger stiffness; on average it had 3.2 times larger circumferential and 1.4-2.7 times larger longitudinal tangent modulus when compared to the PA. This finding suggests that the mechanical driver behind the structural differences between these arteries is preservation of an optimal homeostatic deformation, rather than stress. The study by Guo and Kassab [54] supports the same deformation-driven mechanism behind postnatal growth and remodeling in the aorta.

It was also demonstrated that mechanical behavior of both arteries was considerably heterogeneous. The PA's nearly isotropic behavior in the central region of the medial wall can be justified because of larger axial curvature in that region compared to the lateral wall. However, finite element analysis should be undertaken to fully elucidate the underlying cause of regional variations in mechanical behavior.

Therefore, it was established that biaxial properties of the PA are unique and very distinct from that of the AA. In the Ross procedure, the pulmonary root is used to replace the malfunctioning aortic root. The pulmonary root, which normally functions within the low pressure pulmonary system, must swiftly adapt to the systemic pressure. The subsequent

increases in wall stress lead to remodeling and autograft dilation that can cause aortic insufficiency or aneurysm formation requiring reoperation [146, 147]. The differences in mechanical behavior of these two arteries as elucidated in this study are important for understanding differences in stiffness and wall stress before the Ross procedure.

All the tissue-engineering research to date in large arteries has been focused on the pulmonary arterial replacement due to challenges with the higher physiological demands of the aortic environment [29, 30, 50, 148]. The engineering of the tissue conduit replacement of the diseased or malfunctioning aorta is necessary in congenital heart diseases, congenital connective tissue disorders such as Marfan's syndrome, or in cases of rupture-prone atherosclerotic aneurysm formation [149]. The tissue conduit replacement of the aorta requires adjusting the tissue-engineering approach for the pulmonary artery to ensure survival of the conduit in the systemic environment. The knowledge of biomechanical differences of these two arteries can inform the modifications to the tissue-engineering methodology used for the pulmonary conduit replacement.

4.3.2 Biomechanical Properties of PA during Postnatal Growth

The normal growth process resulted in complex modifications in mechanical behavior of the PA. The summaries of results along with their implications are outlined in the following sections.

4.3.2.1 Geometry

The regional thickness of the PA wall was significantly heterogeneous. The anterior and posterior walls were much thicker than the medial and lateral locations implying the existence of larger wall tension during the cardiac cycle in those regions according to the homogeneity of

stress hypothesis. There was no measured increase in wall thickness and no significant change in its spatial variation with growth denoting increased hoop and axial stress, based on Laplace's law. Due to an average of 1.4 times increase in diameter, thus, a significant increase in diameter-to-thickness ratio with growth, in absence of any measured change in physiological blood pressure, the hoop stress in the PA wall rises by about 40% with growth.

4.3.2.2 Biaxial mechanical behavior

The PA wall was circumferentially stiffer in both age groups implying a more dominant circumferential fiber orientation. Previous studies of the PA biaxial behavior in other animals report similar directional properties [143]. The PA wall exhibited an average of 40% circumferential and 40-60% longitudinal strains under equibiaxial stress. The large circumferential and longitudinal extensibility of the PA wall is of great significance since during cardiac systole about one-third of the heart's stroke volume can be stored in the PA alone leading to significant attenuation of blood flow pulsatility in the rest of the pulmonary system [150]. The loss of arterial compliance is a predictor of cardiovascular mortality. In pediatric congenital heart disease and hypoxia-induced pulmonary hypertension, for example, the extent of decrease in pulmonary artery compliance is an indicator of disease progression [47, 144, 151, 152].

Longitudinal compliance, particularly in the juvenile group, was substantially more variable than the circumferential behavior amongst the four regions studied. The heterogeneity in the longitudinal stiffness resulted in nearly isotropic behavior on the posterior wall and a significant degree of anisotropy of the anterior wall. The heterogeneity in biaxial behavior correlated with the degree of discrepancy between circumferential and longitudinal curvatures in a given region. The posterior aspect of the PA wall has larger axial curvature compared to the anterior aspect, and thus, the isotropic behavior of the posterior wall specimens can be attributed

to more similar curvatures in the circumferential and longitudinal directions of the posterior wall in the *in situ* configuration.

The biaxial behavior of the medial and lateral walls was modified with growth while that of the anterior and posterior walls was unchanged. The circumferential growth deformation patterns, as reported in Chapter 3.0, were also substantially altered in the same medial and lateral regions. Although circumferential growth seems to have been restricted in the lateral location, the circumferential stiffness was not affected in that region while the longitudinal compliance considerably increased with growth. The medial region exhibited significantly larger degree of anisotropy in the adult group with larger longitudinal compliance and, to a lesser degree, a larger circumferential stiffness, noting that neither of these directional changes was individually statistically significant. These findings support the assumption made in the first specific aim that the computed growth deformation patterns were due to change in the vessel surface geometry and not due to modification in the mechanical behavior.

The spatial variation and possible increase in the regional *in vivo* axial pre-stretch with growth in medial and lateral aspects of the PA due to modifications in surface geometry can play a possible role in measured changes in longitudinal compliance. The changes in circumferential and longitudinal curvatures in these regions with growth are plausible drivers for the significant alterations in directional mechanical properties. However, further analysis utilizing finite element methodology is necessary to investigate the underlying cause of these measured alterations in the regional mechanical behavior with growth.

4.3.3 Residual Strain Patterns

It is now well established that the vascular system contains residual strain in the no-load state. This effect can be revealed by making a radial cut in a ring tissue. It has been demonstrated that this mechanism generates non-uniform pre-stress transmurally in the vessel wall, thus reducing the concentration of the circumferential stress at the inner wall at normal physiological pressure [1, 66, 68]. The study of the change in the zero-stress state is of a unique significance because the zero-stress is the only state at which cells and extracellular matrix are at natural shape. The residual strain patterns along the PA wall have been described in previous studies [153-155], but the alteration in this pattern with growth has not been previously reported.

The measured residual strain values during the postnatal maturation period were considerably heterogeneous and became more nonuniform with growth. The abluminal $E_{RS\theta}$ was substantially larger than that of the endoluminal surface. Although the transmural distribution of $E_{RS\theta}$ was not quantified, this observation is an indication that the neutral bending axis is located proximally (near the endoluminal surface), indicating that the medial layer is stiffer, hence, more mechanically significant than the adventitial layer [156]. Since the change in the abluminal residual strain between the two age groups was consistent with that of the endoluminal surface, the position of the neutral bending axis is probably relatively maintained with growth.

There was an average of about 24% circumferential residual stain present at the endoluminal surface in the juvenile stage that fell to approximately 16% in the adult stage. The residual strain was relatively maintained at the STJ while it significantly decreased at the BFN, implying that the PA wall remodels toward BFN while it maintains its structure near the right ventricular outflow region. As demonstrated in the previous chapter, the PA tapers distally with

growth. This decrease in diameter at BFN and drop in hoop stress in that region may be a correlate to the decrease in residual strain.

The remodeling of the vessel wall in a disease condition such as hypertension or during the normal maturation process results in change of the zero-stress state due to the nonuniform growth in different parts of the vessel [1, 157]. Fung and Liu [154] studied the effect of hypoxia-induced hypertension on the zero-stress state of the rat pulmonary artery. In this study they state that tissue growth is induced by growth factor and other physical, chemical, and biological factors. They claim that physical stress, if shown to influence growth, should also cause tissue remodeling under hypertension because of the direct relationship between blood pressure and physical stress. Since it was shown in the current study that the PA diameter-to-thickness ratio increased with growth, the wall stress should have increased. However, while the nonuniform wall stress distribution in the adult arterial wall was provided as a basis for heterogeneity of residual strain, the same reasoning cannot explain the relative preservation of residual strain at the STJ with growth in presence of larger wall stress in the adult PA. Therefore, further analysis is required to elucidate the driving mechanism behind remodeling of the PA wall during the normal growth process.

5.0 REGIONAL STRUCTURAL CHARACTERIZATION

The objective of this chapter was to determine the structural correlates to the mechanical properties reported in the previous chapter by delineating the spatial variation of the PA wall structure during the postnatal maturation as outlined in the second specific aim (sections 1.3.3 and 1.7). The gross anatomy of arterial wall structure was studied and the regional thicknesses of the major arterial layers were measured. The multiphoton microscopy (MPM) technique was utilized to obtain high quality images of collagen and elastin microstructure. The elastin structure was accurately quantified, and the mean fiber orientation and degree of fiber scattering were calculated in the four designated regions of the PA wall with growth. The sizes of all three arterial layers were maintained with growth. The elastin fiber network exhibited clear directionality and was heterogeneous correlating with the mechanical properties. The change in elastin organization of lateral wall corresponded with the postnatal alteration in its mechanical behavior. The elastin structure of the medial wall did not change to a significant extent with growth. Therefore, further study is required to elucidate the structural remodeling mechanism underlying the regional modification in mechanical behavior of the medial wall during postnatal growth.

5.1 BACKGROUND

The collagen and elastin gross fiber orientation have been acquired in fixed tissues using small angle light scattering (SALS) technique [158]. This technique has been used along with mechanical testing to directly analyze the fiber kinematics during biaxial loading [94, 159]. One of the major limitations of the SALS technique is that only gross tissue microstructure can be determined: elastin and collagen fibers are not distinguished. Further, only average transmural architectural information can be obtained unless the tissue is sectioned, SALS performed on each section and subsequently the SALS data of the sections is reconstructed into a 3D configuration the get the gross architecture of the tissue [160]. Finally, the three-dimensional trajectory of fibers cannot be visualized through the SALS technique. The last two limitations are particularly significant for the study presented in the next chapter on quantification of collagen recruitment behavior.

Multiphoton excitation microscopy (MPM) based on the simultaneous absorption of two or more near infrared photons has become a powerful technique for the artifact-free, nondestructive and high-resolution visualization of the fibrillar components of the extracellular matrix such as collagen and elastin in their native environment [161-163]. The non-linear process called second harmonic generation (SHG) enables visualization of collagen fibers with submicron resolution without the need for tissue processing. In SHG, multiple photons simultaneously interact with non-centrosymmetric molecular assemblies of fibrillar collagen producing radiation at exactly half of the excitation wavelength [164]. The 3D autofluorescence imaging of the elastic fiber is achieved through two-photon excitation autofluorescence (TPEF) microscopy. In the conventional confocal laser scanning fluorescence microscopy absorption of a single photon supplied adequate energy for the fluorophore to reach the excited state from which

it returns to the ground state by producing a photon of fluorescence [165]. In TPEF, the fluorophore excitation is achieved by the near simultaneous absorption of two longer wavelength photons. TPEF and SHG signals can be excited and detected simultaneously provided that two detection channels are present on the microscope. Usually, SHG signal travels in the same direction as the incident light and isotropic TPEF is detected in the backward direction. In this work, MPM imaging of collagen and elastin is performed on stress-free arterial segments.

5.2 METHODS

After biaxial testing, samples were placed in freshly prepared 2% paraformaldehyde solution and refrigerated at 4°C overnight. Subsequently, one circumferential strip was cut from each sample for transverse sectioning for visualization of the arterial layer structure, and the remaining specimen was left for enface sectioning to quantify the collagen and elastin fiber content and orientation. The fixed samples were paraffin-embedded; the strip samples were each cut transversely into 5-μm thick sections for histological staining, and the enface sectioning was performed at a 50-μm slice thickness for multiphoton imaging. The Verhoeff-Van Gieson stain for elastin was applied to strip section for clear identification of arterial layer structure. Different arterial layers were visually identified and their thicknesses manually measured using ImageJ software.

5.2.1 Multiphoton Microscopy

The Olympus FV1000 MPM system consisted of a mode-locked Ti: Sapphire laser (Chameleon Vision, Coherent, Santa Clara, CA) and an Olympus upright optical microscope. The average excitation power at the sample was approximately 40mW with an excitation wavelength of 830 nm and about 10% laser transmissivity. The tissue was line-scanned, and TPEF and SHG signals were captured by two nondescanned external photomultiplier tube detectors coupled to the longpass dichroic mirrors and bandpass emission filters. The emission wavelengths was set to 400±100 nm for second harmonic generation signal of collagen, and the second channel was set at 525±50 nm for elastin fluorescence. Time-lapse images were acquired using Fluoview software (Olympus). Using a 25X water-immersion objective, XY scans (508 × 508 μm; 0.497 μm/pixel resolution) were performed at 2 μsec/pixel. Depending on the section quality either an image stack or a single XY scan was acquired of each slide from the sectioned tissue samples.

5.2.2 Structural Quantification

The MPM technique was used to obtain collagen and elastin signals of three enface sections of medial layer of each biaxial specimen (n=5 per location per age group), with one section proximal to intima, one in the central region, and one proximal to the adventitia. The MPM images of adventitial sections of randomly selected biaxial specimens (n=7) were also obtained. The elastin and collagen channels of MPM images were separated and maximum intensity z-projection of collagen and elastin image stacks were obtained using ImageJ, giving a 2D projection from the 3D stacks. The relative elastin and collagen content of each image was quantified using ImageJ color threshold tool (Appendix B).

Due to the presence of collagen fiber's crimp structure, the fiber axis could not be accurately determined. Therefore, only elastin fiber orientations were determined in the sections of tunica media based on a method originally developed by Chaudhuri et al. [166] that was implemented by Karlon et al. [167] for automated measurement of myofiber orientation and has been used to determine the distribution of fiber angle in tissue-engineered scaffolds [168]. A custom-written MATLAB program based on the aforementioned method [166] was implemented to quantify the fiber orientation distribution (Figure 5.1; Appendices C2 and C3).

Specific details of the method were given in previous publications [166, 167] and are briefly explained here. Edge detection was performed by convolving a horizontal and a vertical mask of a selected size s x s, with the image at each pixel, to give respective gradient measures G_x and G_y. The edge image was then constructed from gradient vector magnitude ($G = G_x^2 + G_y^2$) and angle ϕ ($\phi=\tan^{-1}[Gx/Gy]$). The image was then divided to m x m pixel sub-images, and the gradient magnitude G was used as the weighing function for each angle on the domain [-90^o, 90^o] at 1^o increments at each pixel in the sub-image. The summed gradient-weighted contribution for each angle in the domain was determined, and the dominant fiber orientation was identified as the maximum accumulator bin value within a sub-region. The angle values representing each bin were accumulated in a histogram to define the collagen fiber orientation distribution in the whole image. The circumferential direction in each section corresponded with 0^o angle; hence, the vessel axis was aligned with the 90^o angle. Vertical and horizontal mask sizes were 7 x 7 pixels (s = 3). Subregion size for direction vector calculation was 16 x 16 pixels. Both mean elastin fiber orientation and normalized orientation index (NOI), as a degree of orientation dispersion from the mean fiber alignment, were computed to quantify fiber structure in the PA wall.

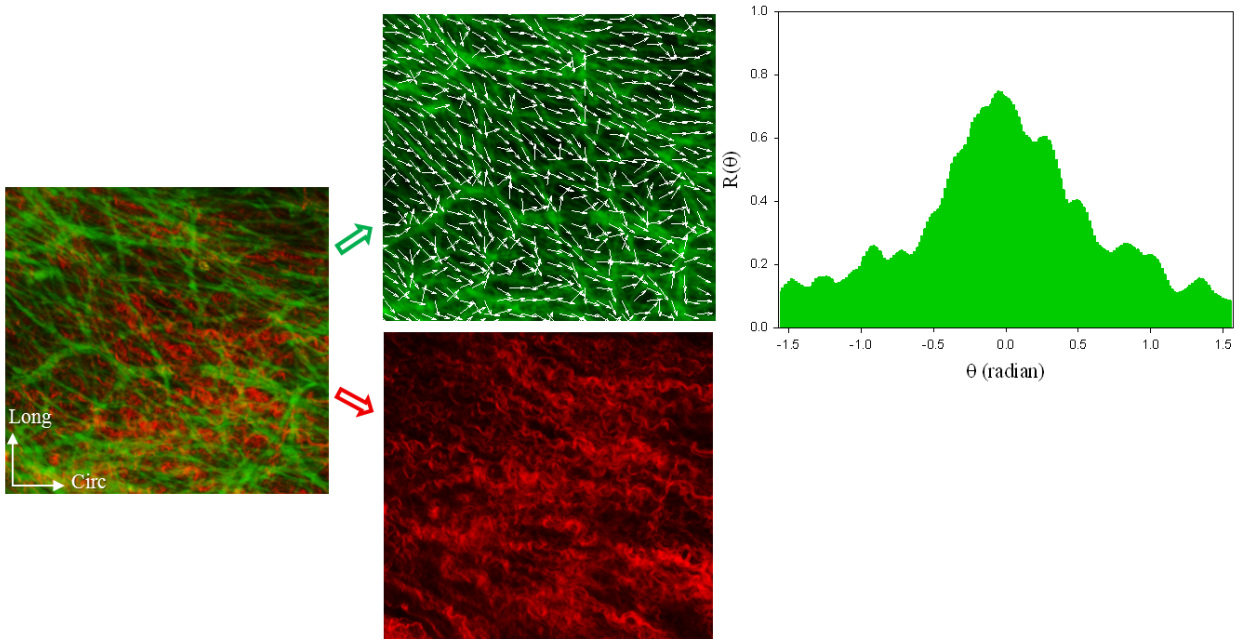

Figure 5.1. Quantification of elastin fiber network angular distribution in 2D projection of MPM images. Collagen (red) and elastin (green) of a proximal section of tunica media shown on the left with each fiber population individually displayed in middle. A depiction of orientation analysis of elastin fibers is demonstrated through superimposed regional fiber orientation vectors (white arrows) with corresponding normalized fiber orientation distribution graph on the right.

5.2.3 Statistical Analysis

A one-way ANOVA was performed to evaluate spatial variability (SPSS software). Levene's test for homogeneity of error variance was performed. The multiple post hoc comparisons were made using the Bonferroni correction when error variances were similar and the Games-Howell post-hoc adjustment was made when homogeneity of variance was violated. The independent t-test was used to assess the changes with growth in each location. A one-tailed value of $p < 0.05$ was considered statistically significant. All values are reported in terms of mean ± SEM.

5.3 RESULTS

5.3.1 Thicknesses of Arterial Layers

The regional variation of arterial layer structure was negligible in both age groups (p>0.4). The relative thickness of each layer did not significantly change with growth (p>0.08). The PA wall mostly consisted of the tunica media, occupying 81±0.8% of the wall thickness, and substantially smaller wall volume was comprised of tunica adventitia and intima, taking up 11±0.7% and 7.3±0.4% of the wall thickness, respectively (Figure 5.2).

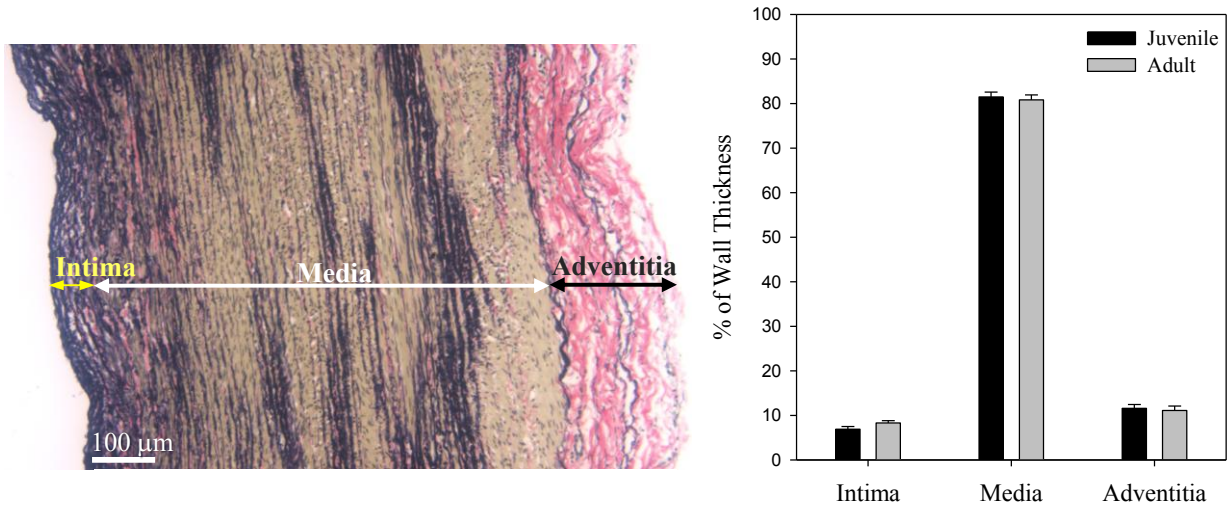

Figure 5.2. Relative thickness of each arterial layer in PA wall.
Verhoeff-Van Gieson stained transverse section of PA lateral wall sample is shown (left) with each layer labeled; the collagen is in pink, elastin is in black and smooth muscle is in brown color. The relative thickness of each layer is displayed in a bar chart (right): media is substantially thicker than the intima and adventitia.

5.3.2 Collagen and Elastin Structure

Collagen and elastin were closely associated with each other and formed laminas in the tunica intima and media. Elastin exhibited two forms: a dense network structure and a thin sheet-like structure. The elastin compact network arrangement gradually became sparse distally, moving from the intima towards the adventitia (Figure 5.3). In the tunica adventitia, collagen formed thick undulated bundles running mostly in the circumferential direction with elastin dispersed in between in the form of randomly oriented fiber strands (Figure 5.3). Uniform or very distinct internal and external elastic laminae were not present in the ovine PA wall; they mainly appeared as sparse perforated narrow sheets (Figure 5.4).

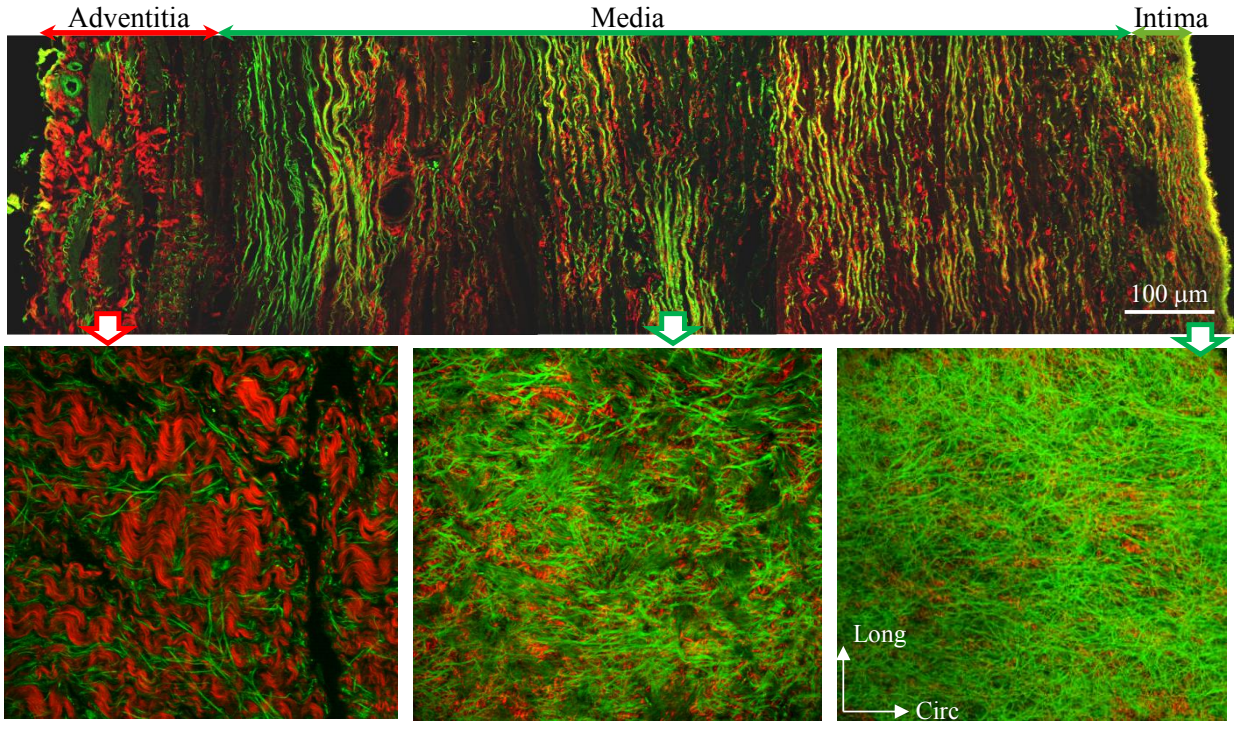

Figure 5.3. MPM images showing different layer structures of PA wall.
Montage of MPM images of a transverse section of PA anterior wall (top) with each layer labeled. MPM images of enface sections of intimal, medial and adventitial layers (bottom) displaying representative collagen (red) and elastin (green) structure and content in each layer: Collagen was relatively thin and had fine crimp structure in media and formed into thicker fiber bundles in adventitia; relative elastin content of media (62±1%) was significantly larger than collagen while collagen was dominant fiber in adventitia (63±2%).

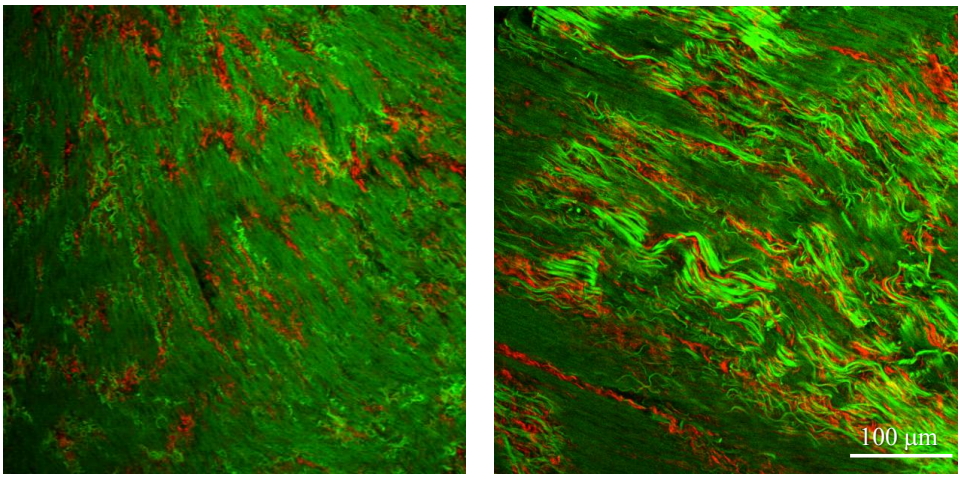

Figure 5.4. MPM images of internal (left) and external (right) elastic lamina-like structures (green) of ovine PA wall.

There was not a significant alteration in the relative collagen and elastin content of the tunica media spatially and with growth (p>0.3). The collagen area fraction was measured to be 38±1% (Elastin: 62±1%) in the tunica media and 63±2% (Elastin: 37±2%) in the tunica adventitia.

There was no significant transmural variation in elastin fiber orientation distribution based on the mean fiber orientation and NOI (p>0.4). The elastin fiber structure was considerably heterogeneous and was nonuniformly altered with growth. The mean elastin fiber orientation and the NOI of anterior and posterior walls did not change with growth (p>0.1). The mean fiber orientation values indicated that elastin fibers were considerably more circumferentially aligned on the anterior aspect of the PA wall, 0±5 degrees, compared to the posterior aspect, 30±8 degrees (p<0.005) (Figure 5.5). However, according to the NOI quantities, the degree of fiber alignment of anterior wall, 38±3%, was not significantly different from that of the posterior wall, 44±3% (p>0.1).

The elastin fibers' mean orientation in the medial wall was similar to that of the anterior wall and seemed to become more circumferentially aligned with growth, changing from 7±7 to

2±3 degrees. However, this change in fiber orientation did not prove to be significant (p=0.07). The degree of fiber dispersion 49±2% was maintained in the medial wall (p>0.1) and was relatively less than the anterior wall (p=0.02). The significant change in fiber structure with growth was measured in the later wall where elastin fibers became considerably more circumferentially aligned, with the mean fiber orientation changing from 23±6 to 1±7 degrees (p=0.006), from juvenile to adult stage. The NOI of lateral wall elastin fibers significantly decreased from 60±3% to 46±4% (p=0.01) revealing an increase in degree of fiber scattering. This change in elastin fiber structure resulted in significant variation in the mean fiber orientation from that of the posterior wall, and while the NOI of lateral wall was significantly larger than rest of the PA wall in the juvenile group (p<0.01), it became fairly uniform in the adult stage.

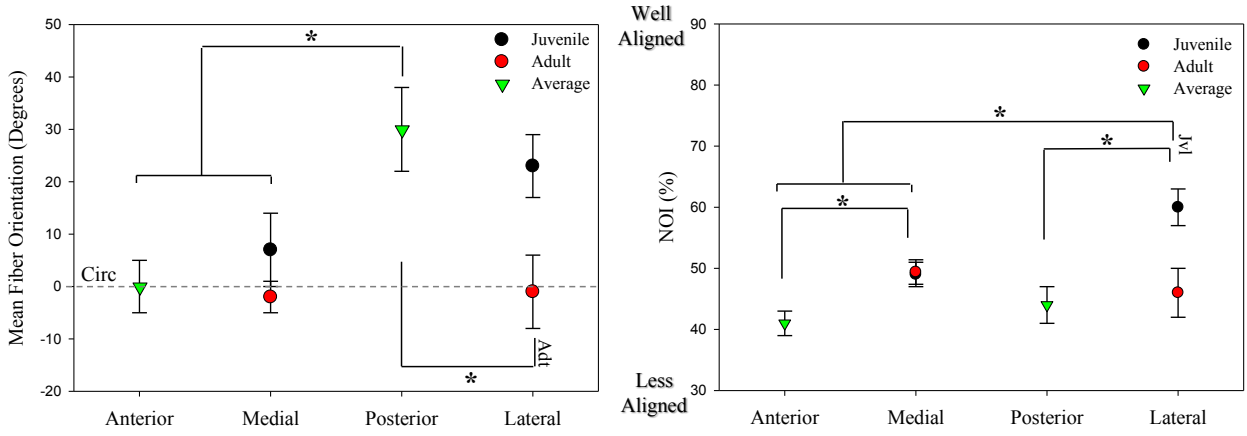

Figure 5.5. Regional variation of elastin mean fiber orientation and NOI of PA wall with growth. Average mean fiber orientation and NOI of both age groups reported for anterior and posterior regions as no significant alterations in elastin fiber structure was measured at these locations with growth (p>0.4). Elastin organization in medial wall did not change significantly with growth (p>0.07). Anterior and medial wall elastin fiber alignment was significantly closer to circumferential direction than posterior wall (p<0.001). Degree of fiber dispersion of medial wall was less than anterior region (p=0.02). NOI of lateral wall was less than other regions in juvenile stage (p<0.01). In lateral wall, significant increase in circumferential mean orientation of elastin fibers with growth (from 23±6 to 1±7 degrees) (p=0.006) was associated with significant drop in NOI from 60±3% to 46±4% (p=0.01). In adult group, other than the posterior wall, the mean fiber orientation was in circumferential direction.

5.4 DISCUSSION

Collagen types I and III, protein molecules with great tensile strength, and elastin, a heavily cross-linked, rubbery protein, determine the proper form and function of the artery wall and essentially regulate its physical and mechanical properties [169]. Elastin and collagen are the critical scleroproteins in larger arteries since they render the arterial wall its large distensibility and recoil property that enables relatively continuous blood flow from the heart to the rest of the body with little change in pressure.

The development of the circulatory system implicates the deposition and remodeling of these structural proteins. The studies of collagen and elastin synthesis in the developing aorta and pulmonary artery has revealed that they undergo a relatively rapid and dramatic series of biochemical and morphologic alterations during the perinatal period as a preparation for postnatal increase in arterial pressure [50, 71, 170].

Although collagen molecules are probably slowly replaced during adult life, studies of elastin turnover indicate that vertebrates depend on the elastin molecules synthesized in early development to function throughout life [72]. Inherited or acquired disorders in the synthesis, processing, or remodeling of these proteins lead to major disruption of the arterial function, such as in hypertension [171-174].

The goal of this study was to understand the role of collagen and elastin organization and content in remodeling of the PA wall and correlating these changes with the alterations in mechanical behavior during postnatal maturation. This information is valuable to unraveling the primary mechanisms of vascular remodeling and developing advanced mechanobiological constitutive models that integrate quantitative information of vascular biology, structure, and biomechanics.

In Chapter 4.0, it was demonstrated that the thickness of the PA wall does not increase with growth implying that there would be an average 40% increase in hoop stress due to an equivalent increase in diameter. The tunica media is considered to be the most mechanically significant arterial layer as measured to occupy the major part of the PA wall. However, despite the inferred rise in the hoop stress, the thickness of this layer was maintained with growth. Therefore, the change in size of tunica media is not part of the adaptive response to change in wall stress during postnatal growth. The relative thickness of this arterial layer was also maintained in the four designated regions at a given growth stage.

The quantified elastin content of the tunica media was significantly larger than its collagen content indicating that elastin is the more dominant structural protein in the PA wall. The absence of a toe region in the stress-strain loading path, as demonstrated in the previous chapter, confirms that elastin response [175] overrides the collagen mechanical contribution, particularly in the low-load zone. This claim will be addressed in Chapter 6.0. This result implies that elastin can play a significant role in modifying the mechanical behavior of the arterial wall in many disease processes such as in hypertension [176, 177]. It was also revealed that the elastin and collagen concentration of the PA wall was not modified with growth, eliminating the theory of upsurge of elastin and collagen synthesis as a mechanistic response to the change in wall stress during normal postnatal growth process.

The elastin structure of the PA wall was quantified and the mean fiber orientation and NOI, degree of fiber alignment, was measured. In many previous constitutive models of the arterial wall, elastin contribution has been represented by neoHookean or other isotropic models [86, 178]. However, current results demonstrated that the elastin fiber network had a distinct alignment with a moderate degree of dispersion, implying that mechanical behavior of the PA

elastin network is direction-dependent as demonstrated in a few recent studies of aortic elastin [179, 180].

The heterogeneity in the mechanical behavior of the PA wall was comparable with the spatial variation in the elastin structure. For example, the elastin fibers in the medial and anterior walls were more circumferentially aligned than the posterior wall correlating with the substantially larger anisotropy of former regions compared to the latter, where the organization of the elastin fiber network was for the most part maintained with growth. A significant alteration in elastin structure was measured on the lateral wall, where the mean fiber alignment became nearly circumferential while the fiber orientation dispersion increased as revealed by the drop in the NOI. Thus, the increase in longitudinal compliance of the lateral wall can be explained by change in the mean fiber orientation towards the circumferential direction.

On average, the elastin fibers became more circumferentially aligned in the medial wall in the adult group compared to the juvenile stage. However, the p value was not sufficiently small to irrefutably link the change in the elastin network arrangement to the substantial rise in the anisotropy of the medial wall. Therefore, further study need to be conducted to fully corroborate the change in elastin organization as the underlying structural cause of the alteration in the mechanical behavior of the medial PA wall during postnatal growth.

6.0 DIRECT MEASUREMENT OF COLLAGEN RECRUITMENT

The goal of this study, as outlined in the third specific aim (sections 1.6.2 and 1.7), was to quantify the postnatal alterations in collagen recruitment behavior using a biaxial loading device coupled with the MPM system. The 3D architecture of collagen fibers was examined and fiber trajectory path was traced in the medial aspect of the PA wall. The 2D collagen and elastin fiber orientation was measured from the summed intensity z-projection of the 3D image stacks. The collagen fibers, on average, were more aligned than elastin fibers as measured by the NOI. The measured collagen tortuosity in the stress-free state significantly increased with growth. However, the collagen fibers were recruited at an overall considerably faster rate in the adult specimens. The alteration in collagen recruitment behavior with growth is an indication of modification in collagen structural properties or a possible change in the elastin-collagen interaction. As reported in the previous chapters, the stress was not found to be the primary mechanical driver during normal growth process of the PA wall. Understanding the underlying mechanism of this change in collagen recruitment behavior during growth will help to determine the primary mechanical factors influencing the arterial wall's normal remodeling and growth process.

6.1 BACKGROUND

It has been proposed that the passive mechanical response of the arterial wall is governed by isotropic elastin fibers in the initial loading region while the crimped circumferentially-oriented medial collagen fibers gradually unfurl and begin carrying load under increasing pressure [87, 88]. In 1978, Cox [181] performed in vitro pressure-diameter measurements on several arterial types, e.g. carotid, iliac, mesenteric, etc., and also quantified the collagen and elastin content of each artery. He used the relation between the variations of the elastic moduli of different arteries with the elastin and collagen content to estimate the elastic modulus of elastin and collagen fibers. Based on the assumption of the parallel contribution of connective tissue elements, he then derived the relation between the transmural pressure and the fraction of collagen fibers supporting wall stress using the simple relation

$$E_{inc} = \Phi_{el} E_{el} + F_{col} \Phi_{col} E_{col} ,$$

where E_{inc} is the incremental elastic modulus, Φ_{el} and Φ_{col} are the percent dry weights of collagen and elastin, respectively; E_{el} and E_{col} are the elastic moduli of elastin and collagen, and F_{col} is the percent fibers supporting wall stress at a given pressure or strain.

Recently, there have been few studies on the direct quantification of the relation between the collagen engagement (recruitment behavior) and tensile loading of the arterial wall. Roy and coworkers [182] froze cylindrical rabbit carotid arteries at different circumferential stretches, and sectioned the arterial wall. They then obtained autofluorescence signals of Picro Sirius Red stained collagen fibers in each section under a confocal microscope and quantified the collagen tortuosity or straightness in each 2D confocal image.

With the advent of advanced imaging modalities such as the MPM, the 3D dynamics of collagen loading behavior of untreated or fresh tissue can now be directly measured without the confounding influence of fixation or antibody staining. Hill et al. [92] combined a uniaxial mechanical testing device with the MPM system and obtained the collagen SHG signals of fresh rabbit carotid arteries at different uniaxial stretches. Subsequently, they measured the collagen tortuosity from the 3D reconstruction of MPM image stacks at a given stretch.

As previously explained (section 1.4.1) the limitation with uniaxial testing is that it does not correspond to physiological boundary conditions of arterial wall. Therefore, in the current study, a biaxial loading device is coupled with the MPM system to quantify, for the first time, the postnatal changes in the arterial wall deformation-collagen recruitment relation in the tunica media of the fresh pulmonary arterial tissue.

6.2 METHODS

To both visualize and quantify the collagen fiber network in three dimensions under real-time equibiaxial strain deformations, biaxial testing was performed underneath the same Olympus FV1000 MPM system described in section 5.2.1. A miniaturized biaxial testing system was custom developed to fit the space constraints of the MPM system (Figure 6.1). The miniaturized biaxial testing system (microbiax) consisted of both an imaging and motion control system. For the motion control system displacement was imparted with four miniature hybrid linear actuators (HaydonKerk) that were controlled with a customized Labview program, a motion controller card, and a 4-axis stepper power drive (National Instruments).

A detailed description of the biaxial testing methods used for planar biological tissues was previously presented (section 4.1.1). A 10 mm x 10 mm specimen was dissected from the medial aspect of the juvenile (n=5) and adult (n=5) ovine PA wall (section 4.1.1.3). To expose the tunica media, the tunica intima was gently peeled off using a micro forceps and micro scissors. Most of the loose connective tissue of tunica adventitia in the center of the specimen was clipped, and four small cut portions of polypropylene suture were attached as fiducial markers to the center of the abluminal surface of the specimen. Two silk suture loops of equal length were attached to each side of the specimen with four stainless steel hooks, and the specimen was placed in the microbiax PBS bath at room temperature. The stainless steel hooks attached to each side of the specimen were coupled to the linear actuator through suture lines that looped over carriage mounts. These carriages were free to rotate to allow for equal tension in the suture lines, and thus allow for a relatively homogenous stress distribution in the specimen during testing. The specimen was mounted onto the device such that X_1 and X_2 axes of the device corresponded with circumferential and longitudinal directions of the sample (Figure 6.2).

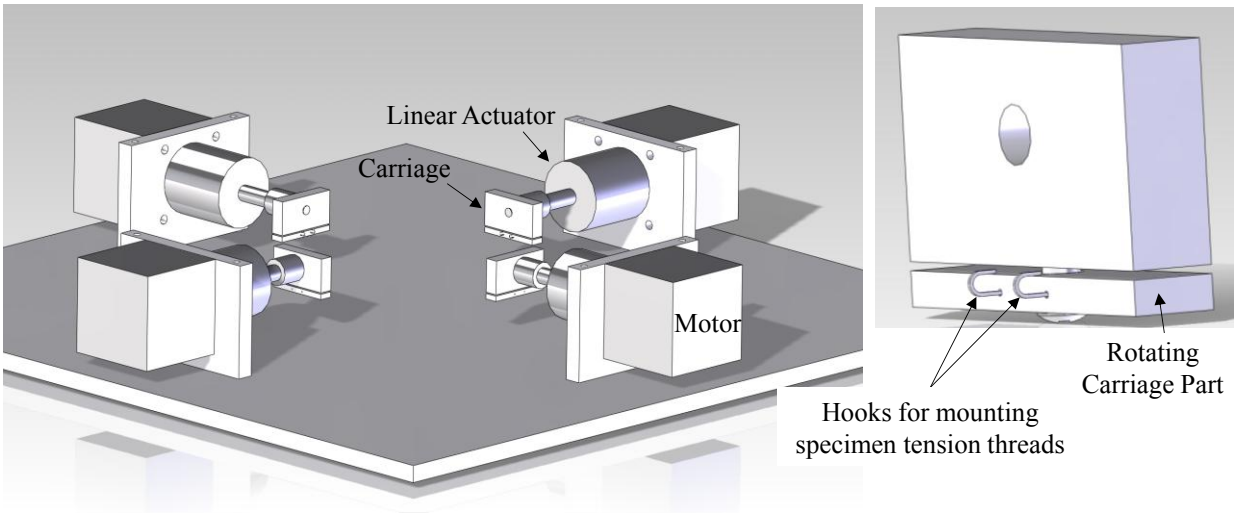

Figure 6.1. CAD diagram of microbiaxial stretching device (left) and a single carriage (right).

The fiducial markers were visualized with a mirror angled at 45 degrees that was mounted below the miniaturized biaxial test system with a transparent cast acrylic base (Figure 6.2). For the imaging system, strain was calculated real-time with a customized Labview program, and a firewire camera (Sony Inc., Tokyo, Japan) equipped with a 55 mm telecentric lens (CBC Inc., New York). The customized Labview software allowed the user to control displacement while continuously displaying the real-time strain, calculated as described in section 4.1.1.1. The specimens were taken through three equibiaxial stretch cycles of preconditioning at the rate of 0.5 mm/sec. The specimens were then taken to 50% equibiaxial stretch at 10% stretch intervals for both juvenile and adult specimens. Subsequently, the juvenile specimens were taken to 70% equibiaxial stretch. Because the first few adult specimens tore at the hooks at 70% stretch, the remaining specimens were taken up to 65% stretch. The SHG and TPEF emission signals of collagen and elastin fibers were acquired in the stress-free post-preconditioned state and at each stretch level. At each stretch level, the tissue extension was held fixed during the approximate 30 minutes of image acquisition. The excitation wavelength was chosen at 830 nm at about 11 to 13% laser transmissivity. The emission wavelengths were received by two filters: The first channel was set to 400±100nm for SHG signal of collagen, and the second channel was set at 525±50 nm for elastin TPFE signal. The sampling speed was set to 2 μs/pixel with a 2 line kalman filter, and the scanning had an incremental z-step of 0.6 μm. The maximum imaging depth reached ranged from about 70 to about 150 μm. Image stacks were imported into the Imaris software (Bitplane, Switzerland), for 3D visualization and quantitative analysis of 3D collagen fiber trajectories. Due to compaction of fibers at or below 20% stretch, the number of fibers that were accurately traceable was about 25. Thus, for each subsequent stretch level 25 fiber paths were traced.

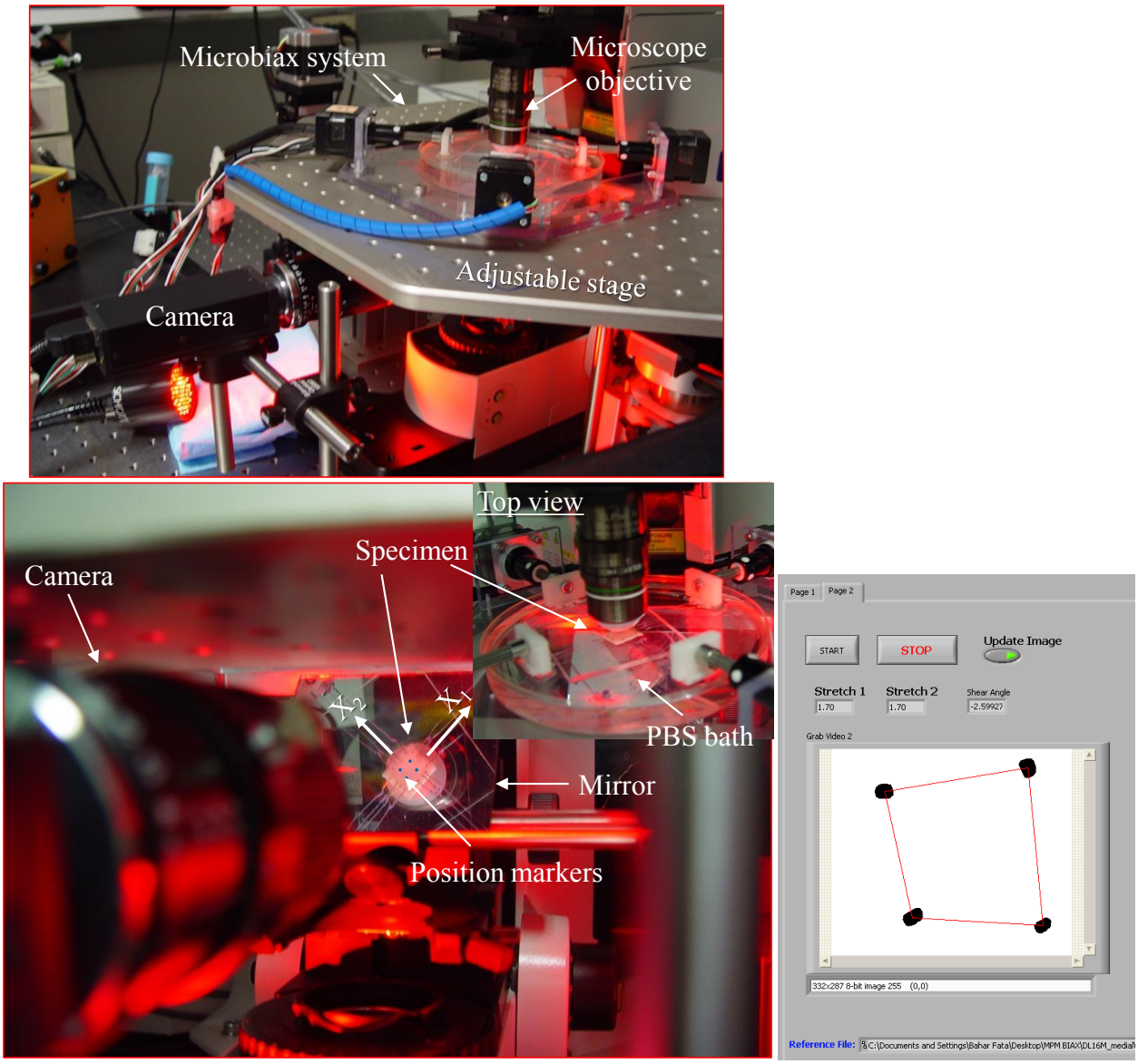

Figure 6.2. Microbiax device combined with MPM system.
Specimen's reflection in mirror captured by camera underneath the device stage (bottom). X_1 and X_2 corresponded to arterial wall specimen's circumferential and longitudinal directions; deformation along those axes was computed through tracking of fiducial markers (blue) by a Labview program (front panel shown on right).

Tortuosity was defined as the ratio of fiber-path (fiber arc) length to the chord length, $\tau = s/l$. Fiber arc length s was measured in 3D reconstructed images by using the semi-automated Filament function in Imaris (Figure 6.3). Fibers were manually selected by the operator and the fiber tracing was performed using the fast marching algorithm, which is a generalization of the

2D method described in [183]. The chord length *l* was determined based on the best fit line to the 3D fiber trace, rather than the end-to-end length, so that the chord length was not dependent upon the choice of the end points [92]. An important advantage of using the 3D renderings is that tracing of the longer fibers is much more accurate than with 2D methods, since portions of fibers that travel out of the plane, or that overlap, may be included.

The 2D elastin fiber orientations were quantified in both fully loaded and in post-preconditioned unloaded states, and collagen fiber orientation was quantified in the former state. First, summed-intensity projection of MPM image stack into X_1-X_2 plane of arterial wall was obtained (Appendix C1). The previously outlined algorithm was then implemented to quantify the orientation distribution of each fiber type (section 5.2.2; Appendices C2 and C3).

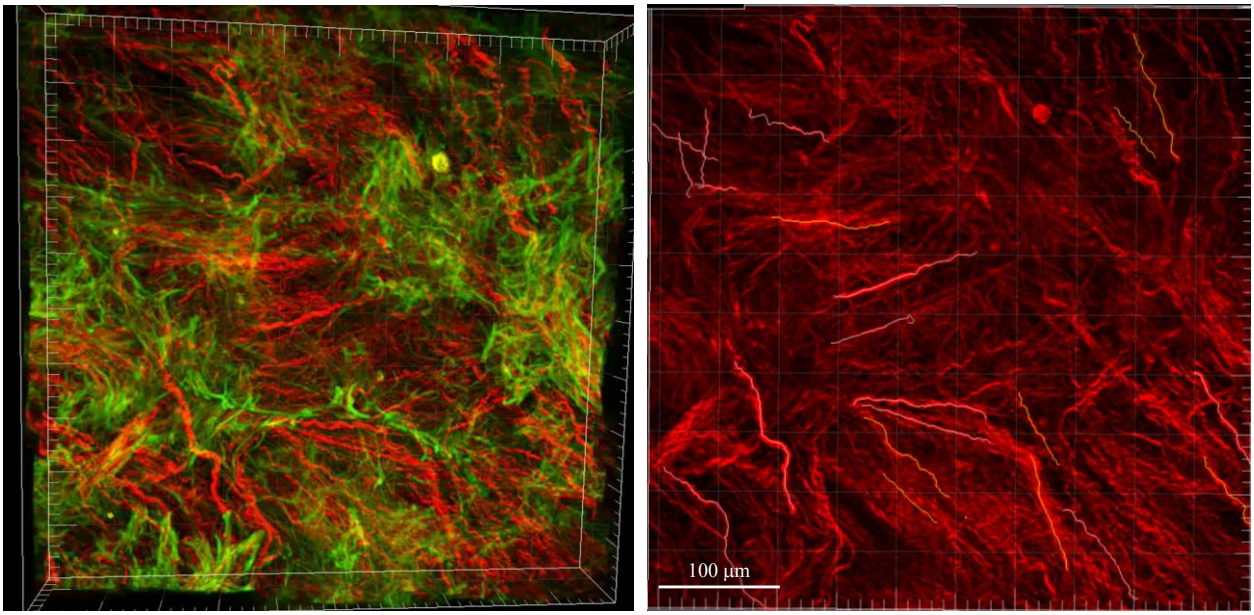

Figure 6.3. 3D reconstruction of MPM image stacks at 40% equibiaxial stretch.
3D elastin and collagen structure of a juvenile medial PA wall specimen at 40% equibiaxial stretch (left). Tracking of collagen fibers' 3D trajectory in the same image using filament tracing function of Imaris (right).

6.2.1 Statistical Analysis

The paired and independent t-test was used to assess the within group parameter of deformation level and in-between group variable of growth (SPSS software). A one-tailed value of $p < 0.05$ was considered statistically significant. All values are reported in terms of mean ± SEM.

6.3 RESULTS

The angle of the fiber best-fit line with the X_1-X_2 plane (plane of the wall) was measured in order to examine the validity of the simplification of 3D fiber paths to 2D fiber orientation distributions. The average out-of-plane fiber angle was measured to be 8.2±0.8 and 11±1 degrees in juvenile and adult groups, respectively, with no significant difference between the two groups (p=0.4). The mean orientation and NOI of both elastin network and collagen fibers were used to make comparisons of fiber orientation distribution. It was verified that the elastin orientation was mostly maintained during equibiaxial deformation (p>0.2; Figure 6.4). The elastin and collagen fiber orientation did not considerably change with growth (p>0.06; Figure 6.4 and Figure 6.5), which confirms the elastin results reported in Chapter 5.0. Mean Elastin and collagen fiber orientations were similar (p>0.1) and nearly circumferential, 1±2 deg. The collagen fibers were more aligned, using the average of both age groups (NOI: 71±3%), compared to the elastin fiber network (NOI: 57±2%, p=0.02). However, it should be noted that the presence of two peaks in the fiber orientation distribution of collagen in the adult group may have somewhat confounded the NOI calculation (Figure 6.5).

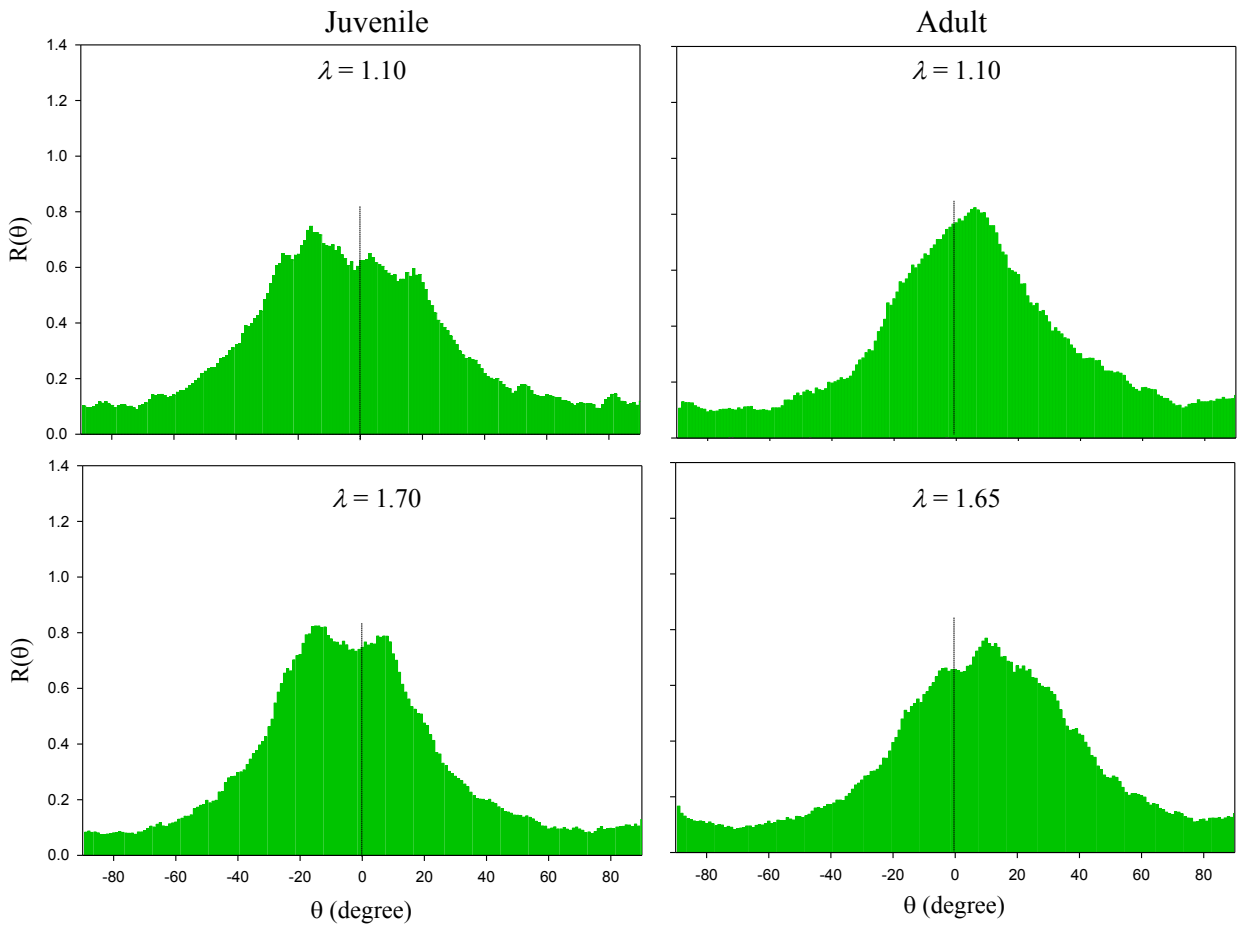

Figure 6.4. Average elastin fiber distribution of medial PA wall with growth and under equibiaxial deformation.

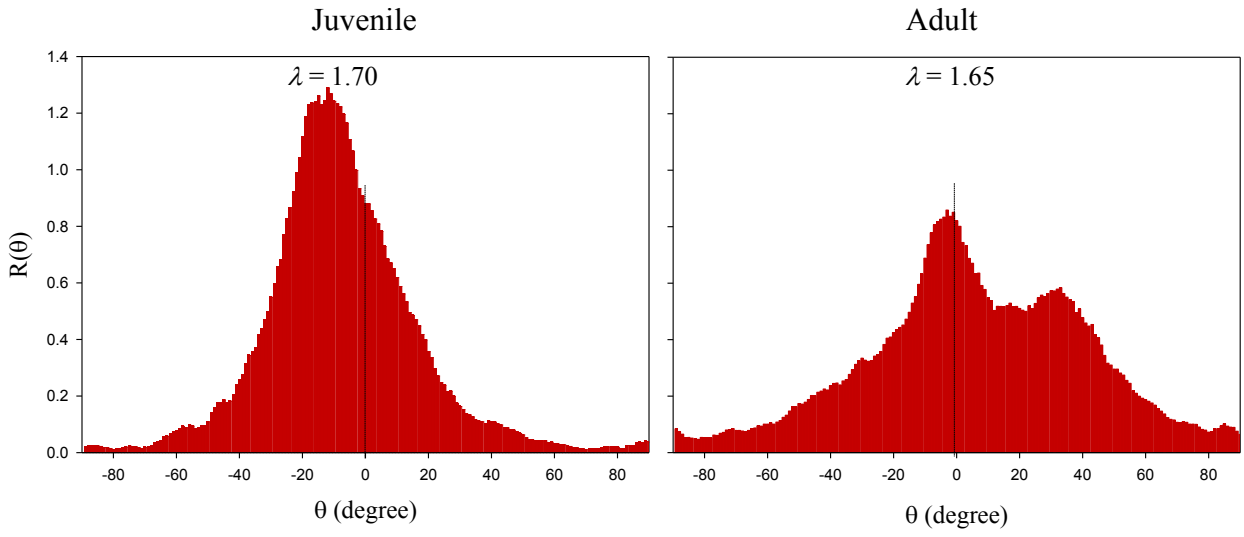

Figure 6.5. Average collagen fiber orientation distribution of medial PA wall in each growth stage.

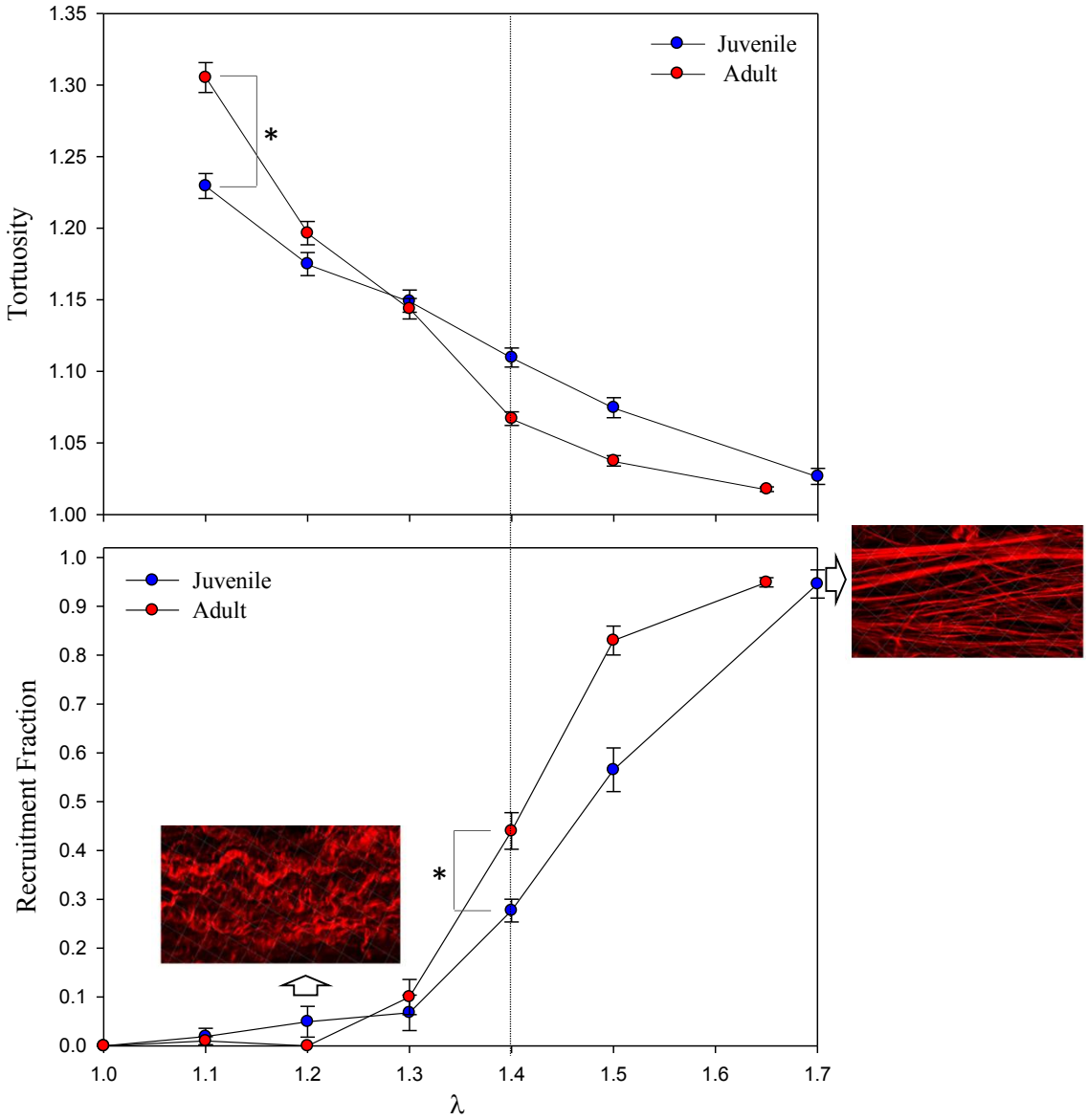

Figure 6.6. Growth adaptations in collagen fiber tortuosity and recruitment behavior of medial aspect of PA wall. Collagen fibers had a more tortuous trajectory in the adult group than juvenile specimens in stress-free state (p=0.006). Differences in collagen recruitment behavior became significant at and above λ=1.4 (p<0.004), where fibers in adult specimens were recruited at a faster rate (with respect to deformation). This deformation state was equal to or beyond peak physiologically relevant circumferential deformations measured in biaxial testing experiments of section 4.2.1.2.

The collagen fiber tortuosity did not significantly change between the stress-free and 10% stretch in both age groups (p>0.4). Therefore, the tortuosity values of fibers in both these configurations were combined to calculate the mean fiber tortuosity of the stress-free PA wall. The collagen fibers had a more tortuous trajectory in the adult group, 1.31±0.01, than the

juvenile specimens, 1.23±0.01; (p=0.006). The tortuosity was calculated to be 1.04±0.01 for juvenile specimens and 1.02±0.002 for adult samples at their respective applied maximum equibiaxial deformations. Henceforth, the critical fiber recruitment tortuosity, beyond which a fiber was considered straight, was defined to be 1.04. The decrease in fiber tortuosity with respect to applied deformation correlated well with the increase in fiber recruitment (Figure 6.6). The fiber recruitment seemed to start after λ=1.20 in adult specimens and after λ=1.10 in juvenile group. However, the difference between recruitment behavior of the two age groups did not become significant until after λ=1.4 (p<0.004), where fibers in adult samples were recruited on average 1.4 times faster than fibers in the juvenile specimens.

6.4 DISCUSSION

The gradual unfurling of collagen fibers or fiber recruitment has been postulated to be the underlying cause for the nonlinear stiffening of arterial wall with increasing stress [87]. The traditional techniques of staining and fixation techniques have been used to quantify the collagen recruitment process [182]. In this approach, a single tissue sample can only provide structural information at a single level of stretch. The sectioning and fixation can also interfere with the native collagen configuration. Furthermore, the 2D analysis of fiber crimp structure can skew the tortuosity measurements because of the 3D nature of fiber trajectory. Hill and coworkers [184] combined a uniaxial loading device with the MPM system to directly measure the 3D collagen fiber paths and evaluate the collagen recruitment process for the first time. This approach enabled 3D collagen fiber architecture to be imaged at multiple stretch values for the same

sample. Thus, a single specimen could provide multiple data points and comparisons could be made between the level of collagen crimp through the loading process.

As previously explained (section 1.4.1), uniaxial testing does not sufficiently replicate the biaxial nature of cardiovascular tissues' *in situ* boundary conditions. Furthermore, in non-equibiaxial deformation, due to the dispersion of the fibrous structure of the arterial wall, the deformation experienced by fibers is a function of their orientation with respect to the loading direction. Therefore, the degree of fiber uncrimping does not directly correlate with the applied tissue deformation. Additionally, the possible non-affine deformation of underlying fibrous structure during uniaxial and non-equibiaxial loading means that deformation of fibers cannot be related to tissue level strain measurements. Therefore, in this work we used a custom biaxial tension device combined with the MPM system to directly evaluate and quantify the collagen fiber recruitment behavior under equibiaxial deformation.

The 2D elastin and collagen fiber orientation was measured in projected image stacks. Fiber tortuosity was measured from 3D fiber traces obtained from 3D rendered MPM images at different stretch levels. Measurement of 3D fiber orientation demonstrated that the medial collagen fibers lie mainly in the plane of the wall. This supports the selection of a 2D fan splay form of distribution rather than use of the 3D conical splay orientation distribution of the fibers in the mechanical modeling of the vessel wall [106, 185]. The elastin fiber orientation measurements were consistent with the results of arterial wall sections (section 5.3.2). The change in organization of elastin fibers was not significant with growth. The collagen fiber orientation seemed to have changed with growth; however, this change was not statistically significant.

It was verified that the equibiaxial deformation did not cause noticeable change in the orientation distribution of elastin fibers, meaning that fiber rotation with deformation was minimal. Thus, fibers deformed in an affine fashion in this specific applied deformation protocol; in other words, fiber deformation correlated with the tissue level deformation. The measured circumferential and longitudinal stretch values of adult medial PA wall samples near peak physiological biaxial stress levels were measured to be 1.37±0.03 and 1.41±0.03, respectively (Figure 6.7). Thus, the applied equibiaxial deformation approximately replicated the physiological biaxial deformation experienced by the PA wall under the *in vivo* condition.

The collagen fibers had a considerably more tortuous trajectory in the adult group compared to the juvenile growth stage. However, this feature did not lead to a slower overall collagen fiber engagement with deformation. On the contrary, while having a slightly slower engagement rate (with respect to deformation) below 30% stretch level, the collagen fibers were recruited at a significantly faster rate in the adult specimens with the difference becoming significant starting at λ=1.4, where 30 to 40% of fibers were recruited. Comparison of this data with the biaxial stress-stretch data of Chapter 4.0 reveals that this stretch level may be near or beyond the maximum physiological deformation level of the PA wall, especially in the circumferential direction (Figure 6.7).

Hill et al. [184] direct measurements of collagen recruitment behavior demonstrated that collagen fibers start contributing to the arterial wall mechanics at a finite strain. The current results confirmed their finding. In both groups, there was not any collagen engagement at and below λ=1.10, and minimal engagement below λ=1.30. The biaxial testing results of medial wall, reported in Chapter 4.0, indicated that the average estimated end-diastolic ($P_{circ} \cong 18$ kPa) and peak systolic ($P_{circ} \cong 35$ kPa) stress levels resulted in about 20% and less than 40%

circumferential deformations, respectively. Therefore, the mechanical behavior of the PA wall within the normal cardiac loading cycle is determined to a large degree by elastin and not collagen. The existence of significant compressive residual strain near the endoluminal surface of the PA wall (section 1.4.2), where the collagen architecture was analyzed, implies that collagen fibers should have even smaller crimp period in the unloaded cylindrical configuration of the artery. This suggests that the engagement of collagen fibers would happen even at a larger deformation *in vivo* than current measurements indicated.

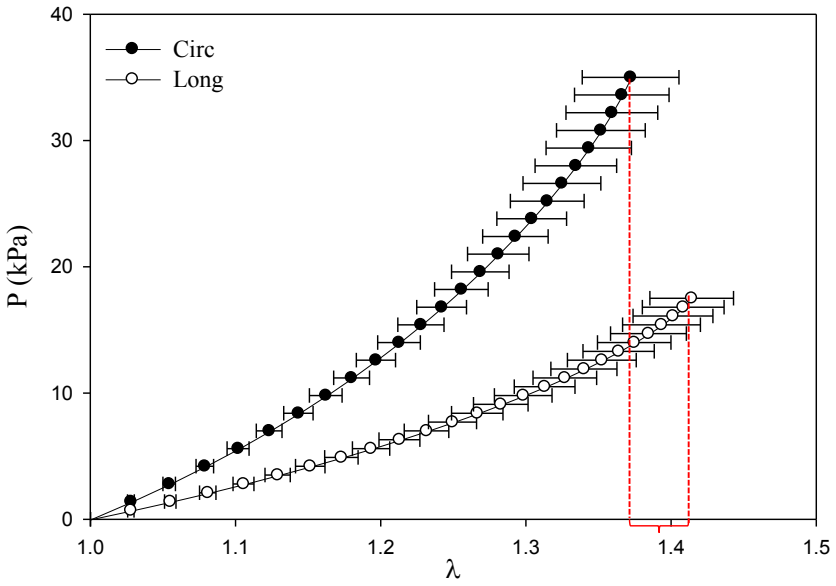

Figure 6.7. Biaxial stress-stretch behavior of medial aspect of adult PA wall near physiological biaxial stress levels. Circumferential and longitudinal stretch values of adult medial PA wall samples near peak physiological biaxial stress levels were similar; thus, applied equibiaxial deformation in this study approximately replicates physiological biaxial deformation experienced under the *in vivo* condition. Furthermore, difference in collagen recruitment behavior between adult and juvenile specimens became significant starting at λ=1.4; this stretch level is near or beyond the maximum physiological deformation level of PA wall as shown here.

The alteration in the collagen recruitment behavior with growth suggests a modification in the collagen structural properties. This change in the collagen response could also imply alteration in the elastin-collagen interaction. Wells et al. [60] investigated the relationship between mechanics and ECM composition of the ovine thoracic aorta wall during postnatal

maturation. They measured a substantial increase in the incremental elastic modulus at high tensile stress during postnatal life that corresponded to a dramatic increase in the collagen cross-linking index in absence of a significant change in the relative collagen content. The possible rise in the cross-linking of collagen fibers in the PA wall can be the underlying cause of the increase in collagen recruitment rate with growth. This claim needs to be verified with experimental measurements of ECM composition in the PA wall at different postnatal growth stages.

The results reported in Chapters 4.0 and 5.0 determined that stress was not the mechanical parameter that was maintained during normal growth process, and that stress levels in the arterial wall increased with growth. The faster recruitment rate of collagen could be an indication of the collagen remodeling to maintain the maximum deformation level in the arterial wall. Further studies should be conducted to verify this hypothesis.

In this study we only considered the medial collagen fibers in the proximity of endoluminal surface of the arterial wall. The visual inspection of the collagen fiber crimp structure throughout the stress-free PA wall revealed an increase in the crimp period from intima towards the adventitia (Figure 5.1 and Figure 5.3), implying that the collagen engagement occurs earlier proximal to tunica intima. Therefore, the contribution of collagen fibers is more substantial more proximally in the medial layer. A more thorough investigation of the collagen recruitment behavior throughout the arterial wall, especially in the *in situ* cylindrical configuration, is necessary; however, due to the depth limitation of the MPM, similar direct measurements of the whole PA wall are not currently feasible. The larger average tortuosity of the collagen fibers in the stress-free adult specimens could be due to the smaller compressive circumferential residual strains in the adult PA wall compared to the juvenile stage (section

4.2.2). Thus, in the unloaded *in situ* configuration, the collagen fibers probably have a more similar level of undulation between the two age groups.

The current study demonstrated for the first time significant alterations in the collagen recruitment behavior during postnatal growth period. Understanding the underlying mechanism of this change in collagen recruitment behavior during growth will help to determine the primary mechanical factors influencing the arterial wall's normal remodeling and growth process.

7.0 INCORPORATION OF ALL EXPERIMENTAL MEASURMENTS INTO A MODIFIED STRUCTURAL CONSTITUTIVE MODEL

This chapter presents the modeling framework to incorporate the plethora of experimental measurements into a structurally based constitutive model, as outlined in the third specific aim (section 1.7). The previous collagen recruitment measurements revealed that collagen engagement is minimal within the normal physiological loading range. Therefore, in order to describe the nonlinear anisotropic behavior of the tunica media in the medial PA wall specimens, the mechanical contribution of the elastin network had to be separated from the isotropic fairly linear contribution of the ground matrix, represented by a neoHookean model. A nonlinear phenomenological elastin model based on the limiting chain extensibility phenomenon of the atactic rubber polymer, suggested by Ogden [178] based on the Fung-Demiray model [186], was utilized. The Fung-Demiray model was modified in order to incorporate the orientation distribution measurements of elastin fibers and account for the anisotropic contribution of the elastin network, as also established by previous investigators. This new constitutive model of the tunica media of the PA wall provided high quality fit of the five-protocol biaxial stress-stretch data of the medial wall specimens based only on optimization of four model parameters.

7.1 BACKGROUND

The altered mechanical properties of arteries are critically associated with microstructural remodeling. The mechanical load-deformation relation of elastin and collagen fibril bundles is fundamental to understanding the underlying microstructural mechanisms of tissue behavior. Structurally motivated models incorporate significant mechanical aspects of the underlying microstructure to better predict the mechanical behavior and understand the mechanisms governing the structure-function relationship of biological tissues. The constitutive model developed takes account of contributions of the collagen component, elastin or elastic fibers (sections 1.5 and 1.6.2), and ground matrix, consisting of non-fibrillar elastin, smooth muscle cells and other non-cellular materials.

The increased rate of collagen and elastin synthesis in blood vessels in connection with both systemic and pulmonary hypertension has been revealed by many biological studies. Structural and degradative alterations of medial elastin is found to be a major contributing factor in physiological phenomena such as aging, and the initiation and development of cardiovascular disease, such as aortic aneurysms [187, 188]. Although elastin network plays a significant role in modifying the mechanical behavior of blood vessels, the mechanical properties of elastin are not fully determined, and studies connecting microstructural changes with elastin mechanics are scarce.

Arteries are generally considered anisotropic, and this property is usually attributed to collagen fibers while the elastin contribution has been represented by the isotropic neoHookean model [86, 189, 190]. Lillie and coworkers [180] performed uniaxial tests on purified aortic elastin and demonstrated that the elastic tissue possessed an inherent anisotropy, with the circumferential stiffness 1.4 times the axial. Their results agreed with values obtained in uniaxial

tests of alkali-purified elastic tissue from canine and ovine aortas [191]. They also demonstrated that the elastic tissue behavior was non-linear in uniaxial tests.

The study of biaxial tensile behavior of isolated elastin networks of bovine thoracic aorta by Zou and Zhang in 2009 [179] revealed significant mechanical characteristics of arterial elastin. Their experimental results consistently indicated that elastin network possessed strong anisotropy that was comparable to the intact arteries, with the circumferential direction being stiffer than the longitudinal direction. Based on an entropy-based non-Gaussian affine statistical model of a network of randomly oriented molecular chains [192], they determined that change in elastin fiber orientation leads to markedly different stress–strain response.

It is now possible to carry out single-chain force-extension experiments on elastin [193]. These studies clearly indicate that elastin does not behave as a linear Hookean material. The force-extension curve of the elastin molecule chain is characterized by two regions with distinct slopes: The first region is of low curvature, where the protein extends relatively easily, followed by a substantially stiffer region, where the force-extension curve rises quickly towards a vertical asymptote. The mechanical behavior of elastin at the single chain level and the macroscopic level is similar to that of the atactic rubber-like materials [194], meaning that its strain-stiffening behavior can be explained by limiting chain extensibility. Therefore, in the present study the elastin mechanics is represented by a function that simulates the limiting chain extensibility behavior, a concept based upon rubber elasticity [178]. This function is derived from the model introduced by Demiray based on Fung's model [186]. Ogden and Saccomandi [178] proposed using this model to account for the nonlinear isotropic contribution of the elastin network.

The results of the current study revealed the presence of a distinctly oriented elastin structure in the tunica media of the PA wall (section 5.3.2), and the previous studies, referred to

above, indicated arterial elastin exhibiting considerable anisotropy. Therefore, the Fung-Demiray model is modified to incorporate the anisotropic nonlinear contribution of the elastin network to the mechanical behavior of the PA wall.

7.2 CONSTITUTIVE MODEL FORMULATION

The biomechanics of the tunica media of the medial aspect of the PA wall is modeled at two quasistatic snapshots of postnatal growth (juvenile and adult) based on the following assumptions and considerations:

1. The general form of the constitutive model is assumed to be maintained during the postnatal maturation period. This assumption is partially supported by the fact that the shape of the stress-stretch curve was relatively conserved with growth (section 4.2.1.2).
2. The mechanical response of tunica media can be idealized into a single response function per unit area.
3. The collagen and elastin are considered to be the mechanically dominant components compared to smooth muscle cells.
4. Both elastin and collagen fibers bear load only along their fiber axes and have negligible resistance to compressive forces.
5. The contribution of elastin-collagen interaction to the mechanical behavior is ignored; therefore, the net tissue response is considered to be the sum of the individual constituent responses.

6. The contribution of either of these fibers is mainly in the plane of the wall (radial mechanical behavior of the artery is governed mostly by the incompressible and ground matrix constituents).
7. It is assumed that the load required to straighten the collagen fibers is negligible compared to the load transmitted by elastin or stretched collagen. Thus, collagen bears load only when nearly or completely straight.
8. Contributions from non-load bearing constituents are combined with the ground matrix.
9. The reference state for all model calculations is the post-preconditioned state as defined in section 4.1.1.3.

The tissue level strain energy density Ψ of the RVE is assumed to result from the contribution of collagen (*col*), elastin (*el*) and ground matrix (*gm*), which includes the sparse elastic sheets or laminae and smooth muscle cells, weighted by their respective volume fractions ϕ according to

$$\Psi(\mathbf{C}) = \phi_{col}\Psi_{col}(\mathbf{C}) + \phi_{el}\Psi_{el}(\mathbf{C}) + \phi_{gm}\Psi_{gm}(\mathbf{C}). \tag{6.1}$$

The tissue level response in terms of the 2nd Piola-Kirchhoff stress is defined as

$$\mathbf{S} = 2\frac{\partial\Psi(\mathbf{C})}{\partial\mathbf{C}} - p\mathbf{C}^{-1} = 2\phi_{col}\frac{\partial\Psi_{col}}{\partial\mathbf{C}} + 2\phi_{el}\frac{\partial\Psi_{el}}{\partial\mathbf{C}} + 2\phi_{gm}\frac{\partial\Psi_{gm}}{\partial\mathbf{C}} - p\mathbf{C}^{-1}, \tag{6.2}$$

where ϕ_{gm} = 1- (ϕ_{el} +ϕ_{col}); the Lagrange multiplier p, which accounts for the incompressible or isovolumetric deformation, is assumed to be associated only with elastin and ground matrix constituents of the tissue. A structurally based modeling approach is employed for the collagen and elastin strain energy functions: The contribution of individual fiber ensembles acting in a

given direction $\mathbf{N}(\theta)=\begin{bmatrix}\cos(\theta)\\ \sin(\theta)\end{bmatrix}$ (in the reference state; Figure 2.4) is summed over all orientations, using a probability distribution function. Thus it assumes the form

$$\begin{aligned}\Psi_{col}(\mathbf{C}) &= \phi_{col}\int_{\theta} R_{col}(\theta)\Psi_{col}^{ens}(\mathbf{C})d\theta \\ \Psi_{el}(\mathbf{C}) &= \phi_{el}\int_{\theta} R_{el}(\theta)\Psi_{el}^{ens}(\mathbf{C})d\theta\end{aligned}, \tag{6.3}$$

where functions R_{col} and R_{el} govern the planar angular distributions of collagen and elastin fibers, respectively; Ψ_{col}^{ens} and Ψ_{el}^{ens} are collagen and elastin fiber ensemble strain energy functions, respectively.

The collagen fibers in an ensemble are represented by a collection of springs that engage at various tissue deformation levels or slack stretches λ_s [89]. Hence, the ensuing collagen ensemble stain energy is considered to be the sum of individual fiber strain energies ψ_{col}^{f} weighted by the recruitment probability function or the distribution of slack stretches d as

$$\Psi_{col}^{ens}(\lambda_f)=\int_0^{\lambda_f} d(\lambda_s)\psi_{col}^{f}(\lambda_s)d\lambda_s\,, \tag{6.4}$$

where λ_f is the stretch along fiber axis.

Based on the X-ray diffraction observation of D-spacing of heart valve and tendon collagen fibers, Sasaki et al. [195, 196] suggested that the straight collagen fiber has a linear force-displacement behavior. However, the single-chain force extension experiments of collagen type II fibers in a more recent study by Sun et al. [197] revealed that collagen fiber has a nonlinear loading behavior. Since the deformation range considered in this study is within the physiological range and substantially below full collagen engagement (sections 6.3 and 6.4), the mechanical contribution of the collagen fibers are considered to be within the linear region of their tensile force-extension curve.

The linear fiber force-displacement relation, when normalized using the reference state fiber cross-sectional area and length, becomes the following linear relation based on the 1st Piola-Kirchhoff stress and stretch:

$$P_{col} = \kappa_{col}[\lambda_t - 1], \tag{6.5}$$

where κ_{col} is the elastic modulus of the individual straight collagen fibers, and λ_t is the true fiber stretch (Figure 7.1) defined according to

$$\lambda_t = \frac{\lambda_f}{\lambda_s}, \tag{6.6}$$

where $\lambda_f = l/l_0$ and $\lambda_s = l_s/l_0$. Based on the relation $P_f = \frac{d\psi}{d\lambda_t}$, the elastin ensemble or collagen fiber strain energy is defined as

$$\psi_{col}^{f}(\lambda_f) = \frac{\kappa_{col}}{2}(\lambda_t - 1)^2. \tag{6.7}$$

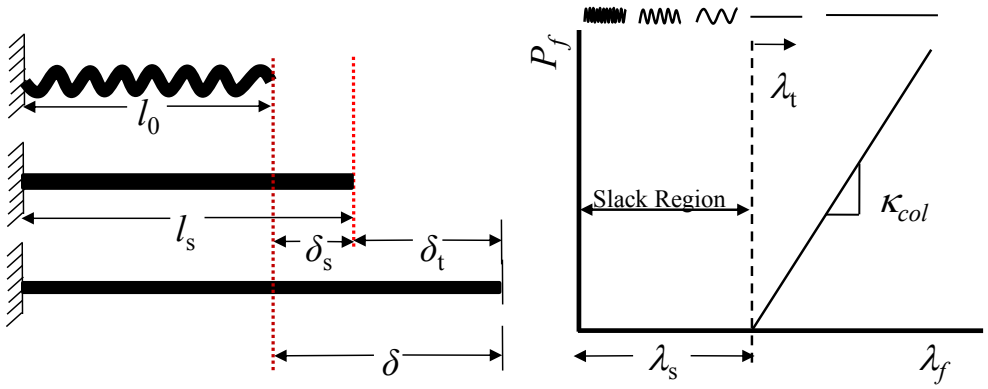

Figure 7.1. Schematic of different length and displacement definitions of an initially undulated collagen fiber (left); Stress-deformation curve of a single crimped collagen fiber (right).
l_0 is reference length used for fiber stretch calculations; l_s refers to slack length or actual fiber length; δ_s is slack displacement or difference between end-to-end length and actual fiber length; δ_t is true fiber displacement (or stress-generating displacement) and δ is combined fiber displacement (left). λ_s is slack or straightening stretch of single collagen fiber; λ_f is total stretch along fiber axis; λ_t is true stretch or stretch of straight fiber, κ_{col} is collagen elastic modulus.

The Fung-Demiray [186] limiting chain extensibility elastin model [178] is given by

$$\Psi_{el}^{iso} = \frac{\mu}{2b}\{\exp[b(\mathrm{I}_1 - 3)] - 1\}, \tag{6.8}$$

where μ represents the shear modulus, b is a dimensionless material constant, and I_1 is the first invariant of **C** ($\mathrm{I}_1 = \mathrm{tr}(\mathbf{C})$, Eq. (2.46)). To account for anisotropic contribution of elastin network, the above relation has to be modified to be in terms of fiber deformation. The elastin fiber is assumed to be transversely isotropic and bear load only along its axis; I_1 can be written in terms of the local fiber coordinate as $\mathrm{I}_1 = \lambda_f^2 + 2\lambda'^2$, where λ_f is deformation along fiber axis and λ' is the deformation orthogonal to the fiber axis ($\lambda_2' = \lambda_3' = \lambda'$). The elastin fiber can be considered to be nearly incompressible within the physiological deformation range; thus, $\lambda_f \lambda'^2 = 1$ or $\lambda'^2 = \lambda_f^{-1}$. The final relation for the first invariant is then given by

$$\mathrm{I}_1 = \lambda_f^2 + 2\lambda_f^{-1}. \tag{6.9}$$

Using Eqs. (6.8) and (6.9), the elastin ensemble strain energy is described by

$$\Psi_{el}^{ens} = \frac{\mu}{2b}\left\{\exp[b(\lambda_f^2 + 2\lambda_f^{-1} - 3)] - 1\right\}, \tag{6.10}$$

where μ is the shear modulus of the elastin ensemble.

The isotropic contribution of the ground matrix, including sparse elastic sheets, are represented by the neoHookean model as

$$\Psi_{gm} = \frac{\mu'}{2}(\mathrm{I}_1 - 3), \tag{6.11}$$

where μ' is the shear modulus of ground matrix and I_1 is the first invariant given in terms of global tissue deformation as

$$\mathrm{I}_1 = \lambda_1^2 + \lambda_2^2 + \lambda_3^2,$$

where $\lambda_3 = 1/\lambda_1\lambda_2$ based on the incompressibility assumption.

The collagen or elastin contribution to the tissue stress is derived according to

$$\mathbf{S}_i = 2\frac{\partial \Psi_i}{\partial \mathbf{C}} = 2\phi_i \int_{-\pi/2}^{\pi/2} R_i(\theta) \frac{\partial \Psi_i^{ens}}{\partial \mathbf{C}} d\theta, \tag{6.12}$$

where $i = col$ or el; the second term is derived based on the relation

$$\frac{\partial \Psi_i^{ens}}{\partial \mathbf{C}} = \frac{\partial \Psi_i^{ens}}{\partial \lambda_f} \frac{\partial \lambda_f}{\partial \mathbf{C}}, \tag{6.13}$$

where $\frac{\partial \Psi_{col}^{ens}}{\partial \lambda_f} = \frac{\partial \Psi_{col}^{ens}}{\partial \lambda_t} \frac{d\lambda_t}{d\lambda_f}$, and since $\lambda_f^2 = \mathbf{N}^{\mathrm{T}}\mathbf{C}\mathbf{N}$, Eq. $(2.16)_1$, the second term is determined according to

$$\frac{\partial \lambda_f}{\partial \mathbf{C}} = \frac{\mathbf{N} \otimes \mathbf{N}}{2\lambda_f}. \tag{6.14}$$

Thus, the final collagen ensemble stress tensor form is given by

$$\mathbf{S}_{col}^{ens} = \eta_{col} \left\{ \int_0^{\lambda_f} d(\lambda_s) \frac{1}{\lambda_s} \left(\frac{1}{\lambda_s} - \frac{1}{\lambda_f} \right) d\lambda_s \right\} \mathbf{N} \otimes \mathbf{N}, \tag{6.15}$$

where $\eta_{col} = \phi_{col}\kappa_{col}$ is the effective collagen fiber modulus. Therefore, the collagen stress component is given by

$$\mathbf{S}_{col} = \eta_{col} \int_{-\pi/2}^{\pi/2} R_{col}(\theta) \left\{ \int_0^{\lambda_f} d(\lambda_s) \frac{1}{\lambda_s} \left(\frac{1}{\lambda_s} - \frac{1}{\lambda_f} \right) d\lambda_s \right\} \mathbf{N} \otimes \mathbf{N} \, d\theta \tag{6.16}$$

The elastin ensemble stress in terms of 2nd Piola Kirchhoff stress in the local fiber coordinate is derived using (Eqs. (2.41) and $(2.48)_3$)

$$S_{el}^{ens} = \frac{1}{\lambda_f} \frac{d\Psi_{el}^{ens}}{d\lambda_f} - p_{el}\lambda_f^{-2} \tag{6.17}$$

where p_{el} is the Lagrange multiplier associated with the elastin fiber deformation in an ensemble, which can be determined from the relations for the stress components normal to the fiber axis $S_{22} = S_{33} = 0$. Hence, the final relation for the ensemble elastin stress is

$$S_{el}^{ens} = 3\mu(1-\lambda_f^{-3})\exp[b(\lambda_f^2 + 2\lambda_f^{-1} - 3)]. \tag{6.18}$$

The final form of the stress tensor for the elastin component is given by

$$\mathbf{S}_{el} = \eta_{el}\int_{-\pi/2}^{\pi/2} R_{el}(\theta)(1-\lambda_f^{-3})\exp[b(\lambda_f^2 + 2\lambda_f^{-1} - 3)]\mathbf{N}\otimes\mathbf{N}\, d\theta\,, \tag{6.19}$$

where $\eta_{el} = 3\phi_{el}\mu$ is the ensemble elastin effective elastic modulus.

To determine the principal biaxial (circumferential and longitudinal) stress contribution of the ground matrix, represented by the neoHookean model, a derivation similar to Eqs. (2.43) based on the relation for the 2nd Piola Kirchhoff, Eq. $(2.48)_3$, gives rise to the relations

$$\begin{aligned} S_{11}^{gm} &= \eta_{gm}(1-\frac{1}{\lambda_1^4\lambda_2^2}) \\ S_{22}^{gm} &= \eta_{gm}(1-\frac{1}{\lambda_1^2\lambda_2^4}) \end{aligned}, \tag{6.20}$$

where $\eta_{gm} = \phi_{gm}\mu'$ is the effective shear modulus of the ground matrix.

7.2.1 Fitting of Fibers' Orientation Distribution Measurements

The measurements of the 2D orientation of the collagen and elastin fibers need to be represented by circular statistics to be included into the constitutive model, as $R(\theta)$ in Eqs. (6.3). In this study von Mises distribution, VM(φ,k), was chosen as probability distribution function for the fiber orientation distribution. The probability density function of the unimodal von Mises distribution is defined according to

$$R(\theta) = \frac{\exp[k\cos(\theta-\varphi)]}{2\pi I_0(k)}, \quad 0 \le \theta < 2\pi, \quad 0 \le k < \infty \tag{6.21}$$

where φ is the mean orientation and I_0 is the modified Bessel function of order zero given by

$$I_0(k) = \frac{1}{2\pi}\int_0^{2\pi} \exp[k\cos(\theta)]d\theta\,. \tag{6.22}$$

When k tends to infinity, the von Mises distribution approaches the Gaussian distribution with variance $1/k$. The parameter k is related to the circular standard deviation σ through the relation

$$\sigma = \sqrt{-2\ln\left|\frac{I_1(k)}{I_0(k)}\right|}, \tag{6.23}$$

where I_1 is the modified Bessel function of order one.

The mean orientation distribution of elastin was obtained by averaging all the orientation measurements of the of the medial PA wall (sections 5.3.2 and 6.3). The mean collagen fiber orientation distribution data was based on measurements made in the previous chapter (Figure 6.5). By plotting the histograms for the mean orientation data of collagen and elastin fibers, it was observed that the orientation distributions were either quite asymmetric or that there were two predominant peak orientations (Figure 7.2). Because of the nature of the fiber distributions, a mixture of two π-periodic von Mises populations was used to represent the mean orientation distribution data, defined as

$$R(\theta) = \frac{1}{2}\left(\frac{\exp[k_1\cos(2(\theta-\varphi_1))]}{\pi I_0(k_1)} + \frac{\exp[k_2\cos(2(\theta-\varphi_2))]}{\pi I_0(k_2)}\right), \tag{6.24}$$

where φ_i and k_i (i = 1,2) are the absolute value of the means and spread parameters of each fiber population, respectively.

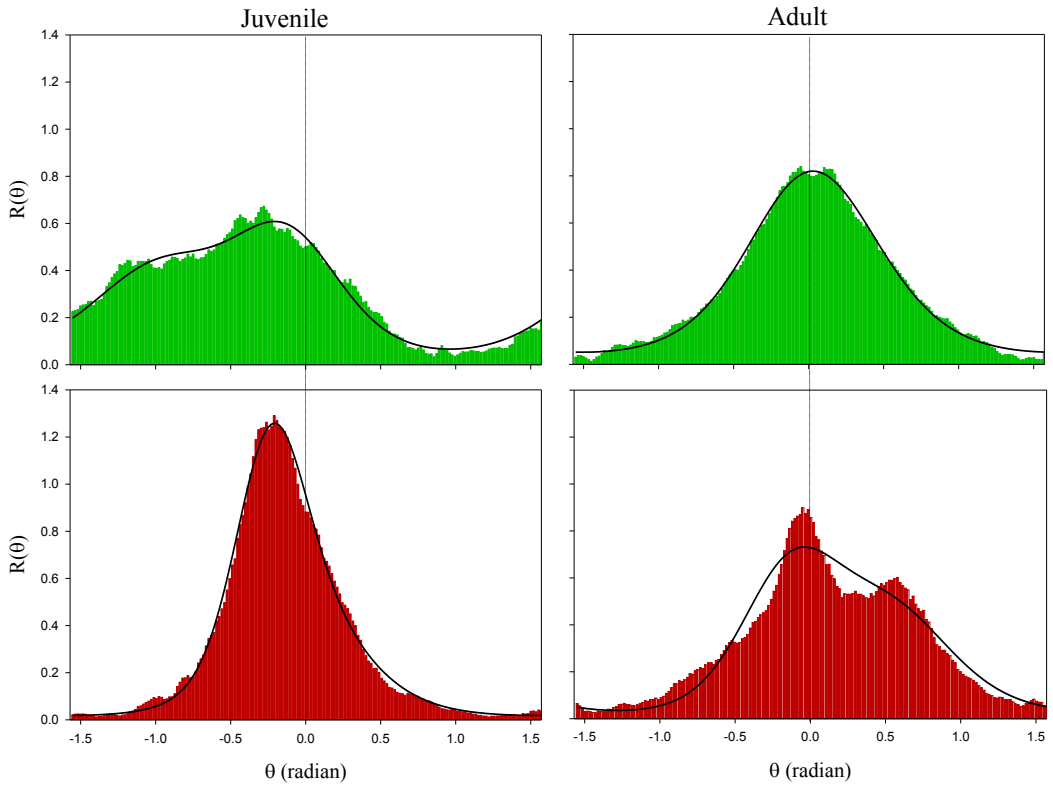

Figure 7.2. Final average elastin and collagen measured orientation distributions and bimodal von Mises probability distribution fits.

7.2.2 Fitting of Collagen Recruitment Measurements

The gradual recruitment of collagen fibers in the RVE, a process in which fibers in an individual ensemble engage into load transmission as they become straightened, has been described by different probability distribution functions [92, 93]. The beta cumulative probability density function (β_{CDF}) provided a truthful representation of the collagen recruitment measurements in the juvenile specimens, D_{jvl} (Figure 7.4). The beta probability density β_{PDF} is a continuous function and is parameterized by two positive shape parameters *a* and *b* according to

$$d_{jvl}(\lambda_s) = \beta_{\text{PDF}} = \frac{1}{\text{B}(a,b)} x^{a-1}(1-x)^{b-1}, \quad D_{jvl}\Big|_{\lambda_f=\lambda^{ub}} = \int_1^{\lambda^{ub}} d_{jvl}(\lambda_s) d\lambda_s = 1, \tag{6.25}$$

where B(.) is the Beta function, that appears as normalization constant. The beta probability distribution is defined on the interval $x \in [0, 1]$ as follows

$$x = \frac{\lambda_s - 1}{\lambda^{ub} - 1}, \tag{6.26}$$

where λ^{ub} is the upper bound stretch, where all ensemble fibers are straight. The quality of β_{CDF} fit to experimental recruitment measurements is considerably dependent on λ^{ub}. Therefore, λ^{ub} was varied to find the closest value to the maximum applied experimental stretch that resulted in the minimum RMS error between the recruitment measurements and the fit (Figure 7.3). Based on the results obtained, λ^{ub} was set to 1.82.

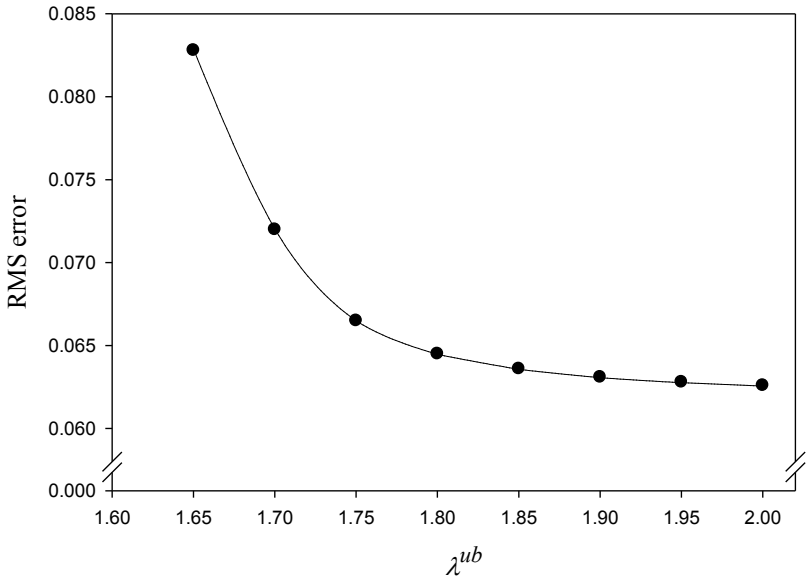

Figure 7.3. Determining upper bound stretch in beta recruitment function based on RMS error of fit to experimental measurements in juvenile specimens.

The recruitment measurements in adult specimens (D_{adt}) were more accurately modeled with the gamma cumulative probability distribution function Γ_{CDF} (Figure 7.4), whose probability density function is given by

$$d_{adt}(\lambda_s) = \Gamma_{PDF} = \frac{1}{A^B \Gamma(A)} x^{A-1} e^{\frac{-x}{B}}, \quad D_{adt}\big|_{\lambda_f \to \infty} = \int_1^{\infty} d_{adt}(\lambda_s) d\lambda_s = 1, \tag{6.27}$$

where A is the shape parameter, B is the scale parameter and $\Gamma(.)$ the Gamma function; x is defined according to Eq. , where λ^{ub} was set to the maximum applied biaxial stretch of 1.65.

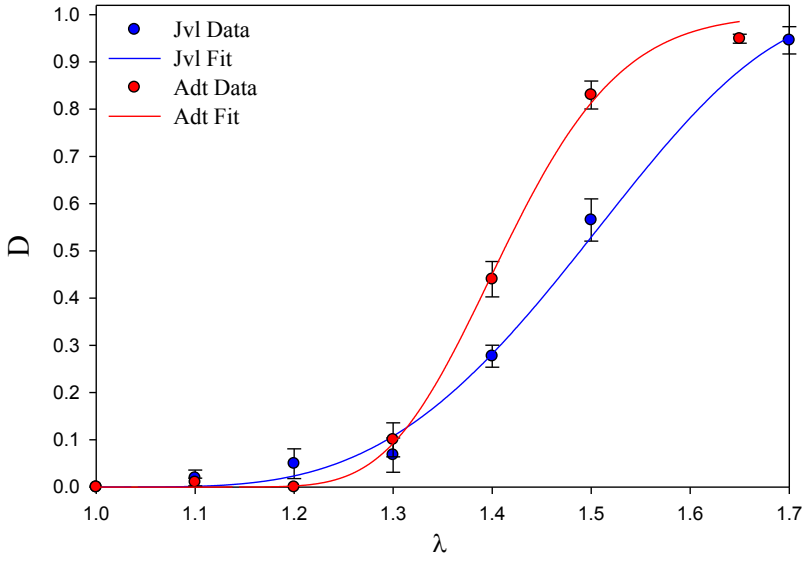

Figure 7.4. Beta and gamma cumulative distribution function fits to mean juvenile and adult collagen recruitment data, respectively.

7.2.3 Parameter Estimation

The process of parameter estimation also referred to as model fitting, aims at determining parameter values for a model through capturing experimental data as closely as possible. An error function or objective function is minimized, which is usually defined as the sum-of-squared errors between the experimental data values and calculated model values. Finding the minimum

value of the objective function, using a predefined tolerance value, is an iterative procedure: After giving a set of initial estimates for the parameters, the parameter values are altered in each iteration to attain a smaller value of the objective function and to eventually reach the optimal set of parameters.

Most of the available optimization algorithms are the gradient-based methods, e.g. Levenberg-Marquardt method, which rely on the smooth behavior of the error surface. The final parameter values found in gradient-based methods are usually dependent on the initial parameter estimates, and there is the risk of reaching only a local minimum of the objective function. The alternative is to use a more robust global approach such as the genetic algorithm. The genetic algorithm uses the survival of the fittest concept mimicking the process of natural evolution. A group of parameters sets is maintained instead of just one working solution set, and based on how well each set fits the data, it is either used to produce better candidate solutions or discarded. Although the genetic algorithm and other global minimization approaches increase the likelihood of reaching the global minimum of the objective function in a given parameter space, they require an exhaustive sampling of the parameter space at a considerable computational expense. The use of these methods are, therefore, more applicable in problems with relatively large number of parameters, where there are usually larger number of local minima and a high chance of failure of a purely gradient-based method to locate the global minimum.

In this study, most of the measureable structural parameters were experimentally determined, and only four parameters (Table 7.1) for each age group were determined by fitting of the constitutive model to the mean of each group's five-protocol biaxial mechanical data. The objective function minimized to find the optimal parameters was defined according to

$$SSE = \sum_i \left[\left(S_{11,i}^{\text{mod}} - S_{11,i}^{\text{exp}} \right)^2 + \left(S_{22,i}^{\text{mod}} - S_{22,i}^{\text{exp}} \right)^2 \right] \tag{6.28}$$

Table 7.1. List of experimentally measured and estimated parameters.

Parameters	Measured Experimentally	Estimated through Model
Collagen recruitment, $d(\lambda)$	√	
Elastin angular distribution, $R_{el}(\theta)$	√	
Collagen angular distribution, $R_{col}(\theta)$	√	
Elastin model constants, η_{el}, b		**2**
Collagen elastic modulus, η_{col}		**1**
Ground matrix effective shear modulus, η_{gm}		**1**

The complete structural constitutive model is highly nonlinear mainly because of the orientation distribution functions and elastin model and the recruitment function. This highly nonlinear model required a nonlinear parameter optimization or curve fitting algorithm. The model was implemented in MATLAB. The MATLAB function "*lsqcurvefit*", especially designed for curve fitting purposes of nonlinear functions, was used to perform the parameter fitting. By default, lsqcurvefit uses the (large scale) trust-region-reflective algorithm, which is a subspace trust-region method and is based on the interior-reflective Newton method. Trust-region methods are based on the basic idea to approximate the function f with a simpler function g, which reasonably reflects the behavior of function f in a neighborhood around the point x. This neighborhood is the trust region. This algorithm allows the user to define bounds on the parameters and hence perform constrained optimization. The following bounds were placed on the parameters: $100 \leq \eta_{col} \leq 10^7$; $0.1 \leq \eta_{el} \leq 100$; $0.1 \leq b \leq 25$, and $0.1 \leq \eta_{gm} \leq 300$.

7.3 RESULTS

The average orientation distribution data of elastin and collagen fibers were well fit by the mixed von Mises probability distribution function (Figure 7.2, r^2>0.94). The beta and gamma probability density functions provided accurate representation of the mean measured collagen recruitment data of juvenile (r^2 = 0.97) and adult (r^2 = 0.98) specimens, respectively (Figure 7.4).

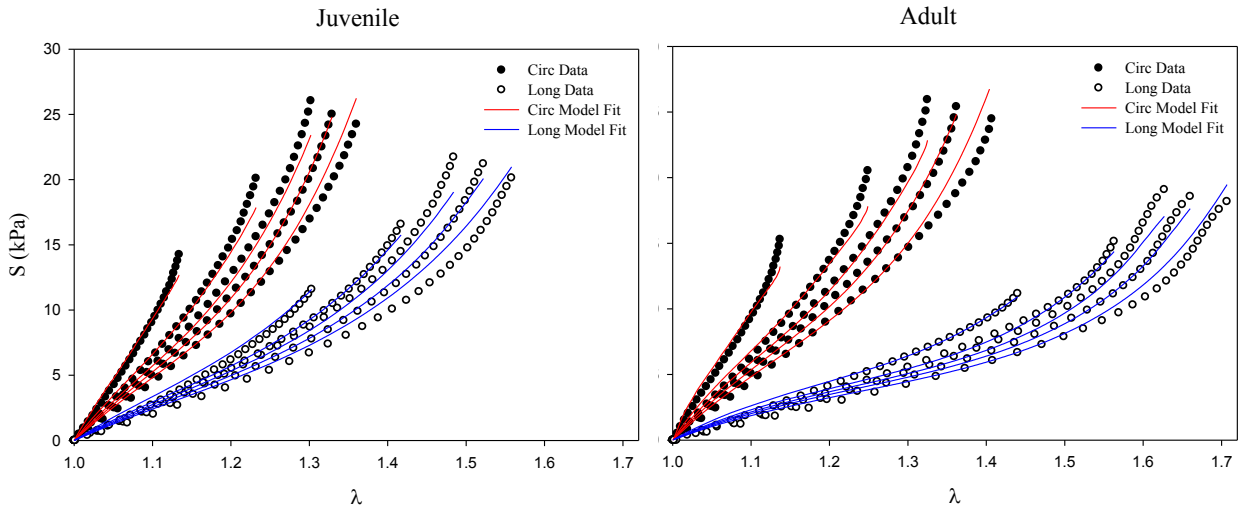

Figure 7.5. Constitutive model fit to the average five-protocol biaxial stress-stretch data of juvenile and adult medial PA wall specimens.

The modified constitutive model incorporating elastin limiting chain extensibility behavior and its anisotropic contribution enabled a very accurate simultaneous fitting of the circumferential and longitudinal stress-stretch data of five biaxial loading regiments (Figure 7.5). The final parameter values along with RMS and r^2 values of the model fit for each age group are reported in Table 7.2. Both the ground matrix and elastin constituents were load bearing in the low stress region. Since the elastin was predominately oriented circumferentially in the adult group (Figure 7.2), the ground matrix effective modulus could be accurately determined based

on the influence of ground matrix on the longitudinal stress-stretch behavior. However, due to the high degree of scattering of elastin fibers in the juvenile stage, the elastin contribution was also dominant in the longitudinal direction. Thus, the sensitivity of the model to the contribution of ground matrix component was negligible in the juvenile group; as a consequence, the effective modulus of the ground matrix could not be determined. Therefore, it was assumed that the properties of ground matrix are not altered with growth, and the juvenile ground matrix effective modulus was set equal to that of the adult value.

Table 7.2. Constitutive model fitting results (Effective moduli are in kPa).

Age Group	Parameters [95% Confidence Intervals]				r^2		RMS error
	η_{col}	η_{el}	b	η_{gm}	Circ	Long	
Juvenile	2007 [1860, 2154]	18.8 [18.6, 21.5]	2.2 [2.1, 2.3]	4.1*	0.989	0.986	1.01
Adult	169 [24.6, 314]	14.5 [14.0, 15.1]	2.7 [2.6, 2.8]	4.1 [3.8, 4.4]	0.979	0.987	1.18

*Kept constant

7.4 DISCUSSION

Constitutive models are required to describe the mechanical behavior of each layer of the arterial wall and gain insights into the mechanisms behind the mechanical response of the arterial wall. The absence of similar crimp or undulation architecture to that of the collagen fibers in the elastin network of the arterial wall and substantially smaller elastic modulus of elastin fiber means that elastin can become readily load bearing as the arterial wall starts passively extending in the *in situ* configuration or under the *in vitro* planar biaxial tensile testing condition. In the current study the strain stiffening phenomenon of the rubber polymer chains was used to model

the behavior of elastin in an RVE [178, 186]. The use of this model to describe the behavior of elastin fibers is supported by the experimental force-extension measurements on a single elastin molecule chain [193].

In most previous models of the arterial wall, the underlying orientation distribution of collagen fibers is considered to be the only cause of the strong anisotropy of the arterial wall [86, 190]. In the current work, the Fung-Demiray model was chosen to account for the strain-stiffening behavior of elastin fiber. It was subsequently modified to allow for the direct incorporation of the measured elastin orientation distribution data into the constitutive model of the tunica media of the PA wall. This modified model accounted for the anisotropic contribution of elastin network and provided a highly accurate fit of the five-protocol biaxial stress-stretch data of the PA wall based on optimization of only four parameters. The phenomenological form of this model and the correlation between the shear modulus and the dimensionless exponent parameter did not allow for elucidating possible alterations in elastin properties with growth.

The direct measurement of the collagen recruitment behavior (section 6.3) revealed that most of the collagen fibers do not become load bearing within the normal physiological deformation region of the PA wall based on the obtained biaxial stress-stretch data (P_{max}=35 kPa, section 4.2.1.2). In order to correctly characterize the collagen fiber properties, the artery has to be loaded well above the physiological loading level. In the study by Hill et al. [92], through the combined uniaxial mechanical testing-MPM system, it was revealed that collagen contribution becomes dominant after about 500 kPa stress in the circumferential (or preferred) direction in the rabbit carotid artery. Thus, the effective collagen modulus obtained based on fitting of the model to the current biaxial data cannot provide a reliable estimate of the collagen fiber properties. Therefore, to account for the nonlinear anisotropic behavior of the PA wall in the juvenile and

adult growth stages, it was necessary to separate out the contribution of the elastin network from the relatively linear isotropic response of the ground matrix.

It was observed that when the recruitment function parameters were set as variables in the optimization process, the faster collagen recruitment resulted in smaller collagen effective modulus values and vice versa. Therefore, the direct measurement of collagen recruitment behavior is necessary to prevent this covariance between the collagen model parameters skewing the determination of collagen fiber property through the constitutive model.

In the majority of previous constitutive models of the soft tissues, including those of arterial wall, the elastin contribution has been combined with that of the ground matrix. In the current study it was demonstrated that elastin substantially contributes to the nonlinear anisotropic mechanical behavior of the arterial wall. Therefore, a constitutive model of the arterial wall cannot determine the structure-function relationship of arterial wall without taking into account the nonlinear behavior of elastin fibers and the anisotropic contribution of the elastin network.

In order to gain insight into the possible physiological modifications of elastin structural properties with growth and the prominent role of elastin in the alteration of pulmonary artery mechanics in hypertension [52], more structurally relevant elastin models need to be developed. The elastin and collagen fibers are closely associated with each other in the media and are organized into concentric rings of lamella units around the arterial lumen (Figure 5.3) with smooth muscle cells lying between these lamellae [71]. In order to elucidate load-bearing mechanism of elastin and collagen constituents of the arterial wall, the effect of the cross-linking of elastin fibers with each other and their interaction with collagen fibers has to be included into the constitutive model.

8.0 SUMMARY AND CONCLUSION

The overall objective of this work was to lay the foundation for tissue engineering approaches and help elucidate the mechanisms regulating the normal remodeling and growth process by enhancing our knowledge of alterations in the structure-mechanics relationship of the main pulmonary artery during postnatal maturation. These goals were carried out through the characterization of the gross anatomy, mechanical behavior, histology, and microstructure of the PA wall during the postnatal growth period. The differences in the anatomy and mechanical behavior of PA and AA were also revealed to gain insight into physiological factors affecting the 3D geometry and governing the mechanical behavior of each artery.

It has been widely accepted that growth and remodeling is a change in the homeostatic state due to alterations in the environment and internal stresses [1]. It has been suggested that the structure of the artery adapts to changes in arterial shape during perinatal and postnatal maturation in order to maintain an equilibrium mechanical tension per elastin lamellar unit [50, 59]. In the present study we did not find any evidence that the stress was maintained in the PA wall during normal postnatal growth.

In Chapter 4.0, it was demonstrated that the thickness of the PA wall did not increase with growth implying that there is an average of 40% increase in hoop stress due to an equivalent increase in diameter. The tunica media is considered to be the most mechanically significant arterial layer as measured to occupy the major part of the PA wall in the current study (section

5.3.1). However, despite the inferred rise in the hoop stress, the relative thickness of this layer was maintained with growth. It was also revealed that the elastin and collagen concentration of the PA wall was not modified with growth (section 5.3.2). Therefore, unlike the arterial wall remodeling due to hypertension [46-48], the upsurge of elastin and collagen synthesis is not a mechanistic response to the change in wall stress during the normal postnatal growth process.

While the nonuniform wall stress distribution in the PA wall could be provided as a basis for heterogeneous residual strain pattern at a given growth stage (section 4.2.2), the same reasoning cannot explain the relative preservation of residual strain at the STJ with growth in presence of larger wall stress in the adult PA.

It was demonstrated that although the AA maximum physiological stress was about 2.7 times larger than that of the PA maximum physiological loading stress, their mean peak strains were very similar in circumferential direction and nearly identical in longitudinal direction (section 4.2.1.1). This phenomenon could be achieved due to the AA's substantially larger stiffness; on average it had 1.4-2.7 times larger longitudinal and 3.2 time larger circumferential tangent modulus when compared to the PA. This finding suggests that the mechanical driver behind the structural differences between these arteries is preservation of an optimal peak homeostatic deformation, rather than stress.

As demonstrated in Chapter 6.0 collagen fibers were recruited at a significantly faster rate (with respect to deformation) in the adult specimens,. The faster recruitment rate of collagen could be an indication of collagen remodeling to maintain the maximum deformation level in the arterial wall during postnatal maturation. Further studies should be conducted to verify this hypothesis and elucidate the driving mechanism behind the measured structural and mechanical

alterations of the PA wall. For example, the peak-systolic MR images of arterial surface should be acquired to compute and compare peak wall deformations at each growth stage.

In both juvenile and adult age groups, there was not any collagen engagement at and below λ=1.10, and minimal engagement below λ=1.30 (section 6.3). The biaxial testing results of medial wall, reported in Chapter 4.0, indicated that the average estimated peak systolic ($P_{circ} \cong$ 35 kPa) stress level resulted in less than 40% circumferential deformations. Therefore, the mechanical behavior of the arterial wall within the normal cardiac loading cycle is determined to a large degree by elastin and not collagen. The elastin content of the tunica media was also found to be significantly larger than its collagen content (section 5.3.2). Furthermore, it was revealed that the elastin fiber network had a distinct alignment, and the heterogeneity in the mechanical behavior of the PA wall was comparable with the spatial variation in the elastin organization. These results imply that elastin can play a significant role in modifying the mechanical behavior of the arterial wall in many disease processes such as in hypertension [176, 177].

Thus, a constitutive model of the arterial wall cannot determine the structure-function relationship of arterial wall without taking into account the structural properties of elastin fibers and the nonlinear anisotropic behavior of the elastin network. In most previous models of the arterial wall, the underlying orientation distribution of collagen fibers is considered to be the only cause of the strong anisotropy of the arterial wall [86, 190].

In the current study the strain stiffening behavior of a single elastin fiber was represented by the Fung-Demiray model (section 7.2). The Fung-Demiray model was then modified to allow for the direct incorporation of the measured elastin orientation distribution data and anisotropic contribution of elastin network into the constitutive model of the tunica media of the PA wall.

This modified constitutive model provided a highly accurate fit of the five-protocol biaxial stress-stretch data of the PA wall based on optimization of only four parameters.

For future studies a more structurally-based model of the elastin network needs to be developed in order to gain insight into the possible physiological modifications of elastin structural properties with growth and the prominent role of elastin in the alteration of pulmonary artery mechanics in hypertension. Furthermore, an elastin-collagen interaction term needs to be incorporated into the model to understand the role of collagen within the normal physiological loading phase.

APPENDIX A

SURFACE GROWTH DEFORMATION STUDY: RELEVANT CALCULATIONS

A1. Coordinate Transformation

The local coordinate of the surface point $\mathbf{x}'$ with its projected centerline path point, **y**, and **Q** are the 3D rotation matrix defined by local Frenet frame as

$$\mathbf{x}' = \begin{bmatrix} \rho(\theta,s)\cos(\theta) \\ \rho(\theta,s)\sin(\theta) \\ 0 \end{bmatrix},\ \mathbf{y} = \begin{bmatrix} R_{cn}(X^3)\cos(\Theta_{cn}(X^3)) \\ R_{cn}(X^3)\sin(\Theta_{cn}(X^3)) \\ X^3 \end{bmatrix} \text{ and } \mathbf{Q} = \begin{bmatrix} n^1(s) & b^1(s) & t^1(s) \\ n^2(s) & b^2(s) & t^2(s) \\ n^3(s) & b^3(s) & t^3(s) \end{bmatrix},$$

where ρ is the surface radial coordinate defined as a function of circumferential location θ and length along the centerline path s, which is given by $s(X^3) = \int_0^{X^3} \left(\sqrt{\left(\frac{dy^1}{dX^3}\right)^2 + \left(\frac{dy^2}{dX^3}\right)^2 + 1} \right) dX^3$;

R_{cn} and Θ_{cn} are the redial and angular coordinates of the centerline path; **n**, **b** and **t** are the local Frenet frame axes of the centerline path.

A2. Modified Torus

Equation of torus in cylindrical polar coordinates is given by

$$\begin{aligned} X_1 &= r_{maj}\cos(\Theta) \\ X_2 &= (r_{min}\sin(\Theta)+R)\cos(\Phi) \\ X_3 &= (r_{min}\sin(\Theta)+R)\sin(\Phi), \end{aligned} \tag{B1}$$

where Θ and Φ define circumferential and centerline path coordinate; $r_{maj} = ecc.r_{min}$ with ecc being the mean cross-sectional ellipticity; and R is the radius of the torus centerline and $r_{min} = r_{STJ}\left(1+\left(\sqrt{taper}-1\right)\frac{R\Phi}{L}\right)$, where L is the length of centerline.

A3. Demonstration of the Curvature Dependent Growth

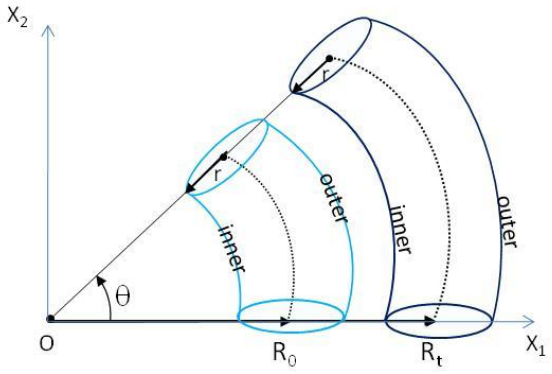

Figure A1. Elongation of a torus (blue) with a constant radius and centerline path tortuosity.

In the case of the simple elongation of a torus with a constant centerline path (Figure A1) tortuosity is given by $\text{Tortuosity} = \frac{\theta}{\sqrt{2-2\cos(\theta)}}$ (with θ in radians), and the longitudinal stretch ratios of inner and outer surfaces are given by

$$\lambda_L^{inn} = \frac{R_t - r}{R_0 - r} = \frac{(R_t - r)}{(R_0 - r)}\frac{(R_t + r)}{(R_t + r)} = \frac{R_t^2 - r^2}{R_0 R_t + rR_0 - rR_t - r^2}$$

$$\lambda_L^{out} = \frac{R_t + r}{R_0 + r} = \frac{(R_t + r)}{(R_0 + r)}\frac{(R_t - r)}{(R_t - r)} = \frac{R_t^2 - r^2}{R_0 R_t - rR_0 + rR_t - r^2}.$$

By comparing the denominators of the two stretch equations, we can see that the denominator of λ_L^{inn} is smaller than λ_L^{out} (since R_0-R_t<0 or R_t-R_0>0); thus, $\lambda_L^{inn} > \lambda_L^{out}$.

APPENDIX B

QUANTIFICATION OF RELATIVE FIBER CONTENT

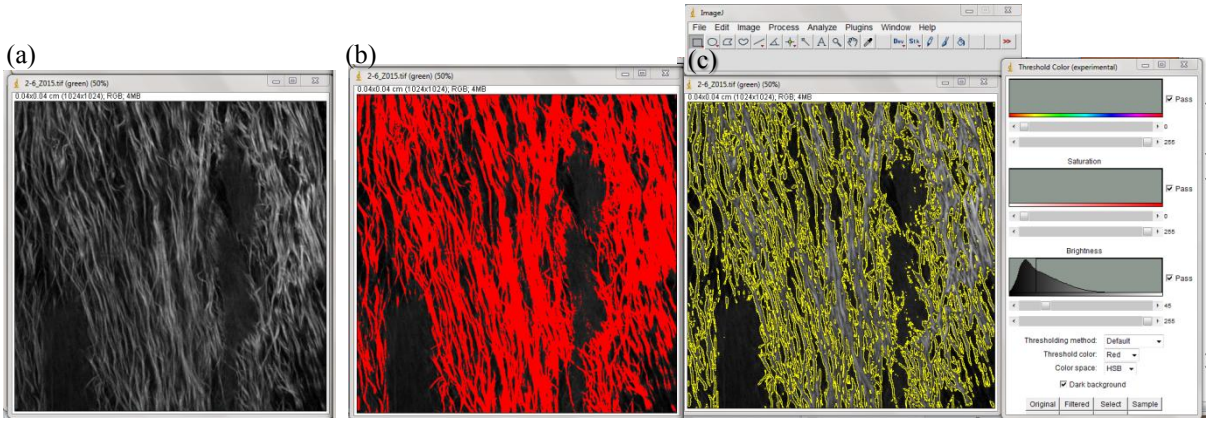

Figure B1. The relative area content of collagen and elastin quantified using ImageJ. The collagen and elastin channels were separated (a), and color threshold tool was used to adjust brightness level so that only fiber-containing regions are selected (b,c).

Once MPM images for each section were obtained, each picture was then split into collagen and elastin channels using the "Split Channels" function under the "Image → Color" tab. Next, the images obtained were converted into RGB images from their original 8-bit default setting. In each image regions of collagen and elastin shown were selected using the "Color Threshold" tool under the "Image → Adjust" tab (Figure B1,b). Boundaries around the areas of fibers were formed after hitting the "Select" button (Figure B1,c). The total fiber area was measured using the "Analyze → Measure" function, and this returned a value pertaining to the total area of the

fibers. From this, the percent area was calculated, and this value reflects the relative amount of collagen and elastin in each section.

APPENDIX C

FIBER PATH TRACKING AND ORIENTATION ANALYSIS

C1. MATLAB Program for Obtaining 2D Projection of MPM Image Stacks

```
% Program description: Opens stacks of multi-photon images and superimposes
% them into a 2D rendering.
%  Inputs:      1. Image Size
%               2. Your desired starting image in stack
%               3. Number of images in stack
%  Output:      1. Collagen 2D projected image
%               2. Elastin 2D projected image
clear all;
g=0; % Only tiffs!
aimg=0; % Do not invert image
disp('Enter image size in pixels (multi-photon is typically 1024x1024)')
imgsiz=input('ENTER 512 or 1024:  ')
[file,file_path]=uigetfile('*.tif','Select collagen image file')
img=imread([file_path file]);
```

```
% Give size of image
M=imgsiz;
N=imgsiz;
% Make new black image
rgb=0;
for rgb=1:3
        newimg(:,:,rgb)=double(zeros(imgsiz,imgsiz));
end
filsiz=length(file)
nfiles=str2num(file(filsiz-4))+...
10*str2num(file(filsiz-5))+...
100*str2num(file(filsiz-6))
num=input('ENTER: Number of files ');
for k=1:num;
         nfiles=nfiles+1;
        %NOTE: RGB, red = 1, green = 2, blue = 0
        % Convert image to double
           img=double(img);
           newimg(:,:,1)=newimg(:,:,1)+img(:,:,1);
           newimg(:,:,2)=newimg(:,:,2)+img(:,:,2);
           new_file=file(1:filsiz-7);
           zer=num2str(0);
           if nfiles < 10
```

```
            img=imread([file_path new_file zer zer num2str(nfiles) '.tif']);
            [file_path new_file zer zer num2str(nfiles) '.tif']
        else
            if nfiles >= 100
                img=imread([file_path new_file num2str(nfiles) '.tif']);
                [file_path new_file num2str(nfiles) '.tif']
            else
                img=imread([file_path new_file zer num2str(nfiles) '.tif']);
                [file_path new_file zer num2str(nfiles) '.tif']
            end
        end
        countdown=num-k;
end
% Display figures
maxcol=max(max(newimg(:,:,1)));
newimg(:,:,1)=(newimg(:,:,1)./maxcol)*255;
maxel=max(max(newimg(:,:,2)));
newimg(:,:,2)=uint8((newimg(:,:,2)./maxel)*255);
newimg=uint8(newimg);
figure(1)
imshow(newimg)
elastin(:,:,2)=newimg(:,:,2);
elastin(:,:,1)=double(zeros(imgsiz,imgsiz));
```

```
elastin(:,:,3)=double(zeros(imgsiz,imgsiz));

elastin=uint8(elastin);

figure(2)

imshow(elastin)

collagen(:,:,1)=newimg(:,:,1);

collagen(:,:,2)=double(zeros(imgsiz,imgsiz));

collagen(:,:,3)=double(zeros(imgsiz,imgsiz));

collagen=uint8(collagen);

figure(3)

imshow(collagen)

imwrite(collagen,[file_path 'collagen_sum' '.tif'],'tif')

imwrite(elastin,[file_path 'elastin_sum' '.tif'],'tif') Dfsdfsdf
```

C2. Implementation of Chaudhuri Algorithm

Below is the implementation of Chauhuri algorithm by Todd Courtney; this program is called by 'MainProgram.m'.

```
function [x_hist,y_hist] = courtney(name,lowths,t)

% This program tracks fiber paths and generated a fiber orientation histogram

% Inputs:       1. Name (collagen or elastin image file)

%               2. lowths (minimum threshold for image)

%               3. t (size of accumulator subregion denoted as w by Chauhuri)

% Output:   x_hist (0-180 degrees at 1 degree increment)
```

```
%          2. y_hist (Number of fibers at each given x_hist angle)
toln=0.0044; % Enter tolerance for angles
img_v2=imread([name,'.tif']);
img_v1=img_v2(:,:,2);
img_v1=medfilt2(img_v1);
img_v1=histeq(img_v1);
img_v1=double(img_v1); % convert array values from uint8 to double precision
% Find size of image
M=length(img_v1(:,1));
N=length(img_v1(1,:));
clear i j
for i=1:M; % iterate across rows
   for j=1:N; % iterate across columns
      if img_v1(i,j)<=lowths;
         img_v1(i,j)=0;
       end
   end
end
% Edge detection
s=3; % Set mask size s
l=2*s+1; % length of cols and rows of kernel
sig=2.0;
for i=-s:1:s;
```

```
    for j=-s:1:s;
        hy(i+s+1,j+s+1)=(2*i/sig^2)*exp(-(i^2+j^2)/sig^2);
        hx(i+s+1,j+s+1)=(2*j/sig^2)*exp(-(i^2+j^2)/sig^2);
    end
end
clear i j
for i=1:M-l+1; % iterate across rows
    for j=1:N-l+1; % iterate across columns
        gx=0;
        gy=0;
        for p=1:l; % iterate across rows of kernel over current pixel
            for q=1:l; % iterate across cols of kernel over current pixel
                gy=gy+hy(p,q)*img_v1(i-1+p,j-1+q);
                gx=gx+hx(p,q)*img_v1(i-1+p,j-1+q);
            end
        end
        Gx(i,j)=gx;
        Gy(i,j)=gy;
        G(i,j)=(gx^2+gy^2);
        if (gx<=0)&&(gy<=0);
            phi(i,j)=2;
        else
            if gx<=0;
```

```
            phi(i,j)=2;
        else
            phi(i,j)=atan(gy/gx);
        end
    end
  end
  countdown1=M+1-l-i;
end
% Directional Histogram Construction
k=0;
i=0;
j=0;
row=0;
for i=1:t:M-l+1;
  row=row+1;
  col=0;
  for j=1:t:N-l+1;
    col=col+1;
    clear A
    if (M-t-i>=t)&&(N-t-j>=t)
      theta=0;
      k=0;
      index=0;
```

```
for theta=0:1:179
   k=k+1;
   radian=theta*pi()/180;
   p=0;
   q=0;
   a=0;
   sum=0;
   % iterate across subregion
   for p=1:t;
      for q=1:t;
         if phi(i-1+p,j-1+q)==2;
            a=a+0;
         else
            a=a+G(i-1+p,j-1+q)*(cos(radian-phi(i-1+p,j-1+q)))^2;
         end
      end
   end
   A(k)=a; % accumulator bin sum across subregion
end
index=0; % reset index
if max(A)<=0;
   maxang(row,col)=200;
else
```

```
            [y,index]=max(A);
            maxang(row,col)=index-1;
        end
    end
  end
  countdown2=M+1-l-i;
end
% Normalize G for image
G=(G./max(max(G))).*255;
G=uint8(G);G=double(G);
% Take natural logarithm of G
clear i j
for i=1:length(G(:,1));
  for j=1:length(G(1,:));
    if G(i,j)<=0;
      Glog(i,j)=0;
    else
      Glog(i,j)=log(G(i,j));
    end
  end
end
clear x y u v
mag=20;
```

```
i=0;
j=0;
n=0;
row=0;
for i=1:t:M-l+1;
   row=row+1;
   col=0;
   for j=1:t:N-l+1;
      col=col+1;
      if (M-t-i>=t)&&(N-t-j>=t)
         n=n+1;
         x(n)=(j+(t/2)-1)+(s+1);
         y(n)=(i+(t/2)-1)+(s+1);
         if maxang(row,col)==200;
            u(n)=0;
            v(n)=0;
         else
            u(n)=mag*sin(maxang(row,col)*pi()/180);
            v(n)=-mag*cos(maxang(row,col)*pi()/180);
         end
      end
   end
end
```

```
% Determine the raw angles and histogram
angles=maxang(((maxang(:)>=1)&(maxang(:)<=180)));
[y_hist,x_hist]=hist(angles,1:180);
img_v1=uint8(img_v1);
figure(1)
imshow(img_v1);
hold on
quiver(x,y,u,v,'w');
saveas(gcf,[char(name) '.jpg'],'jpg');
figure(2)
bar(x_hist,y_hist);
saveas(gcf,[char(name) '_bar.jpg'],'jpg');
```

C3. MATLAB Program for Computing Mean Fiber Orientation and NOI

This program is called by the 'MainProgram.m' after 'courtney.m'

```
function [theta_c,theta_p,NOI,x_hist_final,y_hist_final]=OI_SALS_fata(x_hist,y_hist)
% Finds the mean fiber orientation and computes the NOI based on the
% histogram generated by 'courtney.m'
%  Inputs:      1. x_hist (0-180 degrees at 1 degree increment)
%               2. y_hist (Number of fibers at each given x_hist angle)
%  Outputs:     1. theta_c (mean fiber orientation)
%               2. theta_p (peak orientation or orientation with maximum number of fibers
```

```
%                   3. NOI
%                   4. x_hist_final (modified x_hist: -90 to 90 degrees)
%                   5. y_hist_final (normalized y_hist)
N=4;
polyfit_coeffs=polyfit(x_hist,y_hist,N);
y_polyfit=polyval(polyfit_coeffs,x_hist);
x_optima_pts_all=roots([polyfit_coeffs(1)*N,  polyfit_coeffs(2)*(N-1),  polyfit_coeffs(3)*(N-2),
polyfit_coeffs(4)*(N-3), polyfit_coeffs(5)*(N-4)]);
index_optima_pts_in_range=find(x_optima_pts_all>=0 & x_optima_pts_all<=180 &...
                        x_optima_pts_all==real(x_optima_pts_all));
x_optima_pts=x_optima_pts_all(index_optima_pts_in_range);
x_optima_pts=sort(x_optima_pts);
y_optima_pts=polyval(polyfit_coeffs, x_optima_pts);
% [min_value,min_index]=min(y_polyfit);
[min_value_y,min_index_y]=min(y_optima_pts);
min_index=round(x_optima_pts(min_index_y));
% % % % % %
figure(2)
bar(x_hist,y_hist);
hold on
plot(x_hist,y_polyfit,'r')
hold on
plot(x_optima_pts,y_optima_pts,'cX');
```

```
%
y_hist_mod=zeros(size(y_hist));
x_hist_mod=zeros(size(x_hist));
%
y_hist_mod(1:(179-min_index))=y_hist(min_index+1:179);
y_hist_mod((180-min_index):180)=y_hist(1:min_index+1);
x_hist_mod(1:(179-min_index))=x_hist(min_index+1:179);
x_hist_mod((180-min_index):180)=x_hist(1:min_index+1)+179;
%
yfit=smooth(y_hist_mod)';
%
figure(3)
bar(x_hist_mod,y_hist_mod)
hold on
plot(x_hist_mod,yfit,'g')
%
% Determine the centroid
for i=1:180-1
   theta_cnum(i)=x_hist_mod(i+1)*((yfit(i+1)+yfit(i))/2);
   theta_cden(i)=((yfit(i+1)+yfit(i))/2);
end
theta_c=round(sum(theta_cnum)/sum(theta_cden));
% Define theta_p
```

```
[value,index]=max(yfit);
theta_p=x_hist_mod(index);
[a b]=min(abs(x_hist_mod-theta_p)); % Find location of maximum
% theta_pdisc=x_hist(b);
%
 ZTOT = trapz(x_hist_mod.*pi/180,yfit(1:180)); % total area
%
% Calculate area centered about theta_p in increasing widths
for j=1:(length(x_hist_mod)/2)
       if (b-j>0)&&(b+j<181)          % double check within bounds .. .
      Zrow(j) = trapz(x_hist_mod(b-j:b+j).*pi/180,yfit(b-j:b+j)); % find area of intervals
   End
end
%
% % Normalize area to unity
Znorm=Zrow/ZTOT;
% Compute normalized fiber distribution
y_hist_final = y_hist_mod/ZTOT;
% Find where the area is reaches 50% and acquire its theta location
[az bz]=min(abs(Znorm-0.5));
tetastart=x_hist_mod(b-bz);
tetaend=x_hist_mod(b+bz);
% Calculate OI as theta that encompasses 50% centered at theta_p
```

```
OI=tetaend-tetastart;
NOI=((90-OI)/90)*100;
x_hist_final(1:180)=x_hist_mod(1:180)-theta_c;  % Modify range of x_hist to -90 to 90 deg
%
if theta_c > 180
   theta_c = theta_c - 180;
   theta_p = theta_p - 180;
end
```

MainProgram.m

The script below passes the image path, minimum threshold value and size of subregion to 'courtney.com', output of which are passed to 'OI_SALS_fata.m'. Finally all necessary ouput data and figures are saved.

```
clear all; clc; close all; warning off;
% %
curr_directory='F:\Multiphoton\\Adult\DA18M_medial\stretch_10%.tif.frames\';
name='elastin_sum';
%
file_path=strcat(curr_directory,name);
lowthes=140;  % Minimum threshold value for image
W=17; %  size of accumulator subregion A^W_theta, previously 12, now 30,
[x_hist,y_hist,angles]=courtney(file_path,lowthes,W); %mpm_image,name,lowths,t
```

```
[theta_c,theta_p,NOI,x_hist_final,y_hist_final]=OI_SALS_fata(x_hist,y_hist);
constants=[theta_c,theta_p,NOI]
saveas(gcf,[char(file_path) '_bar.jpg'],'jpg');
% save data
save([file_path,'.mat'],'name','constants','x_hist_final','y_hist_final','x_hist','y_hist','angles');
beep;
```

BIBLIOGRAPHY

1. Fung YC. *Biomechanics: Motion, Flow, Stress, and Growth*. New York: Springer-Verlag 1990.

2. Humphrey JD, Delange SL. *An introduction to biomechanics : Solids and fluids, analysis and design*. New York: Springer-Verlag; 2004.

3. Lucas CL, Wilcox BR, Coulter NA. Pulmonary vascular response to atrial septal defect closure in children. *J Surg Res* 1975,**18**:571-586.

4. Wilcox BR, Lucas CL. Pulmonary input impedance in children with left-right shunt. *J Surg Res* 1980,**29**:40-49.

5. Radke NF, Lucas CL, Wilcox BR. Detection of Pulmonary Vascular-Disease in Infants Using Input Impedance Spectra. *Circulation* 1984,**70**:458-458.

6. Milnor WR, Conti CR, Lewis KB, O'Rourke MF. Pulmonary arterial pulse wave velocity and impedance in man. *Circ Res* 1969,**25**:637-649.

7. Kitabatake A, Inoue M, Asao M, Masuyama T, Tanouchi J, Morita T*, et al.* Noninvasive evaluation of pulmonary hypertension by a pulsed Doppler technique. *Circulation* 1983,**68**:302-309.

8. Haneda T, Nakajima T, Shirato K, Onodera S, Takishima T. Effects of oxygen breathing on pulmonary vascular input impedance in patients with pulmonary hypertension. *Chest* 1983,**83**:520-527.

9. Kussmaul WG, 3rd, Altschuler JA, Herrmann HC, Laskey WK. Effects of pacing tachycardia and balloon valvuloplasty on pulmonary artery impedance and hydraulic power in mitral stenosis. *Circulation* 1992,**86**:1770-1779.

10. Nichols WW, O'Rourke MF. *McDonald's blood flow in arteries: Theoretical, experimental and clinical principles*. 5th ed. London: Hodder Arnold; 2005.

11. Fung YC. *Biomechanics: Mechanical properties of living tissues*. 2nd ed. New York: Springer-Verlag; 1993.

12. Mavroudis C, Backer CL. *Pediatric Cardiac Surgery*: Mosby, Inc; 2003.

13. Rudolph AM. The changes in the circulation after birth. Their importance in congenital heart disease. *Circulation* 1970,**41**:343-359.

14. Ursell PC, Byrne JM, Fears TR, Strobino BA, Gersony WM. Growth of the great vessels in the normal human fetus and in the fetus with cardiac defects. *Circulation* 1991,**84**:2028-2033.

15. Allen HD, Adams FH, Moss AJ. *Moss and Adams' heart disease in infants, children, and adolescents: Including the fetus and young adult*. 6th ed. Philadelphia: Lippincott Williams & Wilkins; 2001.

16. Adatia I, Kothari SS, Feinstein JA. Pulmonary hypertension associated with congenital heart disease: pulmonary vascular disease: the global perspective. *Chest* 2010,**137**:52S-61S.

17. Tulloh RM. Congenital heart disease in relation to pulmonary hypertension in paediatric practice. *Paediatr Respir Rev* 2005,**6**:174-180.

18. Deterling RA, Jr., Clagett OT. Aneurysm of the pulmonary artery; review of the literature and report of a case. *Am Heart J* 1947,**34**:471-499.

19. Kutty S, Kaul S, Danford CJ, Danford DA. Main pulmonary artery dilation in association with congenital bicuspid aortic valve in the absence of pulmonary valve abnormality. *Heart* 2010,**96**:1756-1761.

20. Patnaik AN, Barik R, Babu S, Gullati AS. A rare case of left lung hypoplasia associated with congenital pulmonary artery aneurysm and ventricular septal defect. *Pediatr Cardiol* 2012.

21. Greenwald SE, Johnson RJ, Haworth SG. Pulmonary vascular input impedance in the newborn and infant pig. *Cardiovascular Research* 1984,**18**:44-50.

22. Boumaza S, Arribas SM, Osborne-Pellegrin M, McGrath JC, Laurent S, Lacolley P*, et al.* Fenestrations of the carotid internal elastic lamina and structural adaptation in stroke-prone spontaneously hypertensive rats. *Hypertension* 2001,**37**:1101-1107.

23. Gaballa MA, Jacob CT, Raya TE, Liu J, Simon B, Goldman S. Large artery remodeling during aging: biaxial passive and active stiffness. *Hypertension* 1998,**32**:437-443.

24. Kogon BE, Patel M, Pernetz M, McConnell M, Book W. Late pulmonary valve replacement in congenital heart disease patients without original congenital pulmonary valve pathology. *Pediatric Cardiology* 2009,**31**:74-79.

25. Ono M, Goerler H, Kallenbach K, Boethig D, Westhoff-Bleck M, Breymann T. Aortic valve-sparing reimplantation for dilatation of the ascending aorta and aortic regurgitation late after repair of congenital heart disease. *J Thorac Cardiovasc Surg* 2007,**133**:876-879.

26. Rosenberg HG, Williams WG, Trusler GA, Higa T, Rabinovitch M. Structural composition of central pulmonary arteries. Growth potential after surgical shunts. *J Thorac Cardiovasc Surg* 1987,**94**:498-503.

27. Mayer JE, Jr. Uses of homograft conduits for right ventricle to pulmonary artery connections in the neonatal period. *Semin Thorac Cardiovasc Surg* 1995,**7**:130-132.

28. Cho SW, Kim IK, Kang JM, Song KW, Kim HS, Park CH*, et al.* Evidence for in vivo growth potential and vascular remodeling of tissue-engineered artery. *Tissue Eng Part A* 2009,**15**:901-912.

29. Hoerstrup SP, Cummings Mrcs I, Lachat M, Schoen FJ, Jenni R, Leschka S*, et al.* Functional growth in tissue-engineered living, vascular grafts: follow-up at 100 weeks in a large animal model. *Circulation* 2006,**114**:I159-166.

30. Shinoka T, Shum-Tim D, Ma PX, Tanel RE, Isogai N, Langer R*, et al.* Creation of viable pulmonary artery autografts through tissue engineering. *J Thorac Cardiovasc Surg* 1998,**115**:536-545; discussion 545-536.

31. Mol A, Smits AI, Bouten CV, Baaijens FP. Tissue engineering of heart valves: advances and current challenges. *Expert Rev Med Devices.* 2009,**6**:259-275.

32. O'Rourke MF, Nichols WW. Aortic diameter, aortic stiffness, and wave reflection increase with age and isolated systolic hypertension. *Hypertension* 2005,**45**:652-658.

33. Alvarez L, Aranega A, Saucedo R, Contreras JA, Lopez F. Morphometric data concerning the great arterial trunks and their branches. *Int J Cardiol* 1990,**29**:127-139.

34. Castillo EH, Arteaga-Martinez M, Garcia-Pelaez I, Villasis-Keever MA, Aguirre OM, Moran V*, et al.* Morphometric study of the human fetal heart. I. Arterial segment. *Clin Anat* 2005,**18**:260-268.

35. Snider AR, Enderlein MA, Teitel DF, Juster RP. Two-dimensional echocardiographic determination of aortic and pulmonary artery sizes from infancy to adulthood in normal subjects. *Am J Cardiol* 1984,**53**:218-224.

36. Henry WL, Ware J, Gardin JM, Hepner SI, McKay J, Weiner M. Echocardiographic measurements in normal subjects. Growth-related changes that occur between infancy and early adulthood. *Circulation* 1978,**57**:278-285.

37. Epstein ML, Goldberg SJ, Allen HD, Konecke L, Wood J. Great vessel, cardiac chamber, and wall growth patterns in normal children. *Circulation* 1975,**51**:1124-1129.

38. Sievers HH, Onnasch DG, Lange PE, Bernhard A, Heintzen PH. Dimensions of the great arteries, semilunar valve roots, and right ventricular outflow tract during growth: normative angiocardiographic data. *Pediatr Cardiol* 1983,**4**:189-196.

39. Grant RP, Downey FM, Macmahon H. The architecture of the right ventricular outflow tract in the normal human heart and in the presence of ventricular septal defects. *Circulation* 1961,**24**:223-235.

40. Szpinda M, Brazis P, Elminowska-Wenda G, Wisniewski M. Morphometric study of the aortic and great pulmonary arterial pathways in human foetuses. *Ann Anat* 2006,**188**:25-31.

41. Herijgers P, Ozaki S, Verbeken E, Van Lommel A, Racz R, Zietkiewicz M*, et al.* Calcification characteristics of porcine stentless valves in juvenile sheep. *Eur J Cardiothorac Surg* 1999,**15**:134-142.

42. Sutherland FW, Perry TE, Yu Y, Sherwood MC, Rabkin E, Masuda Y*, et al.* From stem cells to viable autologous semilunar heart valve. *Circulation* 2005,**111**:2783-2791.

43. Wang Z, Chesler NC. Pulmonary vascular wall stiffness: An important contributor to the increased right ventricular afterload with pulmonary hypertension. *Pulm Circ* 2011,**1**:212-223.

44. Kobs RW, Muvarak NE, Eickhoff JC, Chesler NC. Linked mechanical and biological aspects of remodeling in mouse pulmonary arteries with hypoxia-induced hypertension. *Am J Physiol Heart Circ Physiol* 2005,**288**:H1209-1217.

45. Drexler ES, Bischoff JE, Slifka AJ, McCowan CN, Quinn TP, Shandas R*, et al.* Stiffening of the extrapulmonary arteries from rats in chronic hypoxic pulmonary hypertension. *Journal of Research of the National Institute of Standards and Technology* 2008,**113**:239–249.

46. Tozzi CA, Christiansen DL, Poiani GJ, Riley DJ. Excess collagen in hypertensive pulmonary arteries decreases vascular distensibility. *Am J Respir Crit Care Med* 1994,**149**:1317-1326.

47. Ooi CY, Wang Z, Tabima DM, Eickhoff JC, Chesler NC. The role of collagen in extralobar pulmonary artery stiffening in response to hypoxia-induced pulmonary hypertension. *Am J Physiol Heart Circ Physiol* 2010,**299**:H1823-1831.

48. Poiani GJ, Tozzi CA, Yohn SE, Pierce RA, Belsky SA, Berg RA*, et al.* Collagen and elastin metabolism in hypertensive pulmonary arteries of rats. *Circ Res* 1990,**66**:968-978.

49. Tucker A, Migally N, Wright ML, Greenlees KJ. Pulmonary vascular changes in young and aging rats exposed to 5,486 m altitude. *Respiration* 1984,**46**:246-257.

50. Leung DYM, Glagov S, Mathews MB. Elastin and Collagen Accumulation in Rabbit Ascending Aorta and Pulmonary Trunk during Postnatal Growth; correlation of Cellular Synthetic Response with Medial Tension. *Circ Res* 1977,**41**:316-323.

51. Langille BL, Brownlee RD, Adamson SL. Perinatal aortic growth in lambs: relation to blood flow changes at birth. *Am J Physiol* 1990,**259**:H1247-1253.

52. Lammers SR, Kao PH, Qi HJ, Hunter K, Lanning C, Albietz J*, et al.* Changes in the structure-function relationship of elastin and its impact on the proximal pulmonary arterial mechanics of hypertensive calves. *Am J Physiol Heart Circ Physiol* 2008,**295**:H1451-1459.

53. Choudhury N, Bouchot O, Rouleau L, Tremblay D, Cartier R, Butany J*, et al.* Local mechanical and structural properties of healthy and diseased human ascending aorta tissue. *Cardiovasc Pathol* 2009,**18**:83-91.

54. Huang Y, Guo X, Kassab GS. Axial nonuniformity of geometric and mechanical properties of mouse aorta is increased during postnatal growth. *Am J Physiol Heart Circ Physiol* 2006,**290**:H657-664.

55. Haskett D, Johnson G, Zhou A, Utzinger U, Vande Geest J. Microstructural and biomechanical alterations of the human aorta as a function of age and location. *Biomech Model Mechanobiol* 2010,**9**:725-736.

56. Greenwald SE, Berry CL, Haworth SG. Changes in distensibility of intrapulmonary arteries in the normal newborn and growing pig. *Cardiovascular Research* 1982,**16**:716-725.

57. Rachev A, Greenwald SE, Kane TP, Jr JEM, Meister JJ. Analysis of the strain and stress distribution in the wall of the developing and mature rat aorta. *Biorheology* 1995,**32**:473-485.

58. Pagani M, Mirsky I, Baig H, Manders WT, Kerkhof P, Vatner SF. Effects of age on aortic pressure-diameter and elastic stiffness-stress relationships in unanesthetized sheep. *Circ Res* 1979,**44**:420-429.

59. Berry CL, Looker T, Germain J. The growth and development of the rat aorta. I. Morphological aspects. *J Anat* 1972,**113**:1-16.

60. Wells SM, Langille BL, Lee JM, Adamson SL. Determinants of mechanical properties in the developing ovine thoracic aorta. *Am J Physiol* 1999,**277**:H1385-1391.

61. Wells SM, Langille BL, Adamson SL. In vivo and in vitro mechanical properties of the sheep thoracic aorta in the perinatal period and adulthood. *Am J Physiol* 1998,**274**:H1749-1760.

62. Sacks MS, Sun W. Multiaxial mechanical behavior of biological materials. *Annu Rev Biomed Eng* 2003,**5**:251-284.

63. Chesler NC, Thompson-Figueroa J, Millburne K. Measurements of mouse pulmonary artery biomechanics. *J Biomech Eng* 2004,**126**:309-314.

64. Billiar KL, Sacks MS. Biaxial mechanical properties of the natural and glutaraldehyde treated aortic valve cusp--Part I: Experimental results. *J Biomech Eng* 2000,**122**:23-30.

65. Grashow JS. Evaluation of the Biaxial Mechanical Properties of the Mitral Valve Anterior Leaflet Under Physiological Loading Conditions [Master's Thesis]. Pittsburgh, PA: University of Pittsburgh; 2005.

66. Vaishnav RN, Vossoughi J. *Estimation of residual strains in aortic segments.* New York; 1983.

67. Fung YC. *What principle governs the stress distribution in living organisms?* Beijing: Science Press; 1983.

68. Chuong CJ, Fung YC. On residual stresses in arteries. *J Biomech Eng* 1986,**108**:189-192.

69. Takamizawa K, Hayashi K. Strain energy density function and uniform strain hypothesis for arterial mechanics. *J Biomech* 1987,**20**:7-17.

70. Fratzl P. *Collagen structure and mechanics*. New York: Springer; 2008.

71. Mithieux SM, Weiss AS. Elastin. *Advances in protein chemistry* 2005,**70**:437-461.

72. Sherratt MJ. Tissue elasticity and the ageing elastic fibre. *Age* 2009,**31**:305-325.

73. Gosline J, Lillie M, Carrington E, Guerette P, Ortlepp C, Savage K. Elastic proteins: biological roles and mechanical properties. *Philos Trans R Soc Lond B Biol Sci* 2002,**357**:121-132.

74. Hulmes DJ. Building collagen molecules, fibrils, and suprafibrillar structures. *J Struct Biol* 2002,**137**:2-10.

75. von der Mark K. Localization of collagen types in tissues. *Int Rev Connect Tissue Res* 1981,**9**:265-324.

76. Wolinsky H, Glagov S. Structural Basis for the Static Mechanical Properties of the Aortic Media. *Circ Res* 1964,**14**:400-413.

77. Heath D, Wood EH, Dushane JW, Edwards JE. The structure of the pulmonary trunk at different ages and in cases of pulmonary hypertension and pulmonary stenosis. *J Pathol Bacteriol* 1959,**77**:443-456.

78. Saldana M, Arias-Stella J. Studies on the strcture of the pulmonary trunk. I. Normal changes in the elastic configuration of the human pulmonary trunk at different ages. *Circulation* 1963,**27**:1086-1093.

79. Green AE, Zerna W. *Theoretical elasticity*. 2nd ed. New York: Dover; 1992.

80. Cowin SC. The mechanical and stress adaptive properties of bone. *Ann Biomed Eng* 1983,**11**:263-295.

81. Fung YC. Elasticity of soft tissues in simple elongation. *Am J Physiol* 1967,**213**:1532-1544.

82. Fung YC, Fronek K, Patitucci P. Pseudoelasticity of arteries and the choice of its mathematical expression. *Am J Physiol* 1979,**237**:H620-631.

83. Humphrey JD, Yin FC. A new constitutive formulation for characterizing the mechanical behavior of soft tissues. *Biophysical Journal* 1987,**52**:563-570.

84. Holzapfel GA, Weizsacker HW. Biomechanical behavior of the arterial wall and its numerical characterization. *Comput Biol Med* 1998,**28**:377-392.

85. Rivlin RS, Saunders DW. Large elastic deformations of isotropic materials .7. Experiments on the deformation of rubber. *Philos Trans R Soc Lond A Math Physic Sci* 1951,**243**:251-288.

86. Holzapfel GA, Gasser TC. A new constitutive framework for arterial wall mechanics and a comparative study of material models. *J Elasticity* 2000,**61**:1-48.

87. Roach MR, Burton AC. The reason for the shape of the distensibility curves of arteries. *Can J Biochem Physiol* 1957,**35**:681-690.

88. Scott S, Ferguson GG, Roach MR. Comparison of the elastic properties of human intracranial arteries and aneurysms. *Can J Physiol Pharmacol* 1972,**50**:328-332.

89. Lanir Y. A structural theory for the homogeneous biaxial stress-strain relationships in flat collagenous tissues. *J Biomech* 1979,**12**:423-436.

90. Lanir Y. Constitutive equations for fibrous connective tissues. *J Biomech* 1983,**16**:1-12.

91. Wognum S, Schmidt DE, Sacks MS. On the mechanical role of de novo synthesized elastin in the urinary bladder wall. *J Biomech Eng* 2009,**131**:101018.

92. Hill MR, Duan X, Gibson GA, Watkins S, Robertson AM. A theoretical and non-destructive experimental approach for direct inclusion of measured collagen orientation and recruitment into mechanical models of the artery wall. *J Biomech* 2012,**45**:762-771.

93. Sacks MS. Incorporation of experimentally-derived fiber orientation into a structural constitutive model for planar collagenous tissues. *J Biomech Eng* 2003,**125**:280-287.

94. Liao J, Yang L, Grashow J, Sacks MS. The relation between collagen fibril kinematics and mechanical properties in the mitral valve anterior leaflet. *J Biomech Eng* 2007,**129**:78-87.

95. Wognum S. A multi-phase structural constitutive model for insights into soft tissue remodeling mechanisms [PhD Dissertation]. Pittsburgh, PA: University of Pittsburgh; 2010.

96. Taber LA. *Nonlinear Theory of Elasticity, Applications in Biomechanics*. Danvers, MA: World Scientific Publishing; 2004.

97. Fung YC. Biorheology of soft tissues. *Biorheology* 1973,**10**:139-155.

98. Spencer AJM. *Continuum mechanics*. Dover ed. Mineola, N.Y.: Dover Publications; 2004.

99. Holzapfel GA. *Nonlinear solid mechanics: a continuum approach for engineering*. Chichester ; New York: Wiley; 2000.

100. Holzapfel GA. Determination of material models for arterial walls from uniaxial extension tests and histological structure. *J Theor Biol* 2006,**238**:290-302.

101. Holzapfel GA, Gasser TC, Ogden RW. Comparison of a multi-layer structural model for arterial walls with a fung-type model, and issues of material stability. *J Biomech Eng* 2004,**126**:264-275.

102. Humphrey JD, Strumpf RK, Yin FC. Determination of a constitutive relation for passive myocardium: I. A new functional form. *J Biomech Eng* 1990,**112**:333-339.

103. Humphrey JD, Yin FC. On constitutive relations and finite deformations of passive cardiac tissue: I. A pseudostrain-energy function. *J Biomech Eng* 1987,**109**:298-304.

104. Itskov M, Ehret AE, Mavrilas D. A polyconvex anisotropic strain-energy function for soft collagenous tissues. *Biomech Model Mechanobiol* 2006,**5**:17-26.

105. Billiar KL, Sacks MS. Biaxial mechanical properties of the native and glutaraldehyde-treated aortic valve cusp: Part II--A structural constitutive model. *J Biomech Eng* 2000b,**122**:327-335.

106. Freed AD, Einstein DR, Vesely I. Invariant formulation for dispersed transverse isotropy in aortic heart valves: an efficient means for modeling fiber splay. *Biomech Model Mechanobiol* 2005,**4**:100-117.

107. Chen K, Fata B, Einstein DR. Characterization of the highly nonlinear and anisotropic vascular tissues from experimental inflation data: a validation study toward the use of clinical data for in-vivo modeling and analysis. *Ann Biomed Eng* 2008,**36**:1668-1680.

108. Einstein DR, Freed AD, Stander N, Fata B, Vesely I. Inverse parameter fitting of biological tissues: a response surface approach. *Ann Biomed Eng* 2005,**33**:1819-1830.

109. Taber LA. A model for aortic growth based on fluid shear and fiber stresses. *J Biomech Eng* 1998,**120**:348-354.

110. Rachev A, Stergiopulos N, Meister JJ. A model for geometric and mechanical adaptation of arteries to sustained hypertension. *J Biomech Eng* 1998,**120**:9-17.

111. Taber LA, Humphrey JD. Stress-modulated growth, residual stress, and vascular heterogeneity. *J Biomech Eng* 2001,**123**:528-535.

112. Hsu FH. The influences of mechanical loads on the form of a growing elastic body. *J Biomech* 1968,**1**:303-311.

113. Hegedus DH, Cowin SC. Bone remodeling II: small strain adaptive elasticity. *J Elasticity* 1976,**6**:337-352.

114. Cowin SC, Hegedus DH. Bone remodeling I: theory of adaptive elasticity. *J Elasticity* 1976,**6**:313-326.

115. Skalak R, Dasgupta G, Moss M, Otten E, Dullumeijer P, Vilmann H. Analytical description of growth. *J Theor Biol* 1982,**94**:555-577.

116. Rodriguez EK, Hoger A, McCulloch AD. Stress-dependent finite growth in soft elastic tissues. *J Biomech* 1994,**27**:455-467.

117. Alastrue V, Martinez MA, Doblare M. Modelling adaptative volumetric finite growth in patient-specific residually stressed arteries. *J Biomech* 2008,**41**:1773-1781.

118. Atkin RJ, Craine RE. Continuum Theories of Mixtures - Basic Theory and Historical Development. *Quarterly Journal of Mechanics and Applied Mathematics* 1976,**29**:209-244.

119. Bowen RM. A Theory of Constrained Mixtures with Multiple Temperatures. *Archive for Rational Mechanics and Analysis* 1979,**70**:235-250.

120. Gleason RL, Jr., Humphrey JD. A 2D constrained mixture model for arterial adaptations to large changes in flow, pressure and axial stretch. *Math Med Biol* 2005,**22**:347-369.

121. Humphrey JD, Rajagopal KR. A constrained mixture model for arterial adaptations to a sustained step change in blood flow. *Biomech Model Mechanobiol* 2003,**2**:109-126.

122. Gleason RL, Taber LA, Humphrey JD. A 2-D model of flow-induced alterations in the geometry, structure, and properties of carotid arteries. *J Biomech Eng* 2004,**126**:371-381.

123. Cois A, Galeotti J, Tamburo R, Sacks M, Stetten G. Shells and Spheres: An n-Dimensional Framework for Medial-Based Image Segmentation. *International Journal of Biomedical Imaging* 2010,**2010**:1-13.

124. Cow CA, Rockot K, Galeotti J, Tamburo R, Gottlieb D, Mayer JE*, et al.* Automated segmentation of the right heart using an optimized Shells and Spheres algorithm. In: *4th IEEE International Symposium on Biomedical Imaging: From Nano to Macro (ISBI 2007)*; 2007. pp. 876-879.

125. Azar A. An interactive intensity- and feature-based non-rigid registration framework for 3D medical images [Master's Thesis]. Sophia-Antipolis, France: Université de Nice Sophia-Antipolis; 2005.

126. Nielsen PM, Le Grice IJ, Smaill BH, Hunter PJ. Mathematical model of geometry and fibrous structure of the heart. *Am J Physiol* 1991,**260**:H1365-1378.

127. Smith DB, Sacks MS, Vorp DA, Thornton M. Surface geometric analysis of anatomic structures using biquintic finite element interpolation. *Ann Biomed Eng* 2000,**28**:598-611.

128. Struik DJ. *Lectures on classical differential geometry*. 2nd ed. New York: Dover; 1961.

129. Renton JD. *Applied Elasticity: Matrix and Tensor Analysis of Elastic Continua*. Chichester: Ellis Horwood Limited; 1987.

130. Berry CL. Growth, development, and healing of large arteries. *Ann R Coll Surg Engl* 1973,**53**:246-257.

131. de Sa M, Moshkovitz Y, Butany J, David TE. Histologic abnormalities of the ascending aorta and pulmonary trunk in patients with bicuspid aortic valve disease: clinical relevance to the ross procedure. *J Thorac Cardiovasc Surg* 1999,**118**:588-594.

132. O'Rourke MF. Mechanical principles. Arterial stiffness and wave reflection. *Pathol Biol (Paris)* 1999,**47**:623-633.

133. Taylor MG. Wave-travel in a non-uniform transmission line, in relation to pulses in arteries. *Phys Med Biol* 1965,**10**:539-550.

134. Choi G, Cheng CP, Wilson NM, Taylor CA. Methods for quantifying three-dimensional deformation of arteries due to pulsatile and nonpulsatile forces: Implications for the design of stents and stent grafts. *Ann Biomed Eng* 2008,**37**:14-33.

135. Thubrikar MJ. *Vascular mechanics and pathology*: Springer; 2007.

136. Sacks MS, Chuong CJ. Orthotropic mechanical properties of chemically treated bovine pericardium. *Ann Biomed Eng* 1998,**26**:892-902.

137. Billiar KL, Sacks MS. Biaxial mechanical properties of the natural and glutaraldehyde treated aortic valve cusp--Part I: Experimental results. *J Biomech Eng* 2000a,**122**:23-30.

138. Hoffman AH, Grigg P. A method for measuring strains in soft tissue. *J Biomech* 1984,**17**:795-800.

139. Vande Geest JP, Sacks MS, Vorp DA. The effects of aneurysm on the biaxial mechanical behavior of human abdominal aorta. *J Biomech* 2006,**39**:1324-1334.

140. Gozna ER, Marble AE, Shaw A, Holland JG. Age-related changes in the machanics of the aorta and Pulmonary artery of man. *J Appl Physiol* 1974,**36**:407-411.

141. Vande Geest JP, Sacks MS, Vorp DA. Age dependency of the biaxial biomechanical behavior of human abdominal aorta. *J Biomech Eng* 2004,**126**:815-822.

142. Patel DJ, Schilder DP, Mallos AJ. Mechanical properties and dimensions of the major pulmonary arteries. *J Appl Physiol* 1960,**15**:92-96.

143. Drexler ES, Quinn TP, Slifka AJ, McCowan CN, Bischoff JE, Wright JE*, et al.* Comparison of mechanical behavior among the extrapulmonary arteries from rats. *J Biomech* 2007,**40**:812-819.

144. Hunter KS, Albietz JA, Lee PF, Lanning CJ, Lammers SR, Hofmeister SH*, et al.* In vivo measurement of proximal pulmonary artery elastic modulus in the neonatal calf model of pulmonary hypertension: development and ex vivo validation. *J Appl Physiol* 2010,**108**:968-975.

145. Cox RH. Viscoelastic properties of canine pulmonary arteries. *Am J Physiol* 1984,**246**:H90-96.

146. Takkenberg JJ, Klieverik LM, Schoof PH, van Suylen RJ, van Herwerden LA, Zondervan PE*, et al.* The Ross procedure: A systematic review and meta-analysis. *Circulation* 2009,**119**:222-228.

147. David TE, Omran A, Ivanov J, Armstrong S, de Sa MP, Sonnenberg B*, et al.* Dilation of the pulmonary autograft after the Ross procedure. *J Thorac Cardiovasc Surg* 2000,**119**:210-220.

148. Hosoda Y, Kawano K, Yamasawa F, Ishii T, Shibata T, Inayama S. Age-dependent changes of collagen and elastin content in human aorta and pulmonary artery. *Angiology* 1984,**35**:615-621.

149. Humphrey JD. *Cardiovascular Solid Mechanics: Cells, tissues and organs*. New York: Springer; 2002.

150. Patel DJ, Freitas FMD, Mallos AJ. Mechanical function of the main pulmonary artery. *J Appl Physiol* 1962,**17**:205-208.

151. Tabima DM, Chesler NC. The effects of vasoactivity and hypoxic pulmonary hypertension on extralobar pulmonary artery biomechanics. *J Biomech* 2010,**43**:1864-1869.

152. Berger RM, Cromme-Dijkhuis AH, Hop WC, Kruit MN, Hess J. Pulmonary arterial wall distensibility assessed by intravascular ultrasound in children with congenital heart disease: an indicator for pulmonary vascular disease? *Chest* 2002,**122**:549-557.

153. Jiang ZL, Kassab GS, Fung YC. Diameter-defined Strahler system and connectivity matrix of the pulmonary arterial tree. *J Appl Physiol* 1994,**76**:882-892.

154. Fung YC, Liu SQ. Changes of zero-stress state of rat pulmonary arteries in hypoxic hypertension. *J Appl Physiol* 1991,**70**:2455-2470.

155. Liu SQ, Fung YC. Influence of STZ-induced diabetes on zero-stress states of rat pulmonary and systemic arteries. *Diabetes* 1992,**41**:136-146.

156. Han HC, Fung YC. Direct measurement of transverse residual strains in aorta. *Am J Physiol* 1996,**270**:H750-759.

157. Huang W, Sher YP, Delgado-West D, Wu JT, Peck K, Fung YC. Tissue remodeling of rat pulmonary artery in hypoxic breathing. I. Changes of morphology, zero-stress state, and gene expression. *Ann Biomed Eng* 2001,**29**:535-551.

158. Sacks MS, Smith DB, Hiester ED. A small angle light scattering device for planar connective tissue microstructural analysis. *Ann Biomed Eng* 1997,**25**:678-689.

159. Joyce EM, Moore JJ, Sacks MS. Biomechanics of the fetal membrane prior to mechanical failure: Review and implications. *Eur J Obstet Gynecol Reprod Biol* 2009,**144 Suppl 1**:S121-127.

160. Gaitan-Leon DM, Schmidt DE, Chew DW, Vorp DA, Sacks MS. Structural information of cardiovascular tissues using small angle light scattering. In: *Proceedings of the American Society of Mechanical Engineers (ASME) Summer Bioengineering Conference*. Lake Tahoe, CA; 2009.

161. Zoumi A, Lu XA, Kassab GS, Tromberg BJ. Imaging coronary artery microstructure using second-harmonic and two-photon fluorescence microscopy. *Biophysical Journal* 2004,**87**:2778-2786.

162. Boulesteix T, Pena AM, Pages N, Godeau G, Sauviat MP, Beaurepaire E, *et al.* Micrometer scale ex vivo multiphoton imaging of unstained arterial wall structure. *Cytometry A* 2006,**69**:20-26.

163. Konig K, Schenke-Layland K, Riemann I, Stock UA. Multiphoton autofluorescence imaging of intratissue elastic fibers. *Biomaterials* 2005,**26**:495-500.

164. Zipfel WR, Williams RM, Christie R, Nikitin AY, Hyman BT, Webb WW. Live tissue intrinsic emission microscopy using multiphoton-excited native fluorescence and second harmonic generation. *Proceedings of the National Academy of Sciences of the United States of America* 2003,**100**:7075-7080.

165. Scherschel JA, Rubart M. Cardiovascular imaging using two-photon microscopy. *Microsc Microanal* 2008,**14**:492-506.

166. Chaudhuri BB, Kundu P, Sarkar N. Detection and gradation of oriented texture. *Pattern Recognition Letters* 1993,**14**:147-153.

167. Karlon WJ, Covell JW, McCulloch AD, Hunter JJ, Omens JH. Automated measurement of myofiber disarray in transgenic mice with ventricular expression of ras. *Anat Rec* 1998,**252**:612-625.

168. Courtney T, Sacks MS, Stankus J, Guan J, Wagner WR. Design and analysis of tissue engineering scaffolds that mimic soft tissue mechanical anisotropy. *Biomaterials* 2006,**27**:3631-3638.

169. Davidson JM, Hill KE, Alford JL. Developmental changes in collagen and elastin bioynthesis in the porcine aorta. *Developmental Biology* 1986,**118**:103-111.

170. Bendeck MP, Langille BL. Rapid accumulation of elastin and collagen in the aortas of sheep in the immediate perinatal period. *Circ Res* 1991,**69**:1165-1169.

171. Beridze N, Frishman WH. Vascular Ehlers-Danlos syndrome: pathophysiology, diagnosis, and prevention and treatment of its complications. *Cardiol Rev* 2012,**20**:4-7.

172. Stakos DA, Tziakas DN, Chalikias GK, Mitrousi K, Tsigalou C, Boudoulas H. Associations between collagen synthesis and degradation and aortic function in arterial hypertension. *Am J Hypertens* 2010,**23**:488-494.

173. Avolio A, Jones D, Tafazzoli-Shadpour M. Quantification of alterations in structure and function of elastin in the arterial media. *Hypertension* 1998,**32**:170-175.

174. Martyn CN, Greenwald SE. Impaired synthesis of elastin in walls of aorta and large conduit arteries during early development as an initiating event in pathogenesis of systemic hypertension. *Lancet* 1997,**350**:953-955.

175. Gundiah N, M BR, L AP. Determination of strain energy function for arterial elastin: Experiments using histology and mechanical tests. *J Biomech* 2007,**40**:586-594.

176. Martyn CN, Greenwald SE. Impaired synthesis of elastin in walls of aorta and large conduit arteries during early development as an initiating event in pathogenesis of systemic hypertension. *The Lancet* 1997,**350**:953-955.

177. Wagenseil JE, Mecham RP. Elastin in large artery stiffness and hypertension. *J Cardiovasc Transl Res* 2012.

178. Ogden RW, Saccomandi G. Introducing mesoscopic information into constitutive equations for arterial walls. *Biomech Model Mechanobiol* 2007,**6**:333-344.

179. Zou Y, Zhang Y. An experimental and theoretical study on the anisotropy of elastin network. *Ann Biomed Eng* 2009,**37**:1572-1583.

180. Lillie MA, Shadwick RE, Gosline JM. Mechanical anisotropy of inflated elastic tissue from the pig aorta. *J Biomech* 2010,**43**:2070-2078.

181. Cox RH. Passive mechanics and connective tissue composition of canine arteries. *Am J Physiol* 1978,**234**:H533-541.

182. Roy S, Boss C, Rezakhaniha R, Stergiopulos N. Experimental characterization of the distribution of collagen fiber recruitment. *J Biorheology* 2010,**24**:84-93.

183. Meijering E, Jacob M, Sarria JCF, Steiner P, Hirling H, Unser M. Design and validation of a tool for neurite tracing and analysis in fluorescence microscopy images. *Cytometry Part A* 2004,**58A**:167-176.

184. Hill M. A Novel Approach for Combining Biomechanical and Micro-structural Analyses to Assess the Mechanical and Damage Properties of the Artery Wall [PhD Dissertation]. Pittsburgh, PA: University of Pittsburgh; 2011.

185. Holzapfel GA, Ogden RW. Constitutive modelling of arteries. *Proceedings of the Royal Society a-Mathematical Physical and Engineering Sciences* 2010,**466**:1551-1596.

186. Demiray H. A note on the elasticity of soft biological tissues. *J Biomech* 1972,**5**:309-311.

187. McEniery CM, Wilkinson IB, Avolio AP. Age, hypertension and arterial function. *Clin Exp Pharmacol Physiol* 2007,**34**:665-671.

188. Schwartz CJ, Valente AJ, Sprague EA, Kelley JL, Nerem RM. The pathogenesis of atherosclerosis: an overview. *Clin Cardiol* 1991,**14**:I1-16.

189. Zulliger MA, Fridez P, Hayashi K, Stergiopulos N. A strain energy function for arteries accounting for wall composition and structure. *J Biomech* 2004,**37**:989-1000.

190. Gasser TC, Ogden RW, Holzapfel GA. Hyperelastic modelling of arterial layers with distributed collagen fibre orientations. *J R Soc Interface* 2006,**3**:15-35.

191. Sherebrin MH, Song SH, Roach MR. Mechanical anisotropy of purified elastin from the thoracic aorta of dog and sheep. *Can J Physiol Pharmacol* 1983,**61**:539-545.

192. Bischoff JE, Arruda EM, Grosh K. A microstructurally based orthotropic hyperelastic constitutive law. *J Appl Mech-Transactions of the ASME* 2002,**69**:570-579.

193. Urry DW, Hugel T, Seitz M, Gaub HE, Sheiba L, Dea J*, et al.* Elastin: a representative ideal protein elastomer. *Philos Trans R Soc Lond B Biol Sci* 2002,**357**:169-184.

194. Erman B. Molecular aspects of rubber elasticity. In: *Mechanics and thermomechanics of rubberlike solids, CISM courses and lecture notes*. Edited by Saccomandi G, Ogden RW. Vienna: Springer; 2004.

195. Sasaki N, Odajima S. Elongation mechanism of collagen fibrils and force-strain relations of tendon at each level of structural hierarchy. *J Biomech* 1996,**29**:1131-1136.

196. Sasaki N, Odajima S. Stress-strain curve and Young's modulus of a collagen molecule as determined by the X-ray diffraction technique. *J Biomech* 1996,**29**:655-658.

197. Sun YL, Luo ZP, Fertala A, An KN. Stretching type II collagen with optical tweezers. *J Biomech* 2004,**37**:1665-1669.